Fall 2015

# Numerical Studies and Optimization of Magnetron with Diffraction Output (MDO) Using Particle-in-Cell Simulations

Alireza Majzoobi
*Old Dominion University*

# NUMERICAL STUDIES AND OPTIMIZATION OF MAGNETRON WITH DIFFRACTION OUTPUT (MDO) USING PARTICLE-IN-CELL SIMULATIONS

by

Alireza Majzoobi
B.Sc. September 2007, Sharif University of Technology, Iran
M.Sc. October 2011, University of Tehran, Iran

A Thesis Submitted to the Faculty of
Old Dominion University in Partial Fulfillment of the
Requirements for the Degree of

MASTER OF SCIENCE

ELECTRICAL AND COMPUTER ENGINEERING

OLD DOMINION UNIVERSITY
December 2015

Approved by:

_____
Ravindra P. Joshi (Director)

_____
Linda Vahala (Member)

_____
Shu Xiao (Member)

## ABSTRACT

NUMERICAL STUDIES AND OPTIMIZATION OF MAGNETRON WITH DIFFRACTION OUTPUT (MDO) USING PARTICLE-IN-CELL SIMULATIONS

Alireza Majzoobi
Old Dominion University, 2015
Director: Dr. Ravindra P. Joshi

The first magnetron as a vacuum-tube device, capable of generating microwaves, was invented in 1913. This thesis research focuses on numerical simulation-based analysis of magnetron performance. The particle-in-cell (PIC) based MAGIC software tool has been utilized to study the A6 and the Rising-Sun magnetron structures, and to obtain the optimized geometry for optimizing the device performance. The A6 magnetron is the more traditional structure and has been studied more often. The Rising-Sun geometry, consists of two alternating groups of short and long vanes in angular orientation, and was created to achieve mode stability.

The effect of endcaps, changes in lengths of the cathode, the location of cathodes with respect to the anode block, and use of transparent cathodes have been probed to gauge the performance of the A6 magnetron with diffraction output. The simulations have been carried out with different types of endcaps. The results of this thesis research demonstrate peak output power in excess of 1GW, with efficiencies on the order of 66% for magnetic (B)-fields in the range of 0.4T - 0.42T.

In addition, particle-in-cell simulations have been performed to provide a numerical evaluation of the efficiency, output power and leakage currents for a 12-cavitiy, Rising-Sun magnetron with diffraction output with transparent cathodes. The results demonstrate

peak output power in excess of 2GW, with efficiencies on the order of 68% for B-fields in the 0.42T - 0.46T range. While slightly better performance for longer cathode length has been recorded. The results show the efficiency in excess of 70% and peak output power on the order of 2.1GW for an 18 cm cathode length at 0.45T magnetic field and 400 kV applied voltage. All results of this thesis conform to the definite advantage of having endcaps.

Furthermore, the role of secondary electron emission (SEE) on the output performance of the12-cavity, 12-cathodes Rising-Sun magnetron has been probed. The results indicate that the role of secondary emission is not very strong, and leads to a lowering of the device efficiency by only a few percentage points.

This thesis is dedicated to my beloved wife, Sara Salimizadeh, who it would have not been possible for me to get to this point without her great sacrifices and patience. I will love you forever and for always.

## ACKNOWLEDGMENTS

First and foremost, I would like to express my sincere gratitude to my advisor, Prof. Ravindra P. Joshi, for his valuable academic guidance, encouragement and continuous support throughout my research and study. His guidance helped me in my research and the writing of this thesis.

Besides my advisor, I would like to cordially thank my committee members, Prof. Linda Vahala and Prof. Shu Xiao, for reviewing my thesis and providing helpful comments and suggestions. My thanks also goes to Dr. Popescu, G.P.D. of E.C.E. Department, who helped me in the process of my defense and graduation.

I deeply thank my parents and my sister for their endless love, unconditional support and encouragement. Words cannot express how grateful I am to them for all of the sacrifices, supports and encouraging me with their best wishes.

A special thanks to my wonderful wife. I know I have dedicated all the times which belongs to you to my research and I cannot thank you enough for your patience and sacrifices throughout this recent years. Thanks for your moral support and encouragement.

Finally, I would also like to thank all my dear friends at Old Dominion University and in Virginia for all these years.

# TABLE OF CONTENTS

Page

# LIST OF FIGURES

Figure Page

Figure Page

Figure Page

# CHAPTER 1

# INTRODUCTION

## 1-1 Brief History of Magnetrons

The first magnetron as a vacuum-tube device with perpendicular E-field and B-field (cross-fields), capable of generating microwaves, was invented by Arthur Hull in 1913. The initial devices with the power levels of 100 W were built in 1920s and 1930s [8]. This device uses the interaction of a stream of electrons with a magnetic field while moving past a series of open metal cavities called cavity resonators. Bunches of electrons passing by the openings to the cavities excite radio wave oscillations in the cavity, much as a guitar's strings excite sound in its sound box. The frequency of the microwaves produced, called the resonant frequency, is determined by the cavities' physical dimensions. Unlike other microwave tubes, such as the klystron and traveling-wave tube (TWT), the magnetron cannot function as an amplifier to increase the power of an applied microwave signal. It serves solely as an oscillator, generating a microwave signal from direct current power supplied to the tube.

In 1940, John Randall and Harry Boot introduced the first cavity magnetron. They were able to get 10kW output power using this cavity magnetron [9]. The early magnetron suffered from poor frequency stability which was resolved by strapping method and invention of Rising-Sun geometry after World War II [8, 10]. The invention of pulsed power technology led to the development of relativistic magnetrons which work at higher currents by pulsed power and cold cathode technology. The relativistic magnetron is the conventional magnetron which works with high current generated by high voltages. The

first relativistic magnetrons reached the powers in the order of 900 MW, while the output power of conventional magnetrons was about 10MW at that time [8].

Several groups, such as those at the Massachusetts Institute of Technology (MIT), have successfully produced Megawatt output power from relativistic magnetrons. The MIT A6 was one of the most popular relativistic magnetron in 1970s which has become a standard geometry for simulation and experimental researches in this area. This famous magnetron had a solid cathode design. However, more recently, a research group at the University of New Mexico introduced an A6 magnetron with a transparent cathode [11] for faster start-up that helps produce much shorter microwave pulses for ultra-wideband applications.

### 1-2 Basic Operation of Magnetron

The magnetron is basically a cross-field device, which means that the applied magnetic field and electric field are orthogonal to each other. In cross-field devices, the electrons that supply the energy to generate the microwaves are emitted directly from the cathode (or series of cathodes) in the interaction region. As a result, these devices are basically compact and no external component for generation of beam is required. The very simple and basic geometry of a magnetron consists of two parallel conductors with a DC electric field ($E$) applied between them, and a magnetic field ($B$) applied parallel to the surfaces of the conductors. Upon the application of a high voltage between the anode and cathode, explosive emission occurs on the surface of cathode, and electrons are ejected. The speed of electrons generated in the gap is given by Equation (1.1) below as:

$$V_d = \frac{E \times B}{|B|^2} \quad . \tag{1.1}$$

Equation (1.1), given above, shows that the electrons move in an azimuthal direction with a speed |E|/|B|. As the applied voltage between anode and cathode increases, the radius of electrons trajectory increases.

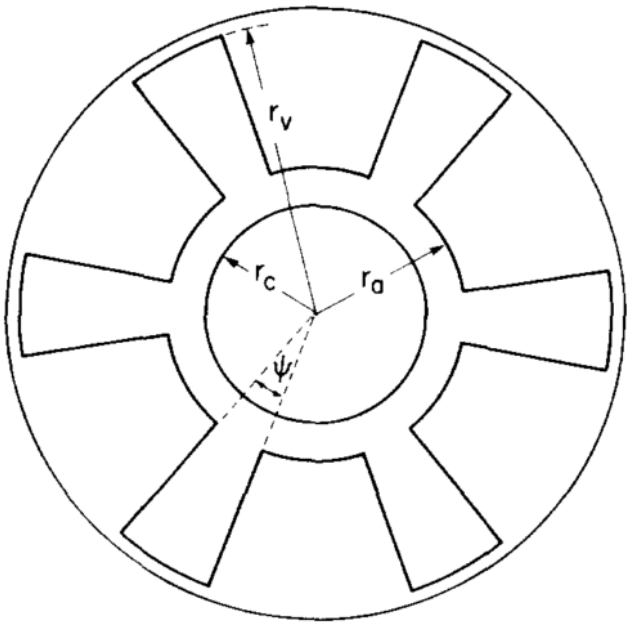


Figure 1-1. Basic configuration of a cylindrical magnetron [1].

Figure 1-1 shows the basic geometry of a cylindrical magnetron. The cathode with radius $r_c$ is separated by a gap from the anode which is shown to have a radius $r_a$. The gap area contains the drifting electrons in operation of magnetron. Also, clearly shown in the Figure 1-1, $r_v$ is the vane radius.

The Hull cutoff and Buneman-Hartree (B-H) conditions are two important regimes based on appropriate equations which specify the operating region of magnetrons. For a given voltage, the applied magnetic field should be enough for generation of initial

electrons around the cathode without getting any breakdown in the gap. In addition, the magnetic field should not be so large that it might reduce the speed of electrons based on Equation (1.1). The critical magnetic field (H) to prevent breakdown of the anode-cathode interaction region in a magnetron is called the Hull field. In the case of an axial field this critical field is given by Equation (1.2) below as:

$$B^* = \frac{mc}{ed_e}(\gamma^2 - 1)^{1/2} \quad , \tag{1.2}$$

where, $m$ and $e$ are the mass and charge of the electron, respectively, and $c$ is the speed of light. The relativistic factor, $\gamma$, and the effective gap in cylindrical geometry, $d_e$, is given by Equations (1.3) and (1.4), respectively as detailed below:

$$\gamma = 1 + \frac{eV}{mc^2} = 1 + \frac{V\,(kV)}{0.511} \quad , \tag{1.3}$$

$$\text{and, } d_e = \frac{eV}{mc^2} = 1 + \frac{r_a^2 - r_c^2}{2r_a} \quad , \tag{1.4}$$

$V$ is the anode-cathode voltage in Equation (1.3) while $r_a$and $r_c$ are the radii of the anode and cathode in Equation (1.4).

If a magnetron is designed properly, then there are values of electric and magnetic field which satisfy the Hull Cutoff condition, known as the Buneman-Hartree (B-H) condition and specified by Equation (1.5) below [8]. This B-H condition is:

$$\frac{eV}{mc^2} = \frac{e\,B_z\omega_n}{mc^2 n} r_a d_e - 1 + \sqrt{1 - \left(\frac{r_a\omega_n}{cn}\right)^2} \quad , \tag{1.5}$$

where, $\omega_n$ is the operating frequency in radians per second and $B_z$ is the applied axial magnetic field.

When the field from the axial current flow, $I_z$, becomes significant, which happens for large currents od long cathodes, the Buneman–Hartree condition is modified to Equation (1.6) [8] and expressed as follows:

$$\frac{eV}{mc^2} = \frac{e\,B_z\omega_n}{mc^2 n} r_a d_e - 1 + \sqrt{\left(1 + b_\varphi^2\right)\left[1 - \left(\frac{r_a\omega_n}{cn}\right)^2\right]} \quad , \tag{1.6}$$

where $b_\varphi = \frac{I_z\,(kA)}{8.5} = \ln\left(\frac{r_a}{r_c}\right)$ . (1.7)

Figure 1-2 depicts the general Hull cutoff and Buneman–Hartree curves. As it has been shown in the figure there is a region which satisfies both the Hull cutoff and Buneman–Hartree conditions and for a particular applied voltage, the magnetron will oscillate only if the applied magnetic field is bound between the two curves.

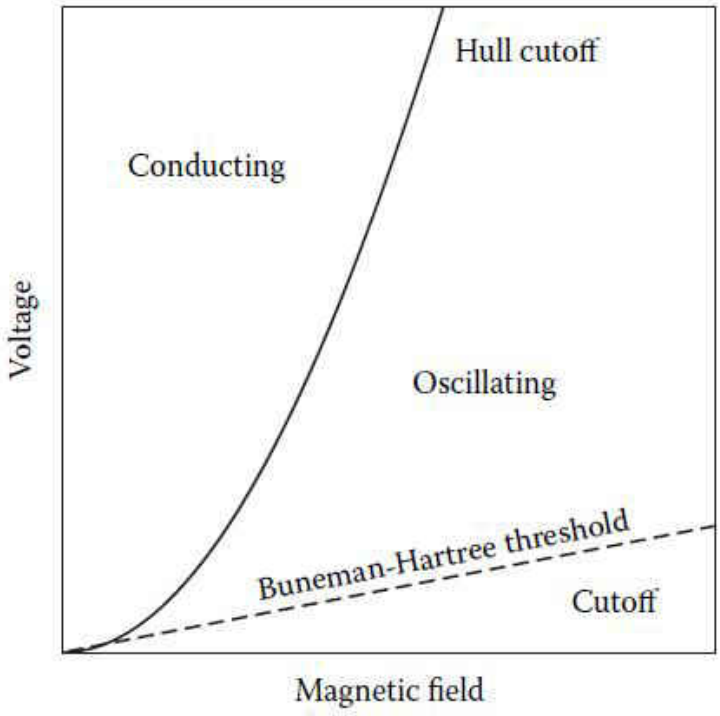


Figure 1-2. General representation of magnetron operation domain (Hull cutoff and Buneman-Hartree curves) [8].

## 1-3 Outline of Thesis

This thesis describes the results of Particle-In-Cell (PIC) simulations based on the MAGIC software tool for A6 magnetron with diffraction output (MDO) with transparent cathode. The use of transparent cathodes was recently suggested as a way to reduce the start-up time of magnetron devices and thus enable the generation of ultrashort pulses microwave pulses. Such short pulses have application in ultrawideband radar systems. Furthermore, this thesis research includes simulation studies of a 12-cavity ″Rising-Sun″ magnetron with axial diffraction output. In addition, the role of endcaps and variations in the length of cathodes for enhanced microwave performance in these devices is probed in this study. The thesis is organized as follows. Chapter 1 provides a very brief history of magnetrons and an outline of the thesis research work including the salient goals and objectives. Chapter 2 discusses the theory of operation and design challenges of the MDO and the compact MDO. Chapter 3 presents as a comprehensive overview of the computational tools and methods, and the Particle-In-Cell (PIC) approach which have been used for simulation in this thesis. In addition, this chapter provides an overview of MAGIC simulation tool and describes the geometry of the magnetrons which have been simulated in this thesis. Chapter 4 details the results obtained and a discussion along with pertinent analysis. Chapter 5 contains the conclusions and a summary of the research findings. Recommendations for future work are also summarized in Chapter 5.

# CHAPTER 2

# LITERATURE REVIEW AND BACKGROUND

## 2-1 The Basic A6 Magnetron

The A6 magnetron with radial output was the first relativistic magnetron invented at MIT by Bekefi, Orzechowski and Palevsky in 1970s with the capability of producing power in the Megawatt range [8].

The anode block of this device consisted of 6 sectorial 20° cavities with length $L$ = 7.5 cm, maximum radius (cavity radius) $R_{cav}$ = 4.11 cm, minimum radius (anode radius) $R_a$ = 2.11 cm, and a solid cathode radius $R_c$ of 1.58 cm. This geometry is the most successful, and the most studied relativistic magnetron to date. In addition this geometry serves as the basic conceptual structure for the magnetron with diffraction output (MDO) which has also been simulated in this thesis. Figure 2-1 shows the anode block of A6 magnetron produced at the University of New Mexico (UNM).

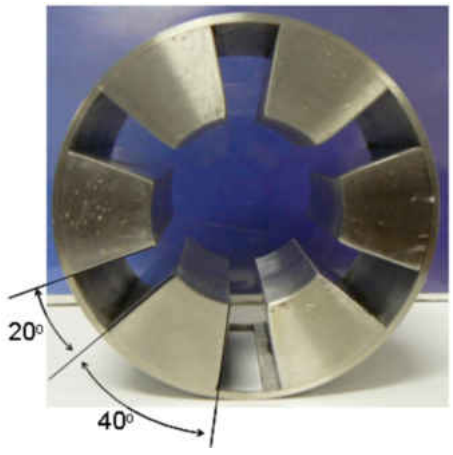


Figure 2-1. Anode block of A6 magnetron built at UNM [2].

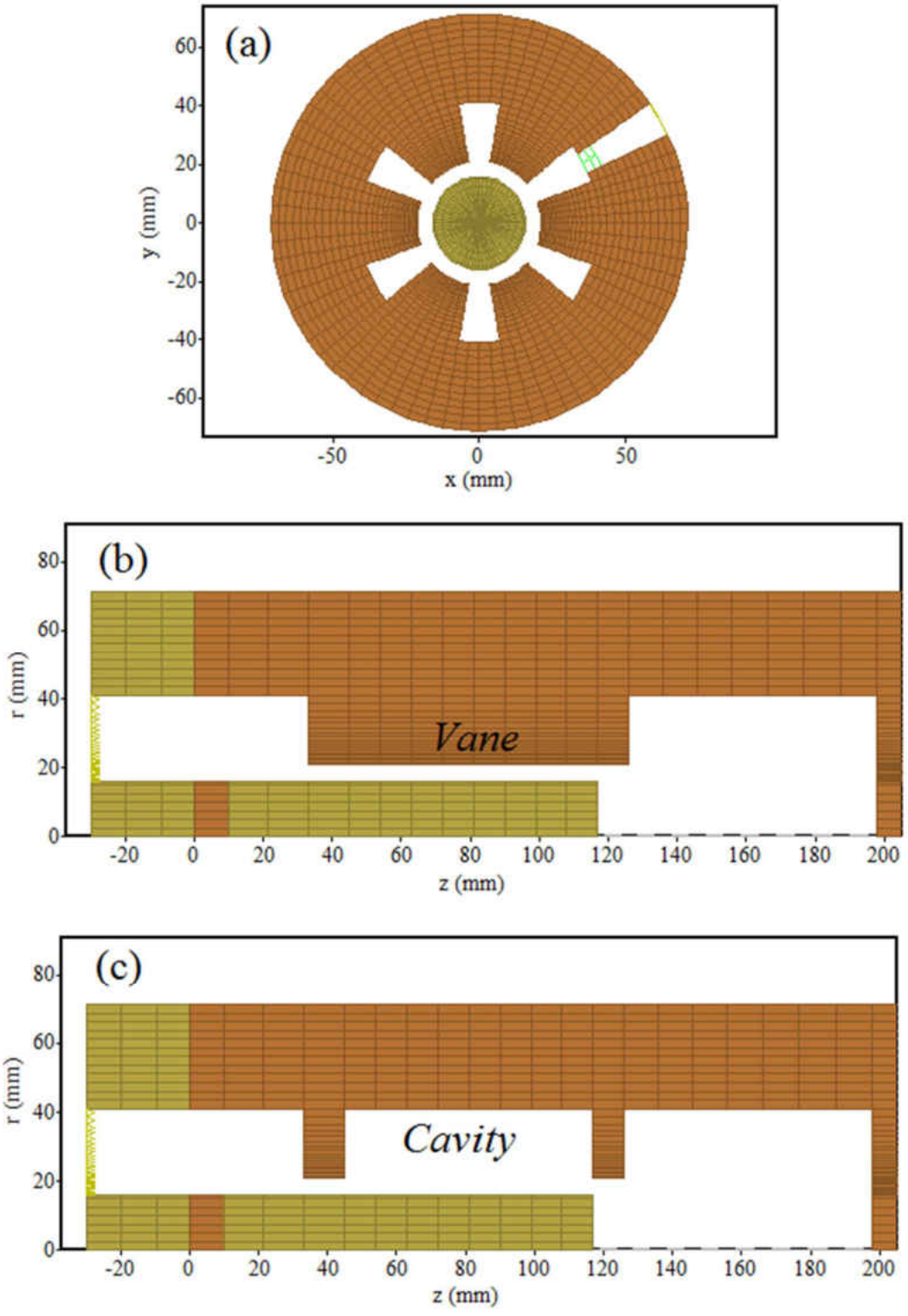


Figure 2-2. The different cross sectional view of A6 magnetron. (a) r-θ plane cross section. (b) r-z plane cross section at the θ corresponding to center of vane. (c) r-z plane cross section at the θ corresponding to center of cavity.

Figure 2-2(a) shows the cross section of A6 magnetron in $r$-$\theta$ plane. Figure 2-2(b) and Figure 2-2(c) shows the cross section of A6 magnetron in the $r$-$z$ plane at different $\theta$ angles. The vane and the cavity are visible in Figures 2-2(b) and 2-2(c), respectively.

## 2-2 Magnetrons with Diffraction Output (MDO)

While the most relativistic magnetrons extract the output power radially from a slot located in their cavities, in axial diffraction output magnetrons (also known as magnetrons with diffraction output -- MDO), the radiations extracted axially along the vanes of the anode block via a horn antenna or multiple waveguides. In a MDO, the vanes of the anode block are continued and tapered within inside of a conical horn antenna. The vanes and cavities of the MDO are tapered smoothly up to a radius that exceeds the cutoff radius of regular cylindrical waveguide. Tapering works to improve impedance matching and allows enhanced power transfer. Compared to the relativistic magnetron with radial extraction, MDO offers advantages such as compact structure, azimuthal symmetry, and high output power. Other benefits of the MDO include a strong resistance to microwave breakdown, more compact systems for producing the magnetic fields, and the ability to select any eigenmode without mode hopping.

The first sample of axial diffraction output relativistic magnetron was tested by Mikhail Fuks in Russia in the late 1970s. But the efficiency of this original MDO was about 12%-13% at that time [11]. Figure 2-3 shows this early sample of relativistic magnetron with axial output. In addition, Figure 2-4 depicts the schematic diagram of this type of magnetron introduced by Fuks.

Figure 2-3 Photograph of the early sample of diffraction output relativistic magnetron [3].

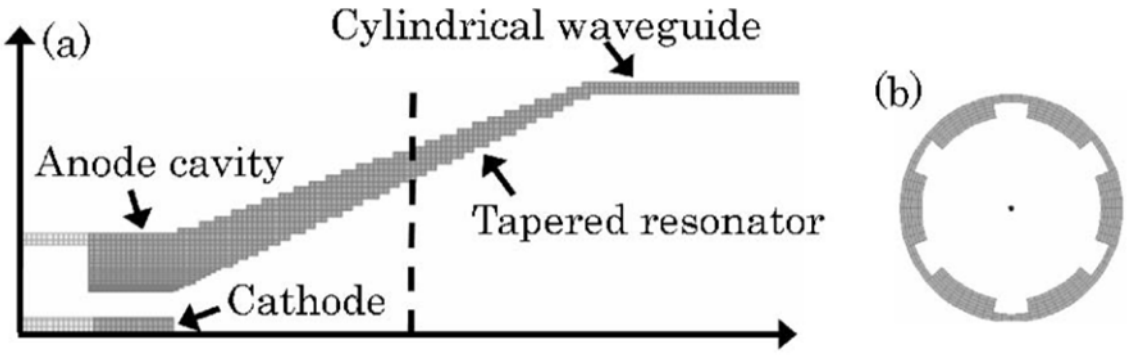


Figure 2-4. Geometry of early Russian MDO. (a) The z-r cross section, (b) the r-$\varphi$ cross section obtained at the dashed-line position [4].

This type of magnetron was considerably improved in 2007 when Daimon and Jiang at the Nagaoka University of Technology in Japan, introduced a new geometry for the MDO [4]. Figure 2-5 shows the geometry of this modified version of MDO by this Japanese group. The performance of this new geometry was studied for different amount of angle for $\varphi_0$ where $\varphi_0 = 9.5^{\circ}$ corresponds to the conventional configuration (Figure 2-4).

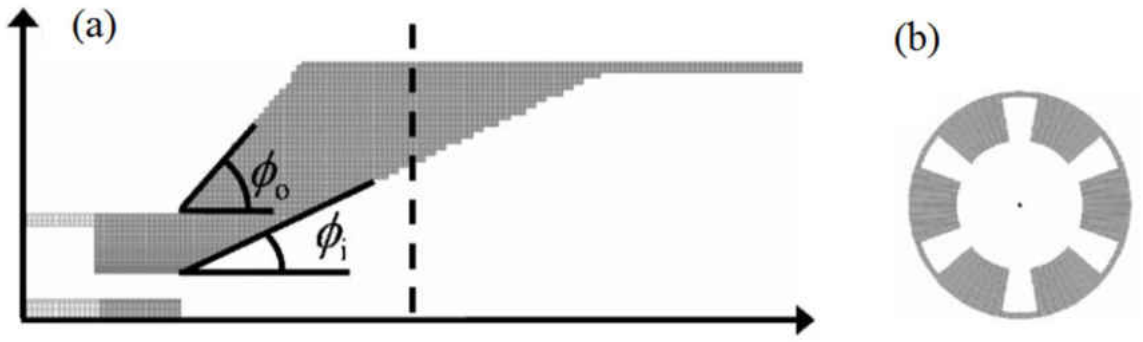


Figure 2-5. The Japanese modified configuration. (a) The z-r cross section, (b) the r-$\varphi$ cross section obtained at the dashed-line position [4].

Figure 2-6 shows the dependence of output power and efficiency of Japanese modified MDO on the value of $\varphi_0$. The results of research showed this type of MDO with output power of about 130 MW, 810 MW and 1050 MW, as well as the efficiency about 3%, 23% and 37% for $\varphi_0$ equal to $9.5^{\circ}$, $12.5^{\circ}$ and $30^{\circ}$, respectively [4]. Thus, the Japanese group optimized the geometry of MDO to produce up to 37% efficiency and about Gigawatt (GW) of output power.

This research was continued by Fuks and Shcamiloglu at the University of New Mexico to improve the MDO geometry. Their simulation studies demonstrated the attainment of efficiencies up to 70% with over 1GW output power based on simulations that used the MAGIC software tool [3]. Figure 2-7 shows the proposed geometry by UNM research group. The different values for angles α and ß were tested to obtain the optimized angles for having the highest output power and efficiency. Figure 2-8 depicts the dependence of output power and efficiency on angles α and ß. The results show the magnetron has the best performance at angles 17.5° and 32° for α and ß respectively [3]. These values have been considered as the basic assumption for the simulated geometry in this thesis.

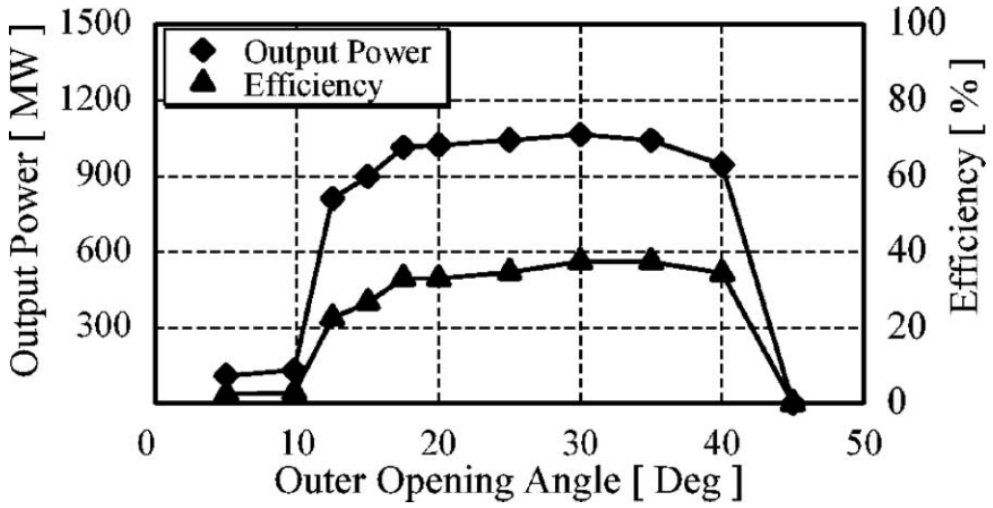


Figure 2-6. Output power and efficiency of Japanese modified MDO for different values of angle $\varphi_0$ [4].

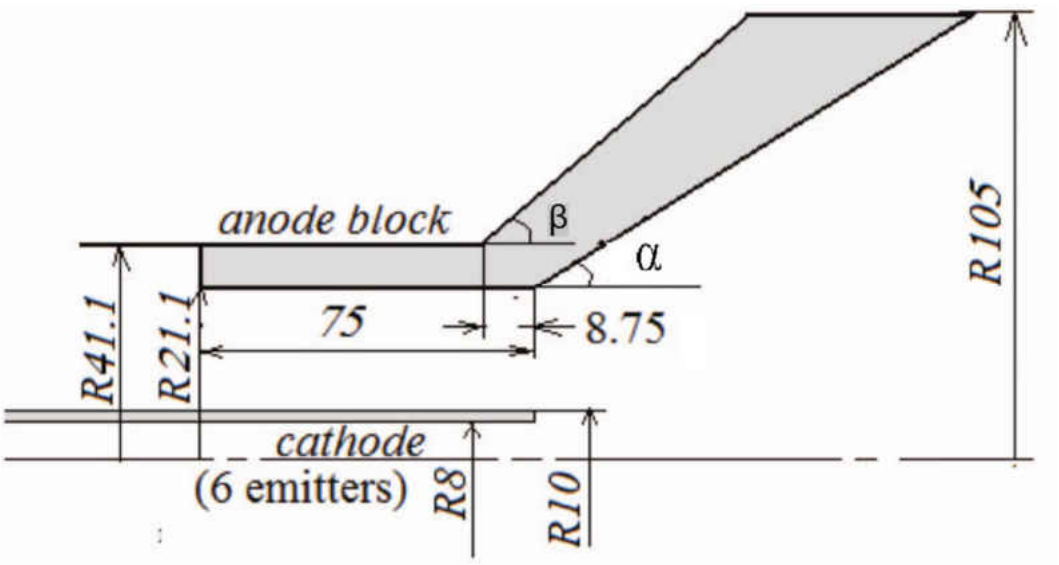


Figure 2-7 Optimized MDO by University of New Mexico research group [2].

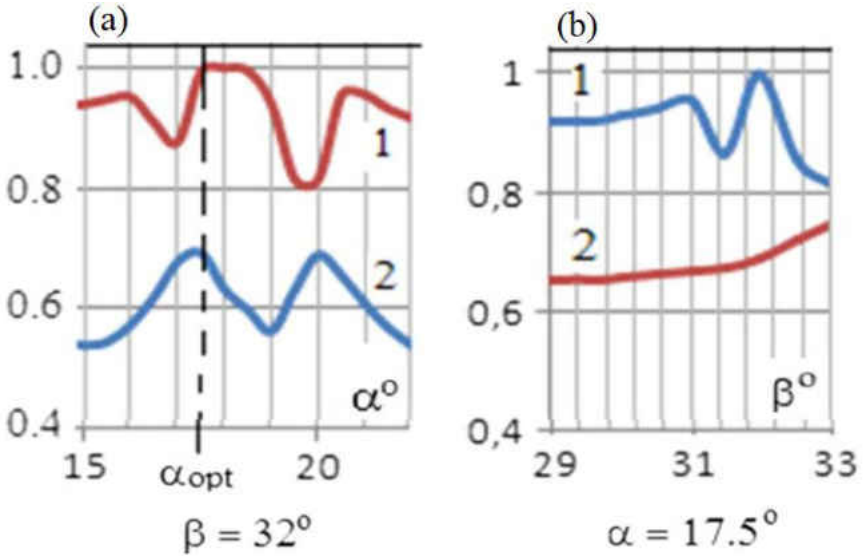


Figure 2-8. Dependence of radiation power P/Pmax (1) and efficiency (2) of UNM MDO on vanes angles. (a) angle α (b) angle ß [3].

## 2-3 Rising-Sun Magnetrons

In the context of magnetron development, the Rising-Sun configuration was created and designed in the 1940s to achieve mode stability [12, 13]. This device geometry consists of

two alternating groups of short and long vanes in angular orientation, that helped create greater frequency separation between the modes and prevent mode competition. Another feature of this configuration is that it enables mechanical frequency tenability [8, 14-16]. Since increasing the number of resonators decreases mode separation, conventional magnetrons cannot be used with a large number of resonators, and so this is an aspect where the Rising-Sun geometry would be particularly useful. Not only does this geometry have fabrication advantages over designs employing strapping, [10] its multi-cavity structure can support a number of distinct standing-wave modes. Of these, the π-mode is nondegenerate with only one field distribution at its excitation frequency, and hence preferred for some applications. The device manufacture for the Rising-Sun magnetron though could be a bit more complicated.

Since the invention of the Rising-Sun magnetron in 1940s, the various geometries for the Rising-Sun magnetron have been introduced and their performance has been analyzed [14, 17-21]. Figure 2-9 depicts the different Rising-Sun geometries which have been studied as examples.

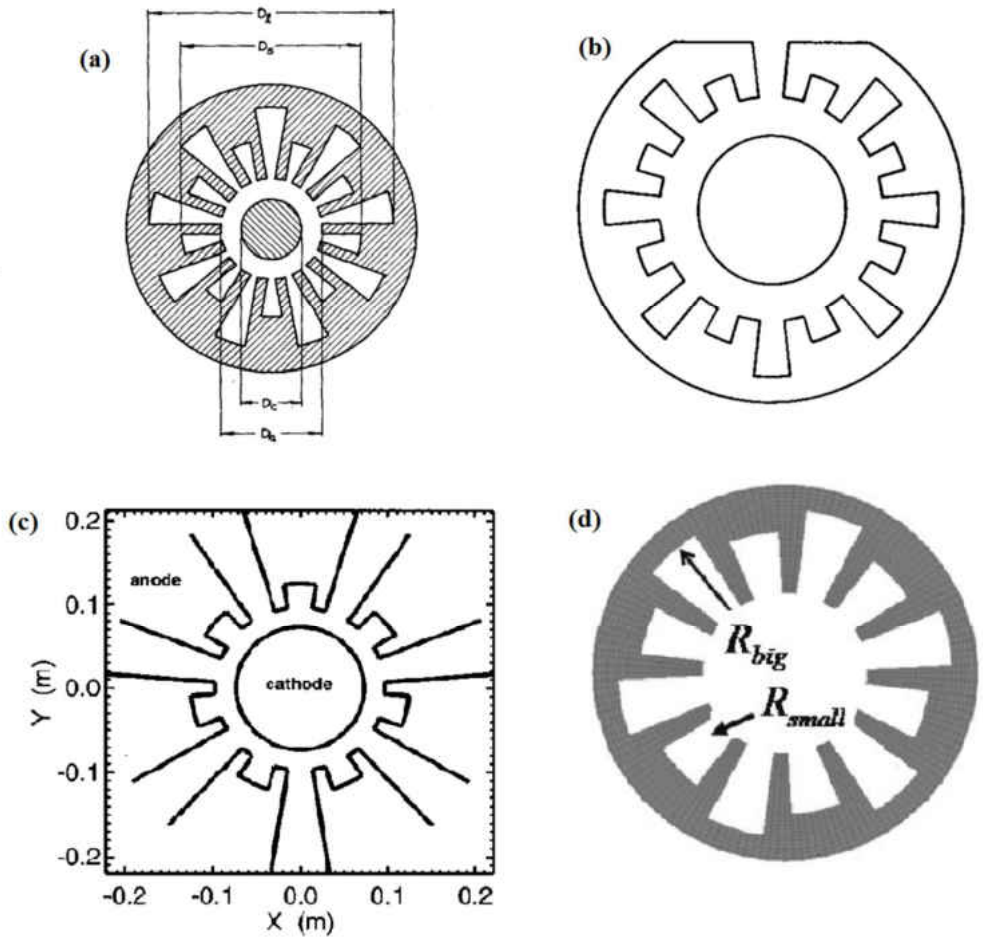


Figure 2-9. Samples for different Rising-Sun anode block geometry. (a) Hollenberg et al. in 1948 [12], (b) Todd et al. in 1988 [14], (c) Lemek et al. in 2000 [18], and (d) Liu et al. in 2014 [21].

## 2-4 Using Endcap for Magnetrons

The use of cathode endcaps has been one of the performance enhancing aspect studied both through experiments and simulations [22, 23]. The physics associated with the improvement is based on two aspects. First, the metallic endcaps shape the electric fields and help define the effective electrical length of the cathode. Without such endcaps, the finite size of the magnetron anode block could give rise to competition between different axial modes. In addition, by extending the cathode length beyond that of the anode via such

endcaps, electron leakage currents can be suppressed [5]. One contributing factor towards leakage current suppression is the reduction in the electron swarm width, due to the influence of radial electric fields on the particle trajectories along the extended cathode. Furthermore, the axial electric fields of the electron space charge that fills the interaction space and the azimuthal magnetic field can provide a negative radial drift for electrons that may be leaving the interaction space. Furthermore, the endcap protects the output window of the MDO from electron bombardment [5]. Figure 2-10 shows the picture of endcap tested at the University of New Mexico.

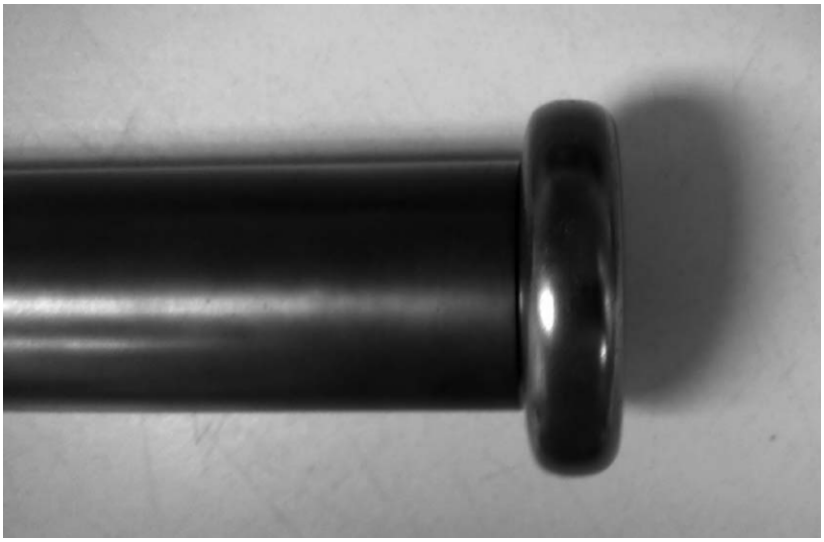

Figure 2-10. Photograph of endcap on solid cathode [5].

## 2-5 Magnetron Priming

Performance improvements in output power, efficiency, and mode purity in relativistic magnetrons are the most prominent issues in this research area. Priming is one of the most important and effective class of techniques that has been introduced for magnetron performance improvement. These techniques include magnetic priming, cathode priming,

and electrostatic priming. Priming is a technique whereby electrons are pre-bunched into the desired number of rotating electron spokes in a magnetron. For pulsed-power-driven magnetrons the driving power is only available to the magnetron for ten to a few hundred nanoseconds. So, in order to utilize the energy, the magnetron needs to operate in the desired mode as quickly as possible. As the magnetrons are usually slow to start oscillating, considerable attention has recently been given to the different methods for achieving rapid start up. Basically, the start of RF oscillations is dependent on the azimuthal RF electric field,$E_\theta$. Researchers have studied different techniques of priming and cathode configurations, such as the use of transparent cathodes and specially shaped cathodes, to decrease the rise time and achieve better mode control in relativistic magnetrons [24-28].

### *2-5-1 Cathode Priming*

The cathode priming technique uses discrete regions of electron emission periodically arranged along the azimuth of a solid cathode surface. Priming of a radiation source always involves some external means by which the desired operating mode is preferentially excited. Radio frequency priming is another priming method in which a low level external signal is injected at the same frequency of the desired operating mode. In the cathode priming method, instead of injecting an external RF signal, the cathode is prepared in such a manner that its emission geometry favors excitation of the $\pi$ mode, the usual operating mode of the relativistic magnetron [28]. This method (Cathode Priming) is much simpler and less expensive than RF priming.

For cathode priming of a six-cavity magnetron operating in the $\pi$ mode, three azimuthally periodic emitting regions on the surface of cathode should be made. Therefore,

a threefold symmetry in the electron bunches is immediately formed from the very beginning. The cathodes are fabricated using projection ablation lithography (PAL) where a KrF laser etches desired regions of surface[28].

Figure 2-11 shows the three–dimensional (3D) simulation results on this method of cathode priming which shows the faster startup in magnetron which cathode priming is applied on its cathode. This figure reveals the position of electrons after discrete times of 7.363 ns and 13.413 ns for a magnetron with and without cathode priming. As it is shown in the Figure 2-11(c) and Figure 2-11(d), the primed magnetron is operating in the $\pi$ mode, while the electrons in the magnetron with no cathode priming exhibit the characteristics of the $\frac{2\pi}{3}$ mode at 13.413 ns (Figure 2-11 (b)). Therefore, the $\frac{2\pi}{3}$ mode is suppressed during startup by cathode priming [28].

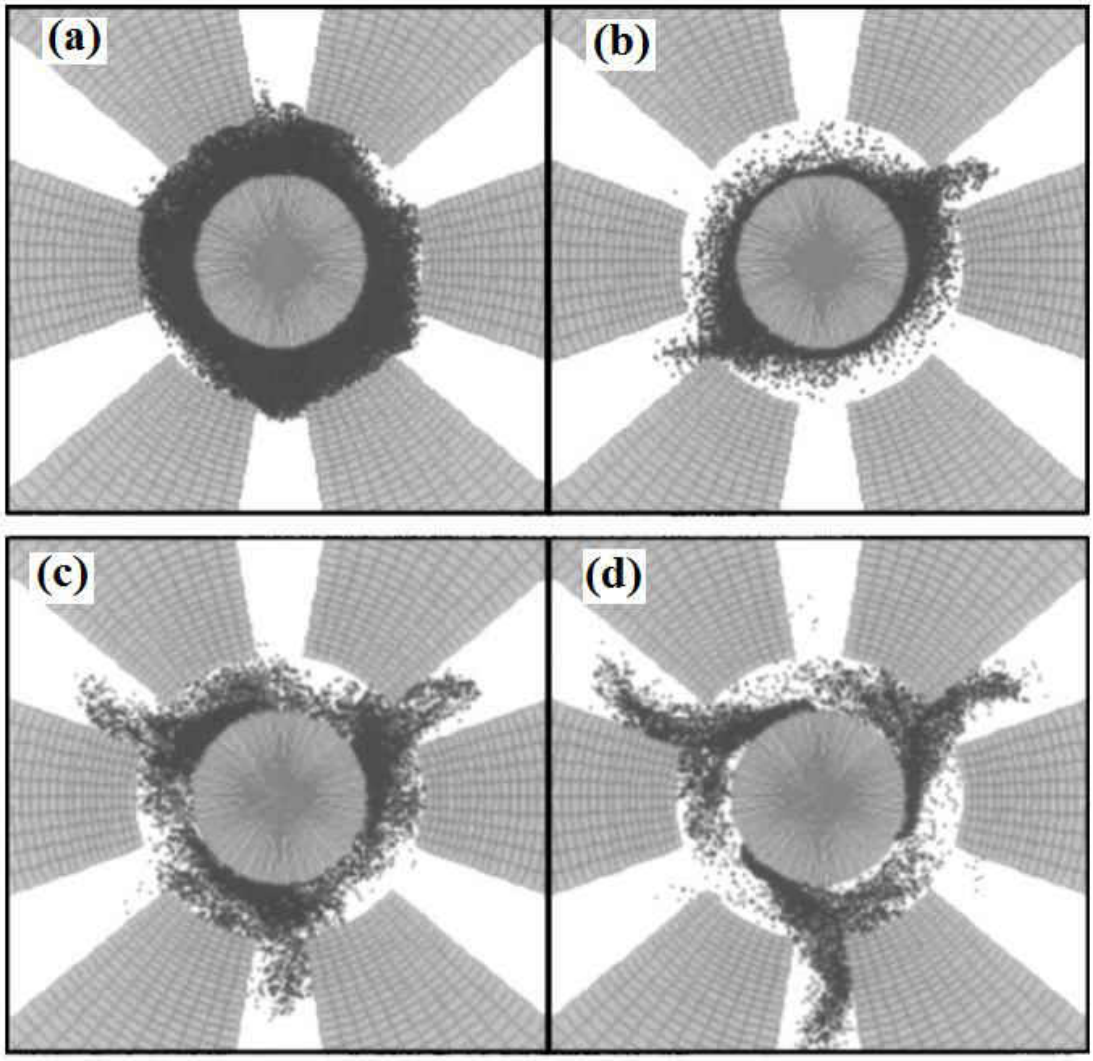


Figure 2-11. Electron positions without cathode priming for (a) t=7.363 ns and (b) t=13.413 ns. Electron positions with cathode priming for (c) t=7.363 ns and (d) t=13.413 ns [28].

### *2-5-2 Magnetic Priming*

Azimuthally varying axial magnetic fields have been utilized to perform "magnetic priming" of magnetrons for rapid startup, low noise, and mode control. Azimuthally modulated magnetic fields are used for magnetic priming, which lead to modulation of the electron sheath over the solid cathode surface. This modulation is amplified when the

sheath is moving in the periodic magnetic field. Figure 2- 12 shows the arrangement of permanent magnets used for magnetic priming.

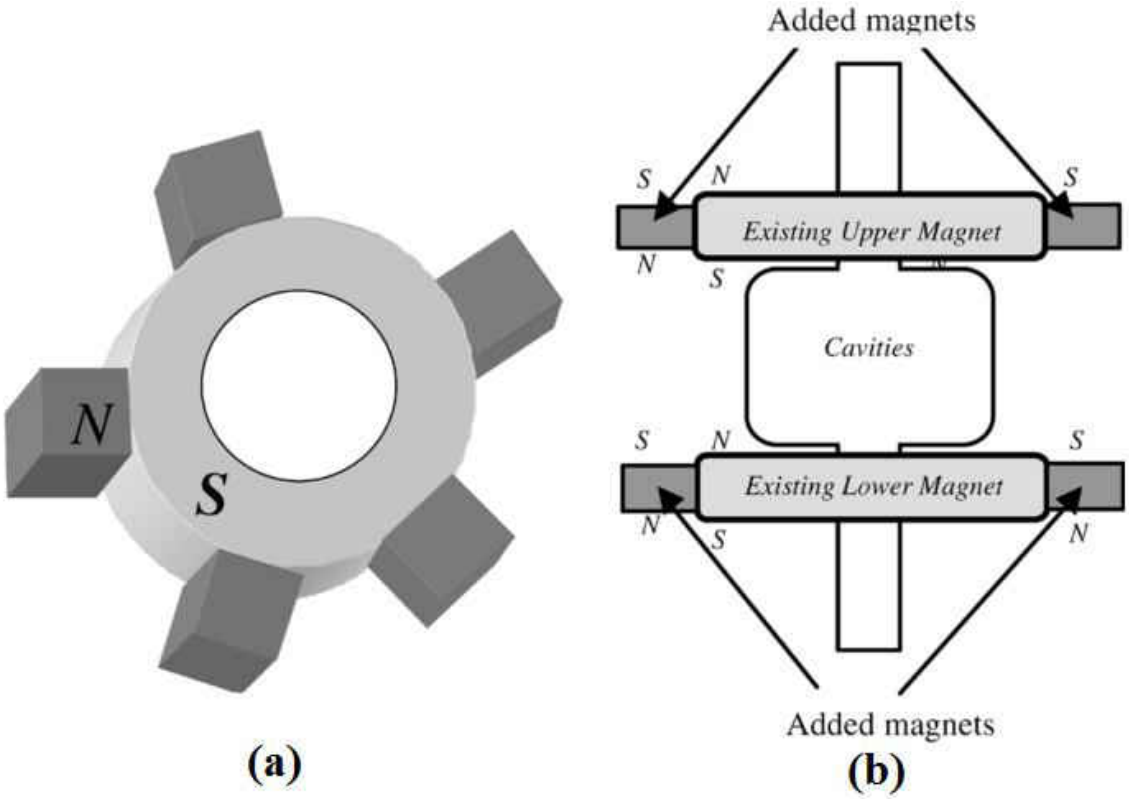


Figure 2-12. The arrangement of permanent magnets used for magnetic priming. (a) 3-D top view of the optimal magnetic priming in a Panasonic magnetron. (b) Side view of the typical axially symmetric, azimuthally varying magnetic field for a Toshiba magnetron [26].

### *2-5-3 Transparent Cathode*

The first generation of relativistic magnetrons used a uniform emission cylindrical cathode which was called a ″solid cathode″ as shown in Figure 2-13(a). The transparent cathode (Figure 2-13(b)) was proposed at University of New Mexico as a means of improving the overall performance of A6 relativistic magnetron and decreasing the start

time of oscillations. The transparent cathode is a hollow cathode with longitudinal strips of material removed in a symmetric angular fashion. As a result, the transparent cathode consists of a district number of individual emitters. The term ″transparent″ arises from the transparency of the cathode to the azimuthal component of the RF electric fields that are used as the operating modes of magnetrons.


Figure 2-13. Two different types of cathode produced at UNM. (a) Solid cathode. (b) Transparent cathode [2].

The main difference between solid and transparent cathode which affects their performance is the existence of azimuthal electric fields for the case of a transparent cathode, while the azimuthal electric fields equal zero along the surface of solid cathodes.

The simulations and experimental results show that, in addition to decreasing oscillation start time, competition between modes can be eliminated. Furthermore, the range of magnetic fields over which the A6 magnetron with a transparent cathode can operate is increased over a similar A6 device with solid cathode.

Figure 2-14 shows the geometry of A6 magnetron with transparent cathode, implemented by MAGIC, which is a particle-in-cell simulation software tool. This tool has been extensively used in this thesis research.

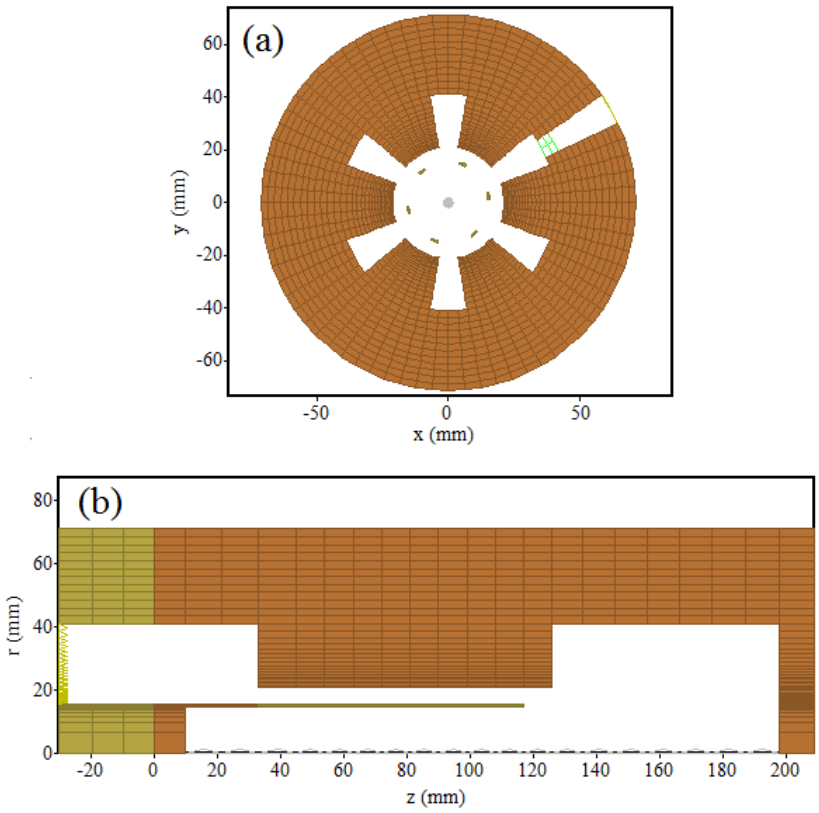


Figure 2-14. Geometry of A6 magnetron with transparent cathode. (a) *r-θ* plane cross section of A6 magnetron with transparent cathode. (b) *r-z* plane cross section of A6 magnetron with transparent cathode.

Overall then, the performance of magnetrons with a transparent cathode is improved by self-consistently and simultaneously providing three different priming techniques: cathode priming, magnetic priming, and electrostatic priming.

The cathode strips in a transparent cathode act in much the same manner as the periodic electron emitting zones generated for cathode priming which has been discussed earlier. Thus the transparent cathodes effectively provide cathode priming in magnetrons.

Figure 2-15 shows the distribution of electrons at the same time in two magnetron with the same conditions and different types of cathode. This simulation results confirm the faster build-up of the RF fields in transparent cathode (Figure 2-15(a)) compared with solid cathode (Figure 2-15(b)). As evident from the Figure 2-15, the bunching is well formed in the case of a magnetron with a transparent cathode (Figure 2-15(a)), while no spatial formation is visible with a solid cathode in Figure 2-15(b).

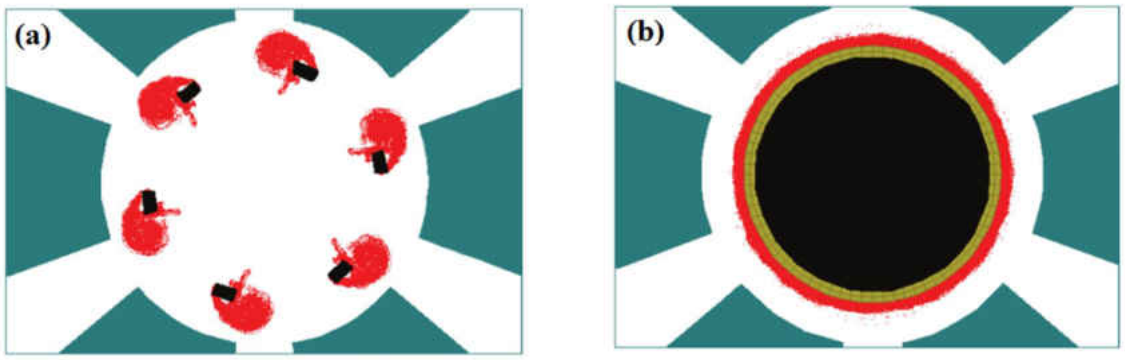


Figure 2-15. Electron prebunching in the transparent cathode. (b) Solid ring of electrons around the solid cathode [29].

In addition, a transparent cathode also self-consistently provides magnetic priming which has been discussed earlier. According to Ampere's Law, the axial currents along the longitudinal cathode strips generate azimuthal magnetic fields around the strips as shown in Figure 2-16. The magnitude of generated azimuthal magnetic fields is given by Equation (2.1) below:

$$B_{N\theta} = \frac{\mu_0 I_{Nz}}{2\pi r} \quad , \tag{2.1}$$

where $r$, is the distance from the strip center, and $I_{Nz}$ is the longitudinal current of the $Nth$ strip.

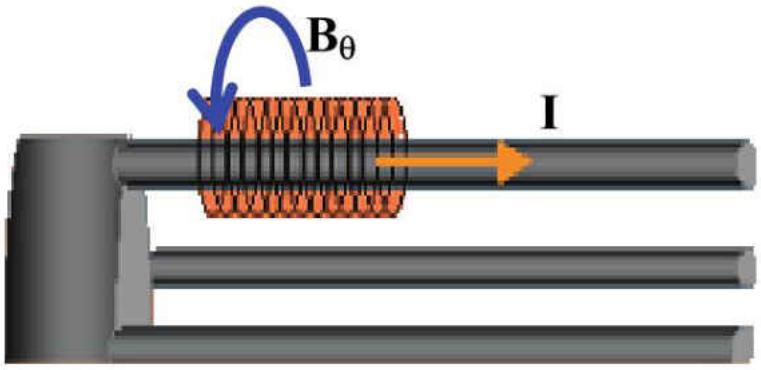


Figure 2-16. The axial current in the cathode strip and the corresponding azimuthal magnetic field lines [29].

In addition to all the aforementioned forms of priming provided by transparent cathodes, the use of such structures also increases the speed of electron flow towards the anode. In a magnetron with transparent cathode, the synchronous azimuthal RF electric field, $E_\theta$, is distributed as a modified Bessel function of the first kind of order $"n"$ [30]. Figure 2-17 shows dependence of azimuthal electric field, $E_\theta$, on the radial position for transparent and

solid cathode. As this figure shows, azimuthal electric field, $E_\theta$, goes to zero on the surface of solid cathode, while for transparent cathode, azimuthal electric field, $E_\theta$, penetrate through the cathode strips. Thus, the electron sheath region in a magnetron with transparent cathode has higher electric field magnitude as compared to the solid cathode. This fact leads to a larger radial velocity of the electrons and a faster rate of oscillation build-up [29, 30].

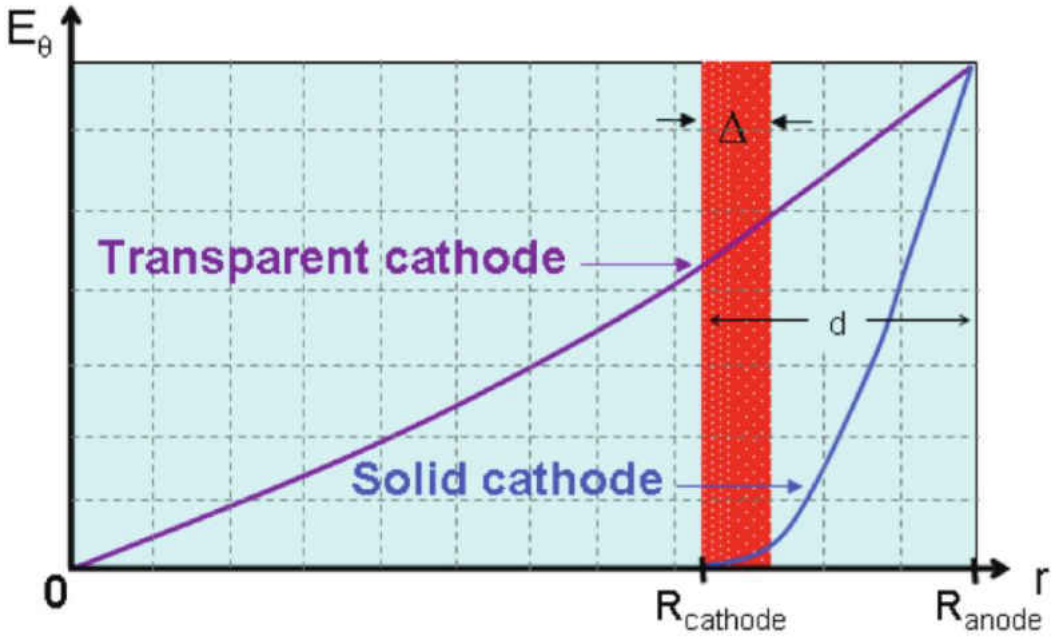


Figure 2-17. Dependencies of the azimuthal electric field of the synchronous wave on radius for a transparent and solid cathode [29].

# CHAPTER 3

# METHOD AND SIMULATION MODEL

## 3-1 Introduction on Particle-in-Cell (PIC)

The origin of Particle-In-Cell (PIC) method used in the simulation of collisionless plasmas can be traced to the early work performed by Buneman (1959) and Dawson (1960) [6]. In these basic physics models, space charge forces were included via direct solution of Coulomb's law, and charged particle trajectories were computed in periodic systems. In the first PIC simulations, the motion of 100-1000 particles and also the interactions between them, were included. Nowadays PIC codes can simulate $10^5$-$10^{10}$ particles. However, the PIC scheme was formalized and numerically coded during the 1970s. Classic texts were published by Birdsall and Langdon in 1985 and also by Hockney and Eastwood in 1981.

The PIC code simulates the motion of plasma particles and calculates all macro-quantities (like density, current density, distribution functions) from the position and velocity of these particles. This is a computational method which can be used to simulate plasmas, rarefied gases, molecular gas dynamics and other processes marked by a departure from the thermal equilibrium. In the PIC method, the gas is represented by a number of macroparticles that move in a domain described by a computational mesh. At any time, each particle is located within a mesh cell, giving the method its name [31]. The macro-force acting on the particles is calculated from the field equations. The name ″Particle-in-Cell″ has originated from the way it assigning macro-quantities to the simulation particles. PIC codes usually are classified depending on the dimensionality of the code and on the

set of Maxwell's equations used. The electromagnetic codes solve the entire set of Maxwell's equations, whereas the electrostatic codes solve only the Poisson equation.

PIC codes have a number of advantages. They represent the lowest codes, i.e., the number of assumptions made in the physical model is reduced to a minimum. They can simulate high-dimensional cases and complex geometries, while also tackling complicated atomic and plasma-surface interactions. But these advantages come at the expense of longer simulation time and computational efficiency which should be mentioned as the most important disadvantages of this technique [32].

The PIC method can be used in many applications. Applications involving fluid dynamics, plasma physics, magneto hydrodynamics, and multiphase applications all use the PIC method. Also PIC can be used to solve the problems in solid mechanics.

### 3-2 PIC Fundamentals

The general flow of the PIC scheme is shown schematically in Figure 3-1. The computational cycle of PIC starts with the charge weighting from the position of particles to the grid nodes. Also source terms, $\rho$ and $J$, for the field equations are accumulated from the continuous particle locations to the discrete mesh locations. Then, the Poisson's and Maxwell's equations are solved on the nodes in order to obtain the electric and magnetic fields. The electric and magnetic field values from the grid is weighted back to the particles and the force imposed on the particles is calculated. The particles are moved according to this force and their acceleration. In the next step, particle boundary conditions such as absorption and emission are applied. In addition, the Monte Carlo collision (MCC) scheme

is applied, if the model is collisional. The fields are then advanced one time step, and the time step loop repeats [7].

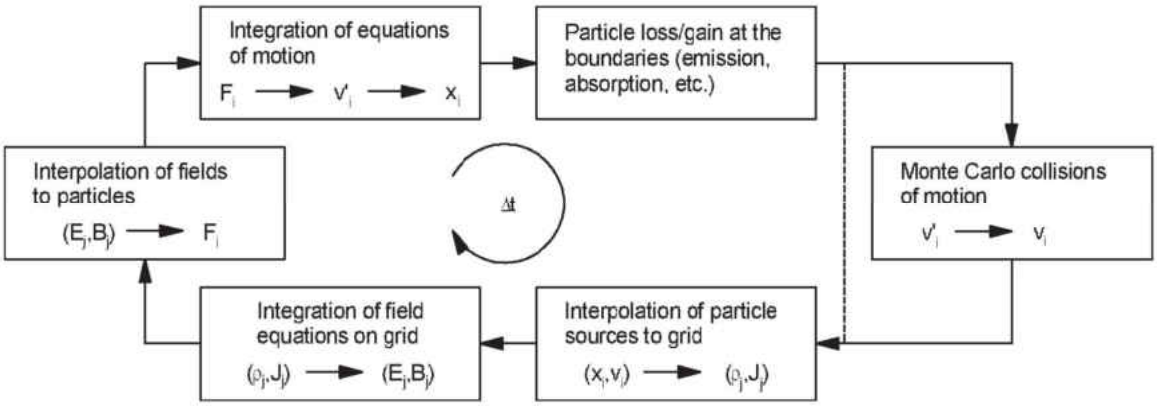


Figure 3-1. Particle-In-Cell computational cycle [6].

In the PIC method, the position and velocity of particles are defined in continuum space while the fields are defined at discrete locations in space. However, both fields and particles are defined at discrete times. Position and velocity of particle and field values are advanced sequentially in time, starting from initial conditions, with the temporal scheme shown in Figure 3-2. In this scheme which is called leap-frog scheme, particle positions and velocities are offset in time by half a time-step, i.e., $\frac{\Delta t}{2}$ .

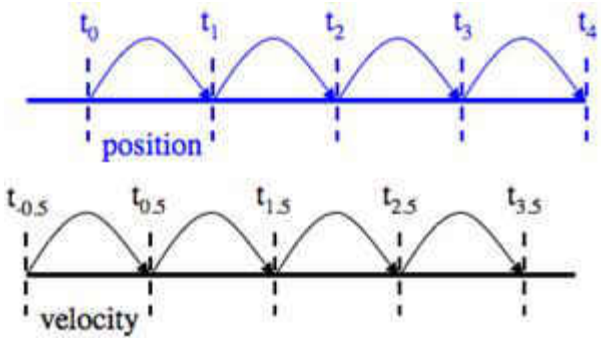


Figure 3-2. Schematic diagram of leap-frog method.

### *3-2-1 Interpolation of Particles to Nodes*

Charge density is a scalar measure spatially varying in space. It indicates the number of charge units per unit volume. It is computed by distributing charge of all particles onto the nodes of computational cells, and then dividing by the corresponding node volume.

The linear scattering operation is schematically shown in Figure 3-3(a). The charge of the simulated particle (the circle in the middle of the cell; gray particle) has been distributed amongst the nodes of the cell in which the particle lies (Hence the name for this method, particle in cell). The closest node to the particle (yellow node) receives the largest fraction of the charge and the smallest amount is contributed to the farthest node (green node).

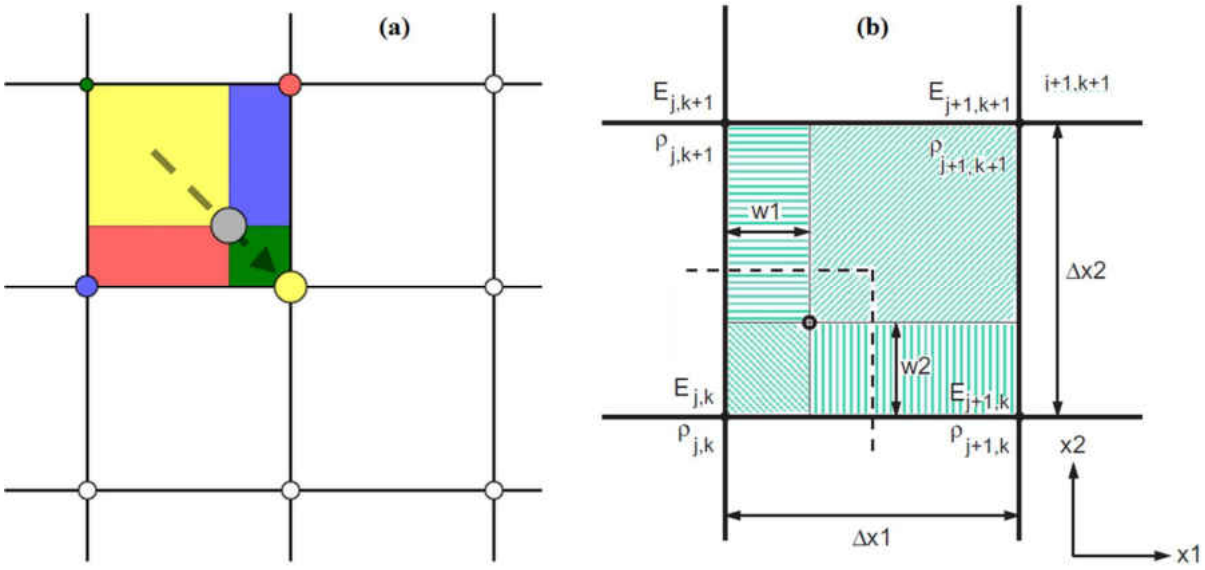


Figure 3-3. (a) Schematic of the scatter operation. (b) Graphical representation of the linear weighting on the 2-D structured Cartesian grid.

Also, a linear weighting scheme for a PIC in 2-D structured Cartesian grid $(j,k)$ is shown in Figure 3-3(b). With the same scenario which has been shown in this figure, for three dimensional Cartesian grid, weighting factor is defined as Equation (3.1).

$$w = x_i - X_{jkm} \quad , \tag{3.1}$$

where, $x_i$ refers to the position of the $i^{th}$ particle, and $X_{jkm}$ is the position of the nearest lower mesh node. It should be mentioned that, as "$i$" is considered for $i^{th}$ particle, "$j,k,m$" denote the indices of an orthogonal right-handed set of coordinates, instead of "$i,j,k$".

Thus, we can write the relations for linearly interpolating a single particle charge "$q_i$" to the surrounding nodes as follows [6, 7]:

$$Q_{j,k,m} = q_i(1-w_j)(1-w_k)(1-w_m) \quad , \tag{3.2}$$

$$Q_{j+1,k,m} = q_i(w_j)(1-w_k)(1-w_m) \quad , \tag{3.3}$$

$$Q_{j,k+1,m} = q_i(1-w_j)(w_k)(1-w_m) \quad , \tag{3.4}$$

$$Q_{j,k,m+1} = q_i(1-w_j)(1-w_k)(w_m) \quad , \tag{3.5}$$

$$Q_{j+1,k+1,m} = q_i(w_j)(w_k)(1-w_m) \quad , \tag{3.6}$$

$$Q_{j+1,k,m+1} = q_i(w_j)(1-w_k)(w_m) \quad , \tag{3.7}$$

$$Q_{j,k+1,m+1} = q_i(1-w_j)(w_k)(w_m) \quad , \tag{3.8}$$

and $$Q_{j+1,k+1,m+1} = q_i(w_j)(w_k)(w_m) \quad . \tag{3.9}$$

The charge is accumulated in this fashion for all particles. In this thesis chapter, just the linear interpolation has been explained. However, there are different methods for the gathering of particles at the nodes, such as, the nearest grid point (NGP), quadratic spline (QS) and cubic spline (CS) methods. Figure 3-4 shows weighting factor versus distance of particle from node for linear spline (LS), the quadratic spline (QS) and the cubic spline (CS).

The charge density could be calculated from Equation (3.10) given below as:

$$\rho_{j,k,m} = \frac{Q_{j,k,m}}{V_{j,k,m}} \quad , \tag{3.10}$$

where, $V_{j,k,m}$ is the volume of the cell centered on the $(j,k,m)^{th}$ mesh node, in the classical PIC scheme.

For electromagnetic models, the current is needed for Maxwell's equations. The current can be weighted by an algorithm equivalent to the charge density weighting algorithm.

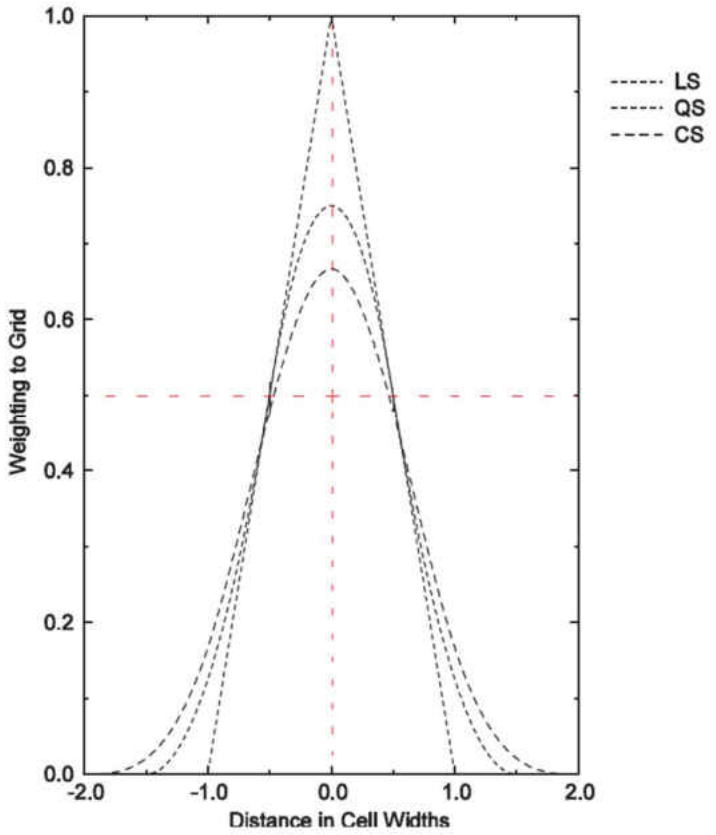


Figure 3-4. Weighting factor versus distance of particle from node for a number of interpolation schemes. LS the linear spline, QS the quadratic spline and CS is the cubic spline [6].

Based on Equations (3.1), (3.11) and (3.12), we can write the two-dimensional charge conserving currents generated in the first cell due to the particle motion shown in Figure 3-5 (Equations (3.13)-(3.16)).

$$\Delta w = w^{t+\Delta t} - w^{t} \quad , \tag{3.11}$$

$$\overline{w} = \frac{w^{t+\Delta t} + w^{t}}{2} \quad , \tag{3.12}$$

$$I_{1,x_j+\frac{\Delta x_j}{2},x_k} = \sum_i \frac{q_i}{\Delta t} \Delta w_1 (1 - \overline{w_2}) \quad , \tag{3.13}$$

$$I_{1,x_j+\frac{\Delta x_j}{2},x_k+\Delta x_k} = \sum_i \frac{q_i}{\Delta t} \Delta w_1 \overline{w_2} \quad , \tag{3.14}$$

$$I_{2,x_j,x_k+\frac{\Delta x_k}{2}} = \sum_i \frac{q_i}{\Delta t} (1 - \overline{w_1}) \Delta w_2 \quad , \tag{3.15}$$

and $I_{2,x_j+\Delta x_j,x_k+\frac{\Delta x_k}{2}} = \sum_i \frac{q_i}{\Delta t}\overline{w_1}\Delta w_2$ .

(3.16)

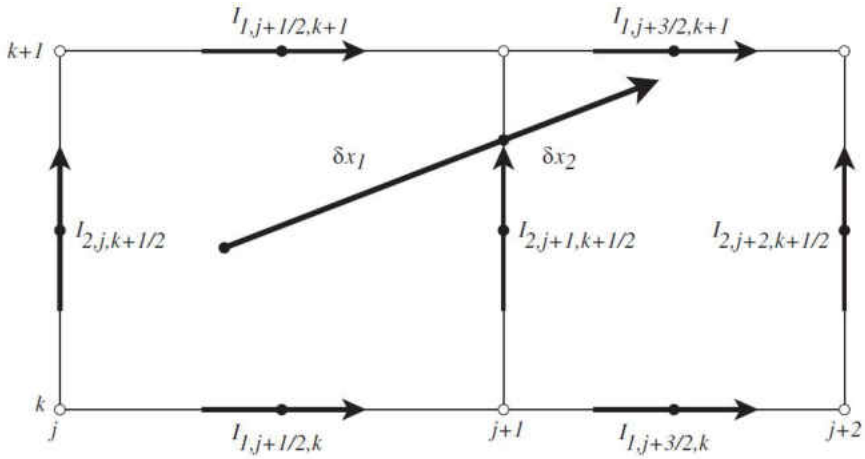


Figure 3-5. Current deposition for a multi-cell particle motion [6].

### *3-2-2 Calculation of Electric (E) and Magnetic (H) Fields*

For electrostatic models, the mesh is defined as shown in Figure 3-6. The source terms and potentials are known at grid nodes, with the electric fields often defined on the same nodes or along cell edges.

The electric field is related to the charge density by Gauss's law as follows:

$$\nabla . \mathrm{E} = \frac{\rho}{\varepsilon} \quad , \tag{3.17}$$

where, $\rho$ is charge density and $\varepsilon$ is permittivity of medium. Also, the electric field is related to the electric potential by following gradient relationship:

$$E = -\nabla\varphi \quad . \tag{3.18}$$

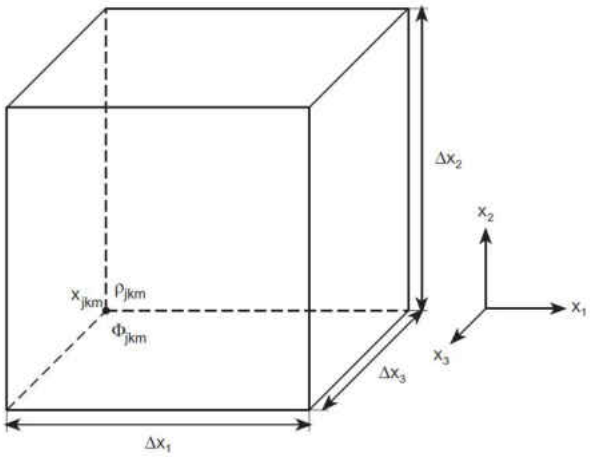


Figure 3-6. Computational mesh for electrostatic mesh [6].

Thus, after substitution of Equation (3.18) in Equation (3.17), the potential is related to the charge density by Poisson's equation as shown in Equation (3.19) below.

$$\nabla.\nabla\varphi(x,t) = \frac{-\rho(x,t)}{\varepsilon} \quad . \tag{3.19}$$

By using a center difference in a one dimensional linear homogeneous isotropic medium, Equation (3.19) becomes:

$$\frac{\varphi_{j+1}-2\varphi_j+\varphi_{j-1}}{\Delta x^2} = -\frac{\rho_j}{\varepsilon} . \tag{3.20}$$

For a system fully bounded by conductors, the charge is conserved. Thus:

$$\oint_S \varepsilon E.dS = \oint_V \rho dV + \oint_s(\sigma_0 + \sigma_J)dS \equiv 0 , \tag{3.21}$$

where $S$ is the surface enclosing the system and $V$ is the volume. Also $0$ and $J$ refer to boundaries of a system with spatial index $0 \leq j \leq J$. The electric field within an ideal conducting material is zero and the surface electric fields in the boundaries are equal to:

$$E_0 = \frac{\sigma_0}{\varepsilon} \quad , \tag{3.22}$$

and, $E_J = -\frac{\sigma_J}{\varepsilon}$ . (3.23)

Since a boundary condition is required in order to have a unique solution, which is usually a reference potential, for instance $\varphi_0 = 0$, is considered for one of the electrodes.

For a non-uniform orthogonal Cartesian mesh in two dimensions, Equation (3.19) can be rewritten as:

$$\frac{\varphi_{j,k+1}}{\Delta x_{k+\frac{1}{2}} \Delta \bar{x}_k} - \frac{2\varphi_{j,k}}{\Delta x_{k+\frac{1}{2}} \Delta x_{k-\frac{1}{2}}} + \frac{\varphi_{j,k-1}}{\Delta x_{k-\frac{1}{2}} \Delta \bar{x}_k} + \frac{\varphi_{j+1,k}}{\Delta y_{j+\frac{1}{2}} \Delta \bar{y}_j} - \frac{2\varphi_{j,k}}{\Delta y_{j+\frac{1}{2}} \Delta y_{j-\frac{1}{2}}} + \frac{\varphi_{j-1,k}}{\Delta y_{j-\frac{1}{2}} \Delta \bar{y}_j} = -\frac{\rho_{j,k}}{\varepsilon}, \quad (3.24)$$

where, $\Delta x_{k+\frac{1}{2}} = x_{k+1} - x_k$ , (3.25)

and, $\Delta \bar{x}_k = \frac{\Delta x_{k+\frac{1}{2}} + \Delta x_{k-\frac{1}{2}}}{2}$ . (3.26)

*3-2-2-1 Maxwell's Equations*

The differential forms of Maxwell's equations in an isotropic medium are:

$$\frac{\partial D}{\partial t} = \nabla \times H - J \quad , \quad (3.27)$$

$$\frac{\partial \mathrm{B}}{\partial \mathrm{t}} = -\nabla \times \mathrm{E} \quad , \quad (3.28)$$

$$\nabla . \mathrm{B} = 0 \quad , \quad (3.29)$$

$$\text{and } \nabla . \mathrm{D} = \rho \quad , \quad (3.30)$$

where, "$D$" is electric flux density, "$H$" is the magnetic field intensity, "$B$" is magnetic flux density, "$E$" electric field intensity, "$J$" is electric current density and "$\rho$" is electric charge density.

Also Equations (3.31)-(3.33) show constitutive relations.

$$\mathrm{B} = \mu \mathrm{H} \quad , \quad (3.31)$$

$$D = \varepsilon E \quad , \tag{3.32}$$

$$\text{and } J = \sigma E \quad , \tag{3.33}$$

where, μ is the magnetic permeability, ε is the dielectric permittivity and σ is the electric conductivity. All of the field parameters are assumed to be functions of position and time, while material parameters are functions of position.

*3-2-2-2 Finite-Difference Time Domain (FDTD) Technique*

The nature of Maxwell's differential equations is that the time derivative of the magnetic field (H) is dependent on the curl of the electric field (E), and the time derivative of the electric field is dependent on the curl of the magnetic field. These interdependent properties were the key reason for introducing the Finite-Difference Time Domain (FDTD) technique. In this technique, at any point in space, an updated value of an E/H-field in time is dependent on the stored value of the E/H-field, and the numerical curl of the local distribution of the H/E-field in space [33].

The FDTD technique was originally introduced by Yee in 1966 and is based on time and spatial discretization of Maxwell's equations to obtain solutions for the electromagnetic field in the time domain [34]. The technique is numerically implemented by continuously sampling the electromagnetic field over the wave propagation in the medium which is discretized into a grid. This grid is popularly called the Yee lattice, and is a numerical three-dimensional space lattice comprised of a multiplicity of Yee cells (Figure 3-7).

Figure 3-7 shows standard Cartesian Yee cell and helps to better understand this staggered time and space grid. As it has been shown in the picture by dashed lines, there is

$\frac{1}{2}$ time step difference between electric field (E) and magnetic field (H). Due to the central difference approximation technique in time, magnetic field is present at $t = (n + \frac{1}{2})\Delta t$, where "$n$" is an integer and electric field is known at integral multiples of the time step. These half time steps are introduced to perform the finite difference computation of electric field based on magnetic field and vice versa.

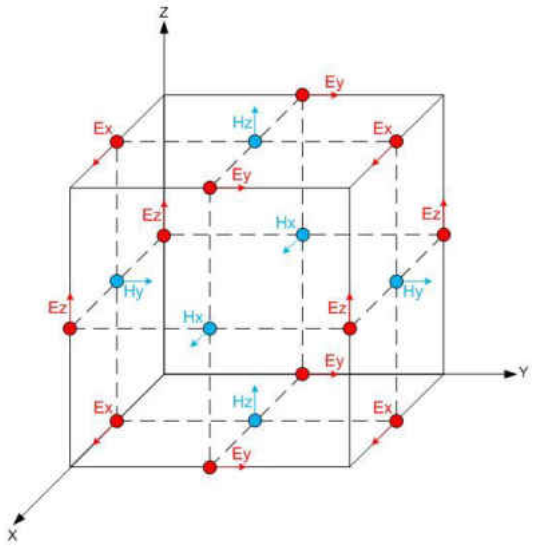


Figure 3-7. Standard Cartesian Yee cell used for finite-difference time domain (FDTD) technique.

Figure 3-7 depicts the positions of various field components. It shows the electric field components are in the middle of the edge and the magnetic field components are in the center of the surface.

After calculation of initial conditions with satisfaction of Maxwell's equations, the electric and magnetic fields are then advanced in time using finite-differenced forms of Ampere's law and Faraday's law, and Equations (3.27) and (3.28). Also, other Maxwell's equations, which were illustrated through Equations (3.29) and (3.30), remain satisfied in time.

In a rectangular coordinate system, Equation (3.27) is equivalent to the following equations:

$$\frac{\partial D_x}{\partial t} = \frac{\partial H_z}{\partial y} - \frac{\partial H_y}{\partial z} - J_x \quad , \tag{3.34}$$

$$\frac{\partial D_y}{\partial t} = \frac{\partial H_x}{\partial z} - \frac{\partial H_z}{\partial x} - J_y \quad , \tag{3.35}$$

and, $$\frac{\partial D_z}{\partial t} = \frac{\partial H_y}{\partial x} - \frac{\partial H_x}{\partial y} - J_z \quad . \tag{3.36}$$

In addition, Faraday's law, i.e., Equation (3.8) can be evaluate in the same fashion and yields:

$$\frac{\partial B_x}{\partial t} = \frac{\partial E_y}{\partial z} - \frac{\partial E_z}{\partial y} \quad , \tag{3.37}$$

$$\frac{\partial B_y}{\partial t} = \frac{\partial E_z}{\partial x} - \frac{\partial E_x}{\partial z} \quad , \tag{3.38}$$

and, $$\frac{\partial B_z}{\partial t} = \frac{\partial E_x}{\partial y} - \frac{\partial E_y}{\partial x} \quad . \tag{3.39}$$

The most common implementation of Equations (3.34) - (3.39) in PIC codes uses a center difference for the differentials and places the fields on the mesh as shown in Figure 3-7, called the leapfrog algorithm. As it mentioned, $D$, $E$ and $J$ are defined in the middle of the edges, while $B$ and $H$ are defined in the center of the surface.

The center difference form of Ampere's law, Equations (3.34)-(3.36), on a uniform orthogonal mesh become:

$$\frac{D_x^t\left(i+\frac{1}{2},j,k\right) - D_x^{t-\Delta t}\left(i+\frac{1}{2},j,k\right)}{\Delta t} = \frac{H_z^{t-\Delta t/2}\left(i+\frac{1}{2},j+\frac{1}{2},k\right) - H_z^{t-\Delta t/2}\left(i+\frac{1}{2},j-\frac{1}{2},k\right)}{\Delta y}$$

$$- \frac{H_y^{t-\Delta t/2}\left(i+\frac{1}{2},j,k+\frac{1}{2}\right) - H_y^{t-\Delta t/2}\left(i+\frac{1}{2},j,k-\frac{1}{2}\right)}{\Delta z} - J_x^{t-\Delta t/2}\left(i+\frac{1}{2},j,k\right) \quad . \tag{3.40}$$

$$\frac{D_y^t\left(i,j+\frac{1}{2},k\right)-D_y^{t-\Delta t}\left(i,j+\frac{1}{2},k\right)}{\Delta t} = \frac{H_x^{t-\Delta t/2}\left(i+,j+\frac{1}{2},k+\frac{1}{2}\right)-H_x^{t-\Delta t/2}\left(i,j+\frac{1}{2},k-\frac{1}{2}\right)}{\Delta z}$$

$$-\frac{H_z^{t-\Delta t/2}\left(i+\frac{1}{2},j+\frac{1}{2},k\right)-H_z^{t-\Delta t/2}\left(i-\frac{1}{2},j+\frac{1}{2},k\right)}{\Delta x} - J_y^{t-\Delta t/2}\left(i,j+\frac{1}{2},k\right) \quad . \qquad (3.41)$$

and, $\frac{D_z^t\left(i,j,k+\frac{1}{2}\right)-D_z^{t-\Delta t}\left(i,j,k+\frac{1}{2}\right)}{\Delta t} = \frac{H_y^{t-\Delta t/2}\left(i+\frac{1}{2},j,k+\frac{1}{2}\right)-H_y^{t-\Delta t/2}\left(i-\frac{1}{2},j,k+\frac{1}{2}\right)}{\Delta x}$

$$-\frac{H_x^{t-\Delta t/2}\left(i,j+\frac{1}{2},k+\frac{1}{2}\right)-H_x^{t-\Delta t/2}\left(i,j-\frac{1}{2},k+\frac{1}{2}\right)}{\Delta y} - J_z^{t-\Delta t/2}\left(i,j,k+\frac{1}{2}\right) \quad . \qquad (3.42)$$

In these equations, spatial and time steps are represented by the lower indices $(i,j,k)$ and the upper index$(t)$, respectively. Where *i*, *j* and *k* denote the indices of an orthogonal right-handed set of coordinates and Figure 3-8 shows the position of the electric and magnetic field components in standard a Cartesian Yee cell.

Similarly, the center-difference form of Faraday's law, Equations (3.37)-(3.39), on a uniform orthogonal mesh become:

$$\frac{B_x^{t+\Delta t/2}\left(i,j+\frac{1}{2},k+\frac{1}{2}\right) - B_x^{t-\Delta t/2}\left(i,j+\frac{1}{2},k+\frac{1}{2}\right)}{\Delta t} =$$

$$\frac{E_y^t\left(i,j+\frac{1}{2},k+1\right)-E_y^t\left(i,j+\frac{1}{2},k\right)}{\Delta z} - \frac{E_z^t\left(i,j+1,k+\frac{1}{2}\right)-E_z^t\left(i,j,k+\frac{1}{2}\right)}{\Delta y} \quad , \qquad (3.43)$$

$$\frac{B_y^{t+\Delta t/2}\left(i-\frac{1}{2},j,k+\frac{1}{2}\right) - B_y^{t-\Delta t/2}\left(i-\frac{1}{2},j,k+\frac{1}{2}\right)}{\Delta t} =$$

$$\frac{E_z^t\left(i,j,k+\frac{1}{2}\right)-E_z^t\left(i-1,j,k+\frac{1}{2}\right)}{\Delta x} - \frac{E_x^t\left(i-\frac{1}{2},j,k+\frac{1}{2}\right)-E_x^t\left(i-\frac{1}{2},j,k-\frac{1}{2}\right)}{\Delta z} \quad , \qquad (3.44)$$

and, $\frac{B_z^{t+\Delta t/2}\left(i-\frac{1}{2},j+\frac{1}{2},k\right)-B_z^{t-\Delta t/2}\left(i-\frac{1}{2},j+\frac{1}{2},k\right)}{\Delta t} =$

$$\frac{E_x^t\left(i-\frac{1}{2},j+1,k\right)-E_x^t\left(i-\frac{1}{2},j,k\right)}{\Delta y} - \frac{E_y^t\left(i-1,j+\frac{1}{2},k\right)-E_y^t\left(i,j+\frac{1}{2},k\right)}{\Delta x} \quad . \qquad (3.45)$$

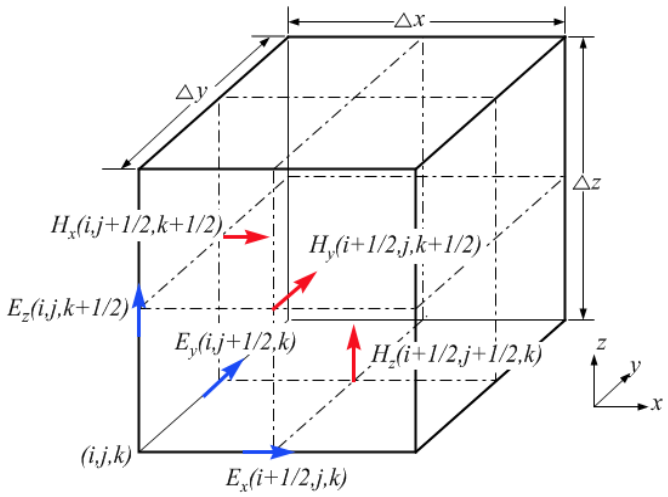


Figure 3-8. Position of electric and magnetic field components in standard Cartesian Yee cell.

The above equations are solved consecutively and the fields leapfrog forwards in time. In a leapfrog algorithm, the new amounts of filed are only dependent upon the previous field values.

Finally, after the computation of the electric and magnetic fields in the nodes, these calculated fields are interpolated to the real particles in the cells for calculation of imposed force on the particles in the next step.

*3-2-2-3 Advantages and Limitations of the FDTD Method*

Finite Difference Time Domain (FDTD) is a relatively powerful and very popular method because of its simplicity. Solving Maxwell's equations using FDTD is a simple iterative procedure and the most prominent advantage of FDTD is that this time-stepping scheme avoids the need to solve simultaneous equations, so matrix inversions are not necessary.

On the other hand, there are several limitations to the numerical implementation of the FDTD technique through the above-mentioned difference equations which have been the subject of research. Some of these restrictions force limitations on the grid size and time step increments which affect the accuracy and stability of this technique.

One of the most important restrictions is setting the maximum value for the longest side of the grid cell which should be much shorter than the shortest wavelength of the wave within the cell. A very common restriction assumed in practice is $\frac{\lambda}{10}$, where $\lambda$ is the shortest perceptible wavelength in the excitation signal [35].

The second limitation is the time-step restriction required to satisfy the Courant–Friedrichs-Levy (CFL) condition. The CFL condition is a necessary condition for stability while solving certain partial differential equations numerically by the method of finite differences.

In multiple dimensions, the Courant– Friedrichs-Levy (CFL) stability criterion on the time step is given by:

$$\frac{1}{V_{max}\Delta t} \geq \left(\sum_{i=1}^{N} \frac{1}{\Delta x_i^2}\right)^{1/2}. \tag{3.46}$$

where, the index "$i$" sums over the coordinate indices and $\Delta x_i$ denotes the grid spacing in the $i^{th}$ coordinate direction. "$N$" is the grid dimension "$V_{max}$" is the maximum wave velocity within the model.

In a three dimensional (3D) case, Equation (3.46) will be written in the following form:

$$\frac{1}{V_{max}\Delta t} \geq \left(\frac{1}{\Delta x^2} + \frac{1}{\Delta y^2} + \frac{1}{\Delta z^2}\right)^{1/2}. \tag{3.47}$$

In the case of N-dimensional isotropic cells, Equation (3.46) can be simplified to:

$$\frac{V_{max}\Delta t}{\delta} \leq \frac{1}{\sqrt{N}} \quad , \tag{3.48}$$

where the left hand side of this equation ($\frac{V_{max}\Delta t}{\delta}$) is called the Courant number. For instance in a three dimensional isotropic case, the Courant number should be less than 0.577 ($\frac{V_{max}\Delta t}{\delta} \leq \frac{1}{\sqrt{3}} \equiv 0.577$).

Different cases have demonstrated that using smaller values of $\Delta t$ does not necessarily improve the results. However, smaller values for the Courant number may sometimes yield satisfactory results [35].

Another restriction develops from the scale and geometry of the problem especially for solving of the problems which consist of very small objects compared with other large parts of geometry. As the method uses a uniform grid to model small parts of model along with large parts, the geometry imposes challenging limitations, especially in computation cost. One way to solve this problem is by using a non-uniform grid, which adds more difficulties for satisfying stability conditions such as CFL condition [35].

### *3-2-3 Position and Velocity of Particles*

The plasma or every material which is studied, is described by a number of computational particles with position "$x$" and velocity "$v$". The position and velocity of particles could be calculated based on Lorentz equation and Newton's second law of motion as follow:

$$ma = F = qE + (qv \times B) \quad , \tag{3.49}$$

where, $a = \frac{dv}{dt}$ and $v = \frac{dx}{dt}$ .

The electric and magnetic fields in Equation (3.49) have been calculated in the previous step by FDTD method. After substitution of acceleration "$a$", in Equation (3.49), the equation changes to:

$$\frac{dv}{dt} = \frac{q}{m}(E + v \times B) \quad . \tag{3.50}$$

Based on the leap-frog scheme as shown in Figure 3-9, Equation (3.50) can be rewritten as follow:

$$\frac{\boldsymbol{v}^{t+\frac{\Delta t}{2}} - \boldsymbol{v}^{t-\frac{\Delta t}{2}}}{\Delta t} = \frac{q}{m}\left(\boldsymbol{E}^{t} + \frac{\boldsymbol{v}^{t+\frac{\Delta t}{2}} + \boldsymbol{v}^{t-\frac{\Delta t}{2}}}{2} \times \boldsymbol{B}^{t}\right) . \tag{3.51}$$

Also: $\frac{dx}{dt} = v$ is written as:

$$\frac{\boldsymbol{x}^{t+\Delta t} - \boldsymbol{x}^{t}}{\Delta t} = \boldsymbol{v}^{t+\frac{\Delta t}{2}} . \tag{3.52}$$

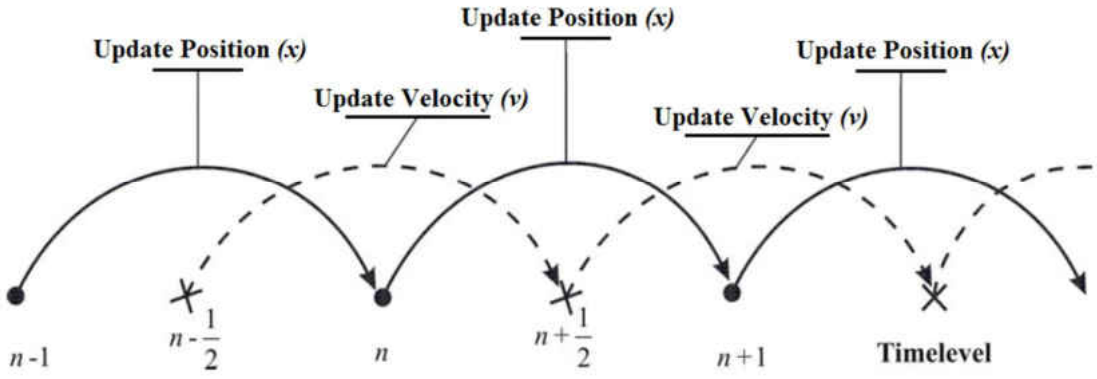


Figure 3-9. The leap frog integration scheme [7].

The stability of the leapfrog scheme can be shown for particles in simple harmonic motion:

$$a = \frac{d^2x}{dt^2} = -\omega_0^2 x. \tag{3.53}$$

With a numerical approximation of second-order derivatives, Equation (3.53) becomes:

$$\frac{d^2x}{dt^2} = \frac{(\frac{x^{t+\Delta t}-x^t}{\Delta t})-(\frac{x^t-x^{t-\Delta t}}{\Delta t})}{\Delta t} = \frac{x^{t+\Delta t}-2x^t+x^{t-\Delta t}}{\Delta t^2} = -\omega_0^2 x. \quad (3.54)$$

Solutions of Equation (3.54) are of the form

$$x^t \propto exp(-i\omega t) \quad , \quad (3.55)$$

$$\text{and } x^{t+\Delta t} \propto exp(-i\omega(t+\Delta t)) \quad . \quad (3.56)$$

Using Euler's equation ($e^{ix} = Cosx + i\,Sinx$), the finite difference becomes:

$$\sin\left(\frac{\omega\Delta t}{2}\right) = \mp\frac{\omega_0\Delta t}{2} \quad . \quad (3.57)$$

So $\omega$ has an imaginary component for $\omega_0\Delta t > 2$, indicating numerical instability and a rapidly growing instability exists for $\omega_0\Delta t > 2$. Therefore, the condition of stability is $\Delta t < \frac{2}{\omega_0}$.

### *3-2-4 Particle Boundary Conditions*

There are two types of boundary conditions, namely emission and absorption. The emitting boundary condition, is used primarily at the cathode surface of the device and in regions prone to electron emission, such as the collector. Emission from surface of materials depends upon different parameters, such as voltage level and temperature, and this subject is an active area of research.

The second particle boundary condition for simulation is a perfectly absorbing boundary. This boundary condition is often applied to surfaces that are also perfectly

conducting metal boundaries for the field solutions. In this case the particles are eliminated when encounter the boundary and weighting the current produced by these particles is stopped. Although this condition often happens in practice, but the physical validity of this situation is more questionable and often results in difficulties in understanding all the current paths in the simulation [6].

### 3-3 Brief Description of MAGIC

Nowadays, no one can cast any doubts on the importance of modeling and simulation in the research and development aspects of engineering. In most projects, it is impossible or prohibitively expensive to build a device and then test the response in the real world. As a result, before actual manufacture, modeling and simulation of a device, process or system becomes a more convenient, practical, and cost-effective route. Furthermore, modeling allows the simulated testing under different conditions before actual manufacture.

The Particle-in-cell (PIC) based MAGIC software tool has been used in this thesis for simulating the magnetron. One of the objectives is to use the tool for performance predictions which could then lead to the selection of an optimized geometry. This software is a well-established commercially available electromagnetic design tool in the plasma, microwave, and pulsed power communities. MAGIC is a two- and three-dimensional user-configurable numerical simulation code that self-consistently solves the full set of time-dependent Maxwell's equations and the complete Lorentz force equation to provide the interaction between space charges and electromagnetic fields [36]. Three-dimensional finite-difference time-domain (FDTD) electromagnetic algorithms are combined with particle-in-cell (PIC) approaches to provide fast, accurate, time-dependent calculations of

the fields and particle motion in phase-space. The use of different computational and simulation software like MAGIC is necessary since analytical solutions are not usually feasible or even possible for complicated models and geometries.

The accuracy of the simulation results in MAGIC (which is based on the PIC method) is highly dependent on the size and number of the grids or cells. As a general rule, having more cells with finer sizes leads to higher accuracy in the results. However, a simulation with finer grids takes more time and computational costs. Thus, there is a trade-off between accuracy on the one hand, and time and cost. So the size of cells needs to be chosen wisely to have acceptable accuracy in the results while attaining a reasonable running time for simulations. The default configurations of MAGIC provide an acceptable accuracy in reasonable time for the users who does not wish or may not know how to specify some aspects of an electromagnetic PIC simulation [37]. One of the most attractive features of MAGIC is that it allows adaptive meshing for increasing the cell resolution in the area of simulation where the important physics takes place [38].

MAGIC is a successful software in solving equations of motion for particles in electromagnetic fields because it incorporates the most useful techniques and allows for configurations to meet a user's specific needs with minimum effort. Thus, it has been used for simulation and design of various equipment such as microwave amplifiers, sensors, lasers, accelerator components, antennas, for beam propagation, pulsed power systems, field emitter arrays, and semiconductor devices [37].

In the simulations of this thesis with the MAGIC software tool, the magnetron interaction space is divided as follow: 0.5 mm for radial grid resolution, 7.5 mm for axial

grid resolution, and 5 degree for azimuthal grid resolution. There were almost 300,000 active particles present during the simulation to start with, and their number can increase significantly over time during the course of the simulation due to secondary electron emissions.

MAGIC offers different types of emission processes of charged particles from the surfaces of an object. These include: EMISSION EXPLOSIVE, EMISSION HIGH_FIELD, EMISSION PHOTOELECTRIC, EMISSION THERMIONIC, and EMISSION SECONDARY [39].

Explosive emission, (MAGIC command: EMISSION EXPLOSSIVE) is the main type of emission which has been used in simulation of magnetron in this thesis. Explosive emission results from plasma formation on a material surface.

A simple, qualitative explanation for initiation of the explosive emission is that an applied external voltage creates high electric fields (in the $10^7$–$10^8$ V/cm range) at cathode micro-protrusions or “whiskers”. Electrons are then emitted from the surface by processes such as field-emission. The micro-protrusions subsequently blow up due to the high local current density that causes rapid resistive heating, leading to vaporization of the cathode material. Experimental information on possible phase-change at the emitting surface during this process has been observed by means of electron microscopy (for example, in the context of carbon emitters [40]). The vapor is easily ionized, creating a "cathode plasma" that acts as a rich source of electrons [41].

MAGIC largely ignores the physical details of the plasma formation process, relying instead on a phenomenological description. However, the particle emission itself is based

upon Child's law of physics, specifically, the normal electric field vanishing at the plasma surface. In MAGIC calculations, breakdown can occur only if the normally directed field at the half-cell, $E_c$, exceeds the specified breakdown (field threshold) which is defined by the user.

Checking of the electric field with the field threshold is performed continuously for every surface cell on the emitting object. The "break down" occurs at a cell which the field exceeds the field threshold. It should be noted that in MAGIC, a single, non-emitting cell between two emitting cells is also allowed to break down, even if the threshold is not exceeded. The time of breakdown, $t_b$, is recorded for each cell that breaks down. Subsequently, every cell has its own history and is treated independently [39].

The resulting plasma surface is counted as a metal with zero work function. Thus, both ions and electrons can be emitted under the effect of local field. The creation of the macro particle based on Gauss's law is allowed using the phenomenological algorithm until the field of surface reduced to some specified residual value [37]. It can be represented as follows:

$$\frac{dq}{dA} = \varepsilon_0 f(t - t_0)(E_c - E_r) - \rho\, dx, \tag{3.58}$$

where, $f$ is the plasma formation rate which depends on $t_b$, ρ is the existing charge density at the surface, and $E_r$ is the residual field. Restrictions may be imposed to limit the charge of minimum macro particles and maximum current density.

In field emission, (MAGIC command: EMISSION HIGH_FIELD), the electric field supplies the required energy for overcoming the work function. The current density is given by the Fowler-Nordheim equation as follows:

$$\frac{d^2q}{dA\,dt} = \frac{AE_S^2}{\emptyset\, t(y)^2}\exp\left(\frac{-B\, v(y)\, \emptyset^{3/2}}{E_S}\right), \tag{3.59}$$

where $A$ and $B$ are the Fowler-Nordheim constants. The work function, $\emptyset$, and the other functions in the equation may be either a constant or a function of tome and spatial functions [39].

In thermionic emission, thermal (MAGIC command: EMISSION THERMIONIC), thermal energy is required to overcome the work function. In this condition, the current density is given as Equation (3.60).

$$\frac{d^2q}{dA\,dt} = A_0\, T^2\exp\left(\frac{-\emptyset}{KT}\right), \tag{3.60}$$

where, $k$ is the Boltzmann constant and $A_0$ is the Dushman parameter ($= 1.24 \times 10^6 \frac{A}{m^2 Kelvin^2}$). The work function, $\emptyset$, may be either a constant or a function of time and spatial coordinates [39].

For secondary electron emission, (MAGIC command: EMISSION SECONDARY), which has been probed in simulations of this thesis, the incidents electrons provides the required energy for overcoming the potential barrier of the function.

### 3-4 Simulation Model

In order to analyze the effects of endcaps, length of cathode, and location of the cathode with respect to the anode, the A6 MDO geometry of UNM [3] has been chosen as the basic geometry (Figure 2-7) for the present analysis. As was mentioned in Chapter 2, this geometry is the modified design of the well-known A6 magnetron invented by the MIT group [1] with details as explained in Section 2-1.

In order to evaluate the role of endcap on output power, efficiency and leakage current of the A6 MDO magnetron, two types of endcap were designed for magnetron: (a) one comprehensive bulbous shaped endcap, and (b) six individual endcaps.

Different views of A6 MDO magnetron with one bulb-shape endcap and with six individual endcaps, designed by MAGIC 3D, are shown in Figure 3-10 and Figure 3-11, respectively.

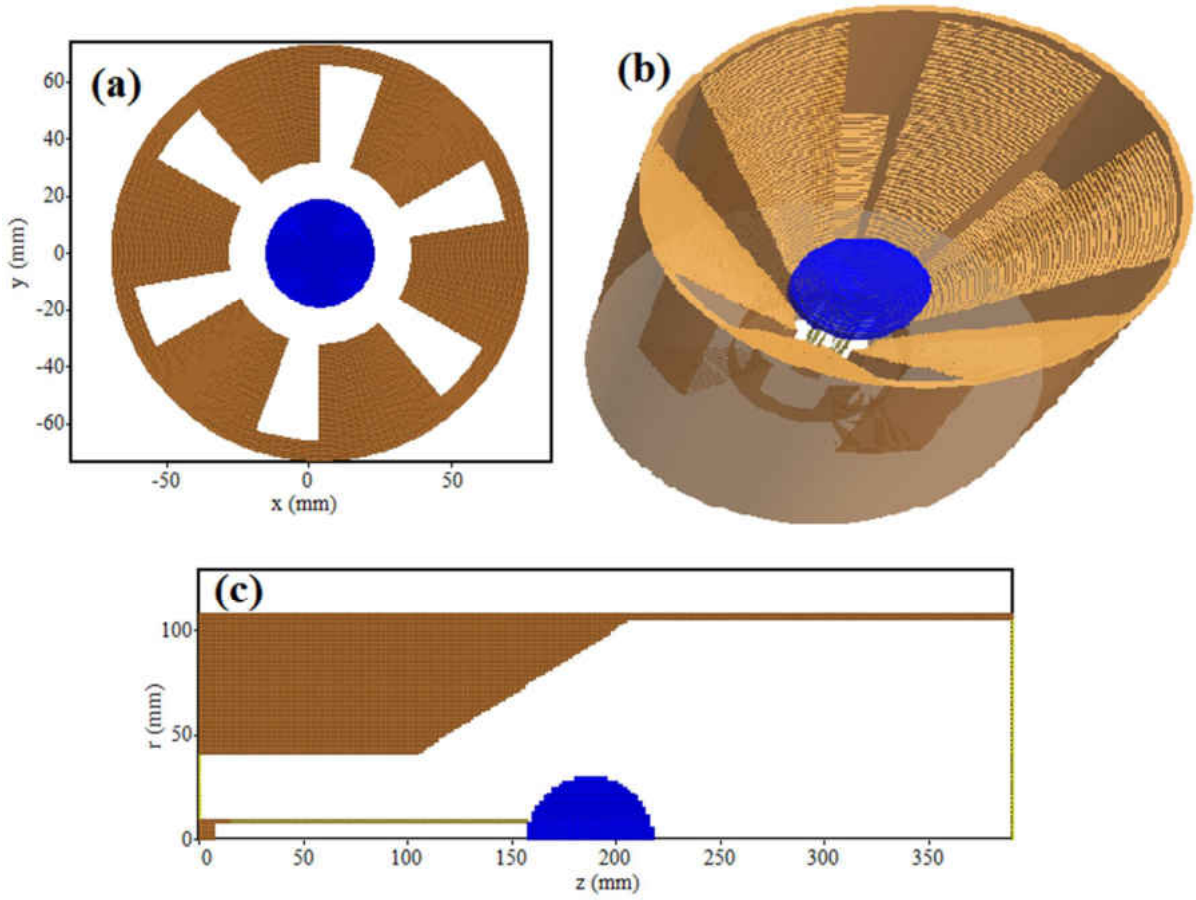


Figure 3-10. A6 MDO magnetron with bulb shape endcap. (a) Cross sectional view in the *r*-$\varphi$ plane. (b) Three dimensional view, (c) Cross sectional view in the *r*-*z* plane.

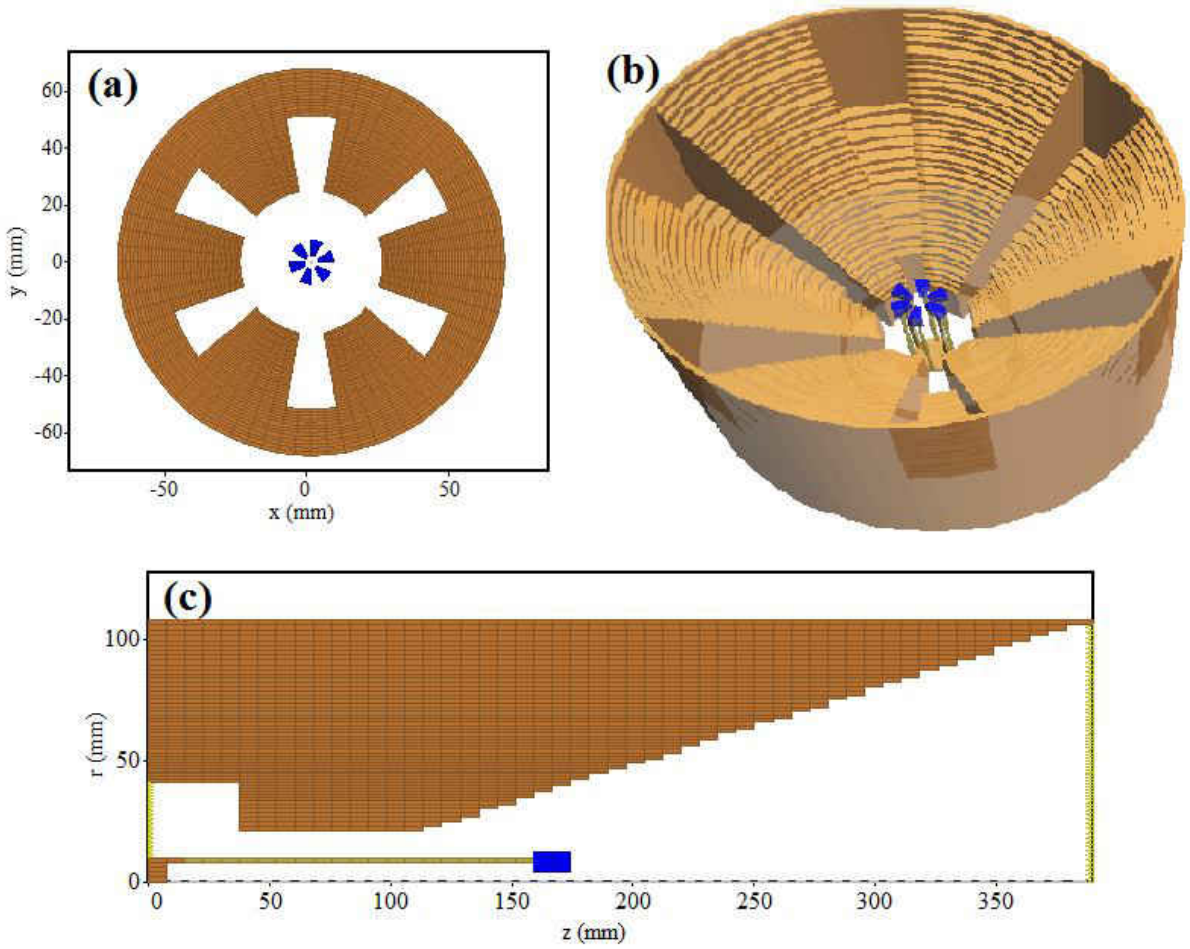


Figure 3-11. A6 MDO magnetron with six individual endcaps. (a) Cross sectional view in the *r*-$\varphi$ plane. (b) Three dimensional view, (c) Cross sectional view in the *r*-*z* plane.

In addition, in order to evaluate and find the optimized geometry and operation conditions of a Rising-Sun magnetron with axial output, again the well-known A6 magnetron [1] was chosen as the basic configuration to start building with, though appropriate changes relating to the anode block and cathodes were implemented for the Rising-Sun geometry. The anode block consisted of 12 sectorial 20˚ cavities with length $L$ = 7.5 cm, maximum radius $R_{cav}$ = 4.11 cm, and minimum radius $R_a$ = 2.11 cm [3, 42-44].

Two different structures were used for the short vanes of the Rising-Sun magnetron. As shown in Figure 3-12, for the first geometry, the outer radii of vanes were fixed and the

slope of vanes ($\beta$) was changed. In the second geometry (Figure. 3-13), the radius of the vanes ($R_s$) was changed while the distances to the point of the vane endings were fixed at 204.6 mm for all six vanes. Thus, both models had the basic tapered structure that has been proposed and studied previously [45]. This differs slightly from the configuration used in a very recent report on 12-cavity relativistic magnetrons [46], wherein the tapered cavity was replaced by a single-stepped cavity. However, the single-stepped design does have some drawbacks, and so was not considered in this thesis. For example, one cannot have mode conversion as readily as with a tapered MDO. In addition, one would require larger diameter Helmholtz coils for the single-stepped cavity in order to provide the uniform magnetic field in the interaction space.

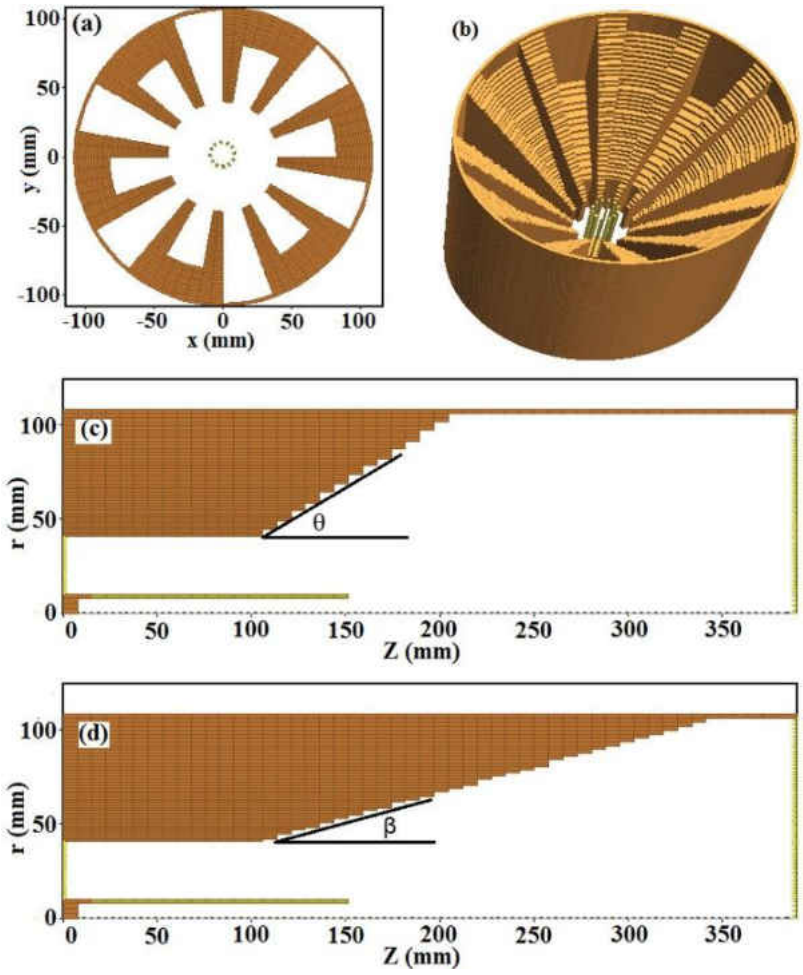


Figure 3-12. Rising-Sun magnetron with the anode block geometry chosen as the first configuration for quantitative performance evaluation with variable angle for short vanes (angle $\beta$). (a) Cross sectional view in the *r*-$\varphi$ plane. (b) Three dimensional view for $\beta$ equal to 15 degrees. (c) Cross sectional view of the long vanes in the *r*-*z* plane. (d) Cross sectional view of the short vanes in the *r*-*z* plane [47].

The transparent cathode structure for the simulations was modeled as consisting of 12 discrete longitudinal emitters evenly placed at 8 millimeter from the center ($R_c$ = 8 mm) with 2 mm and a 10-degree thickness.

For the MDO, the coaxial antenna for extracting the generated microwave power was modeled to consist of an antenna feed and head without a dielectric vacuum window to

maintain vacuum inside the magnetron. The model here included an input port at the lowest $z$-position for providing dc power to the magnetron, and an output port at the highest $z$-position for absorbing the microwave power incident on it.

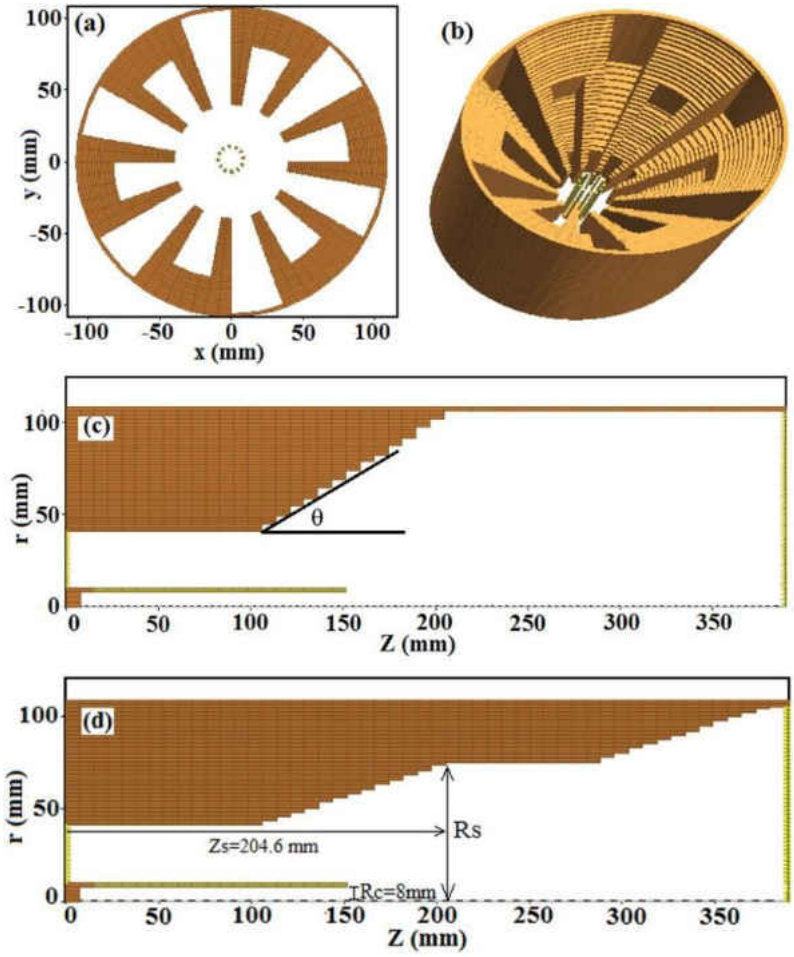


Figure 3-13. The second anode block geometry chosen for the Rising-Sun magnetron simulations with variable outer radius for short vanes ($R_s$). (a) Cross sectional view in the r-φ plane. (b) Three dimensional view for $R_s$ equal to 75 mm. (c) Cross sectional view of the long vanes in the r-z plane. (d) Cross sectional view of the short vanes in the r-z plane [47].

In addition, two different shapes of the endcap were used in the simulations of Rising-Sun magnetron: a bulb shape and cylindrical shape. The radius of endcap for both cases was taken to be 25 mm with the thickness of the cylindrical endcap set at 15 mm. The geometry for these two comprehensive endcaps used is shown in Figure 3-14.

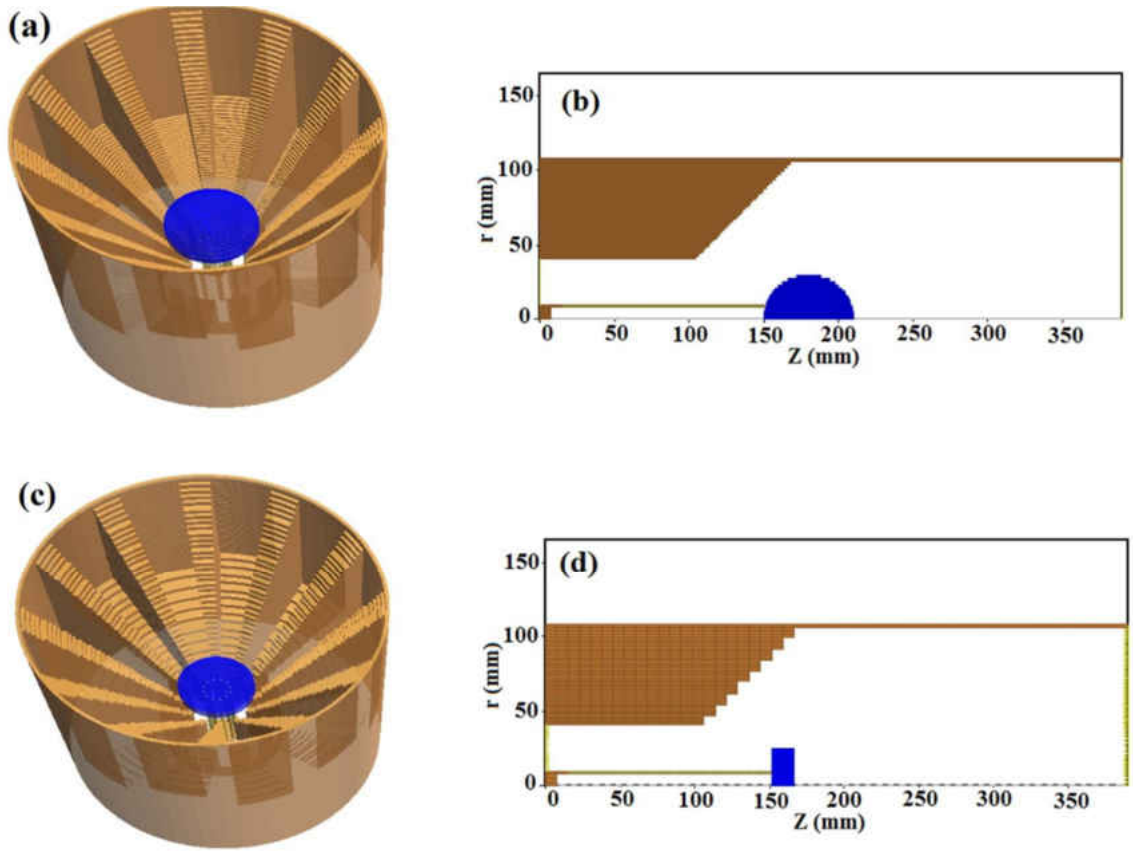


Figure 3-14. Geometry used for Rising-Sun MDO structures with different endcap geometries. (a) Three dimensional view with Bulb shape endcap, (b) Cross sectional view in the *r-z* plane with Bulb shape endcap, (c) Three dimensional view with cylindrical endcap, (b) Cross sectional view in the *r-z* plane with cylindrical endcap [47].

# CHAPTER 4

# RESULTS AND DISCUSSION

For the PIC simulations, 50-ns voltage pulses of magnitude 400 kV with a 4-ns rise-time were applied. Integrating the angular electric field across each cavity yielded the radiofrequency (RF) voltages. The frequency was obtained through a Fourier transform of an RF-voltage over a time interval in the steady state domain. The simulation time step, on which the time-integration scheme is based, is automatically chosen to meet the Courant-Friedrichs-Lewy [48] stability condition of: $\delta t < \delta x/(c\sqrt{2})$, where $\delta x$ is the smallest cell size and $c$ is the speed of light.

## 4-1 Simulation Results and Discussion

### *4-1-1 A6 MDO Magnetron*

The role of the cathode length and its extension beyond the anode dimensions was initially probed. The length of the anode block $L$ was 7.2 cm, and different cases were simulated for cathode lengths of $L$, $L+2dz$, $L+4dz$, where $dz$ = 7.5 mm. PIC simulation results for the A6 MDO without any endcap for these three different lengths of the cathode are shown in Figure 4-1. The output power, device efficiency and leakage current were obtained as a function of the applied magnetic field. In all cases, the maximum efficiency occurs at a B-value of about 0.42T and is roughly 43%. As shown in Figure 4-1(a), the leakage current is predicted to fall monotonically from about 2.65 kA to 1.8 kA in going from 0.3T to 0.44 T in 7.5 cm cathode length.

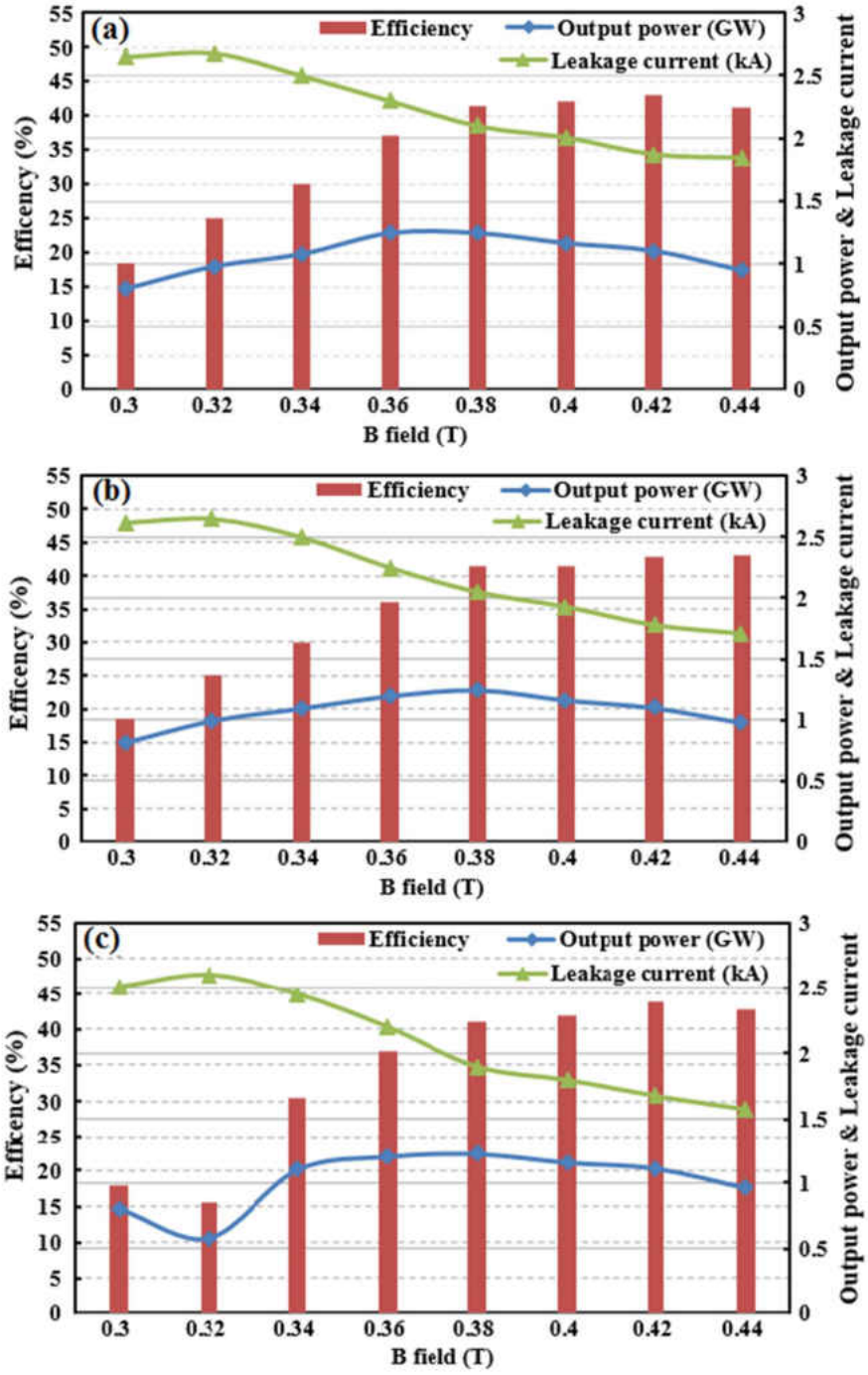


Figure 4-1. PIC simulation results for the A6 MDO without any endcap. The output power, device efficiency and leakage current are shown as a function of the applied magnetic field for different cathode lengths: (a) Cathode length 7.5 cm (*L*), (b) cathode length 9 cm (*L +2dz=7.5+1.5 cm),* and (c) cathode length 10.5 cm (*L +4dz=7.5+3 cm).*

In regards to the increase in cathode length, a comparison of Figure 4-1(a) and Figure 4-1(c) shows a slight decrease in leakage currents from about 1.8 kA down to 1.55 kA at the 0.44 T field. The maximum output power is predicted to about 1 GW at the highest 0.44 T field in both cases.

Next, PIC simulations for the MDO with one comprehensive endcap encompassing all six cathodes were carried out for four different lengths of the cathode. The geometry for the comprehensive endcap is shown in Figure 3-10. Once again, the output power, device efficiency and leakage currents were obtained as a function of the applied magnetic field for cathode lengths of *L-2dz, L, L+2dz*, and *L+4 dz*, as shown in Figure 4-2.

The increases in efficiency as compared to the previous results of Figure 4-1 are quite significant. For instance comparing Figure 4-1(c) with Figure 4-2(b) for a cathode length *L+4dz*, shows the efficiency to increase from about 43% at a 0.42 T field without an endcap, to 62% at the same 0.42T field with an endcap. Figure 4-2(b) shows the efficiency values for a slightly longer cathode with an endcap is again slightly large. It is thus apparent that though a shorter cathode length is detrimental to the performance, the endcap plays a stronger role. Even more important and significant is the sharp drop-off in leakage current with the presence of an endcap. The leakage current is close to zero in Figure 4-2(c) at the higher magnetic fields of 0.42 T, as compared to 1.8 kA in Figure 4-1.

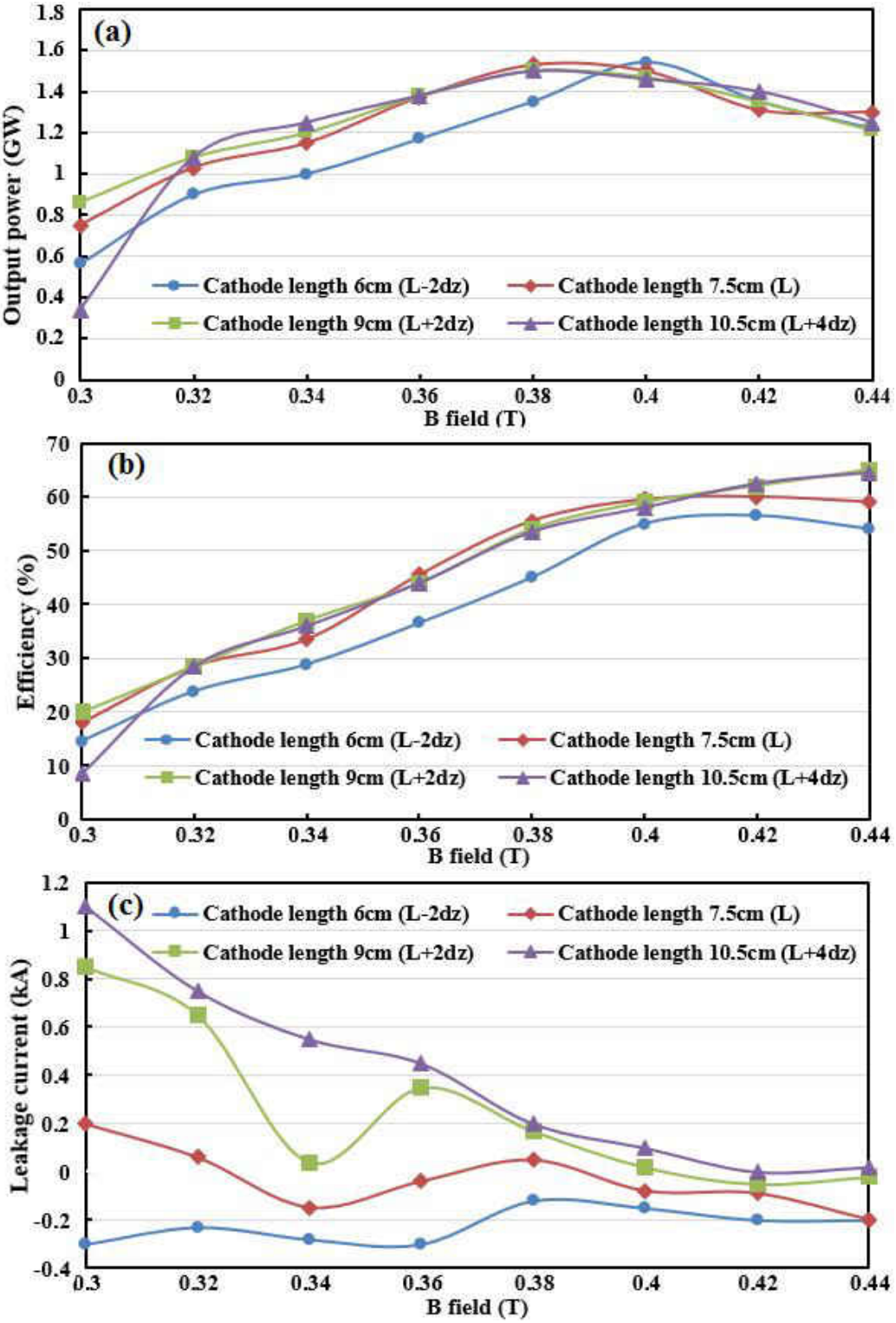


Figure 4-2. PIC simulation results for the A6 MDO with one comprehensive endcap for different length of cathodes. (a) The output power, as a function of the applied magnetic field. (b) Efficiency, as a function of the applied magnetic field, and (c) Leakage current, as a function of the applied magnetic field.

Finally, the output power is also predicted to increase with the use of endcaps for all four cathode lengths as shown in Figure 4-2(a). At the magnetic fields of 0.4T, the output power is predicted to be on the order of 1.5 GW. Based on Figure 4-2, one would select operating magnetic fields in the 0.4-0.44 range with the endcap and a cathode that extends beyond the anode dimension for superior performance.

In addition, MAGIC-based simulations were also carried out for the same MDO structure, but with six individual endcaps for the six electrodes. The geometry for this configuration is shown in Figure 3-11. Results of MAGIC simulation for the MDO with the six individual endcaps are shown once again as a function of the applied magnetic field in Figure 4-3. These plots show the output power, device efficiency and leakage current for cathode lengths of *L-2dz, L, L+2dz*, and *L+4 dz*. The results are somewhat similar to the plots of Figure 4-2 obtained for a single endcap.

As Figures 4-3(a) and 4-3(c) shows the peak output power at the highest B-fields of 0.44T is predicted to be somewhat lower at about 1.08 GW, though the leakage currents at the same fields are close to zero for cathode length 9 cm and 10.5 cm. The efficiencies continue to be quite high, and are just over 62%. The results show although the B-field 0.44T gives the highest efficiency but the output power at 0.44T dropped to about 1 GW from 1.4 GW at B-field around 0.4T. Thus, for this 6-endcap configuration, the results suggest an optimum operating range for the B-field around 0.4T. Therefore, based on the results of Figures 4-2 and 4-3, the best choice taking account of the highest efficiency, output power, and lowest leakage current, would appear to be an extended cathode with length $L$ + 2 dz and an operating B-field of 0.4 T.

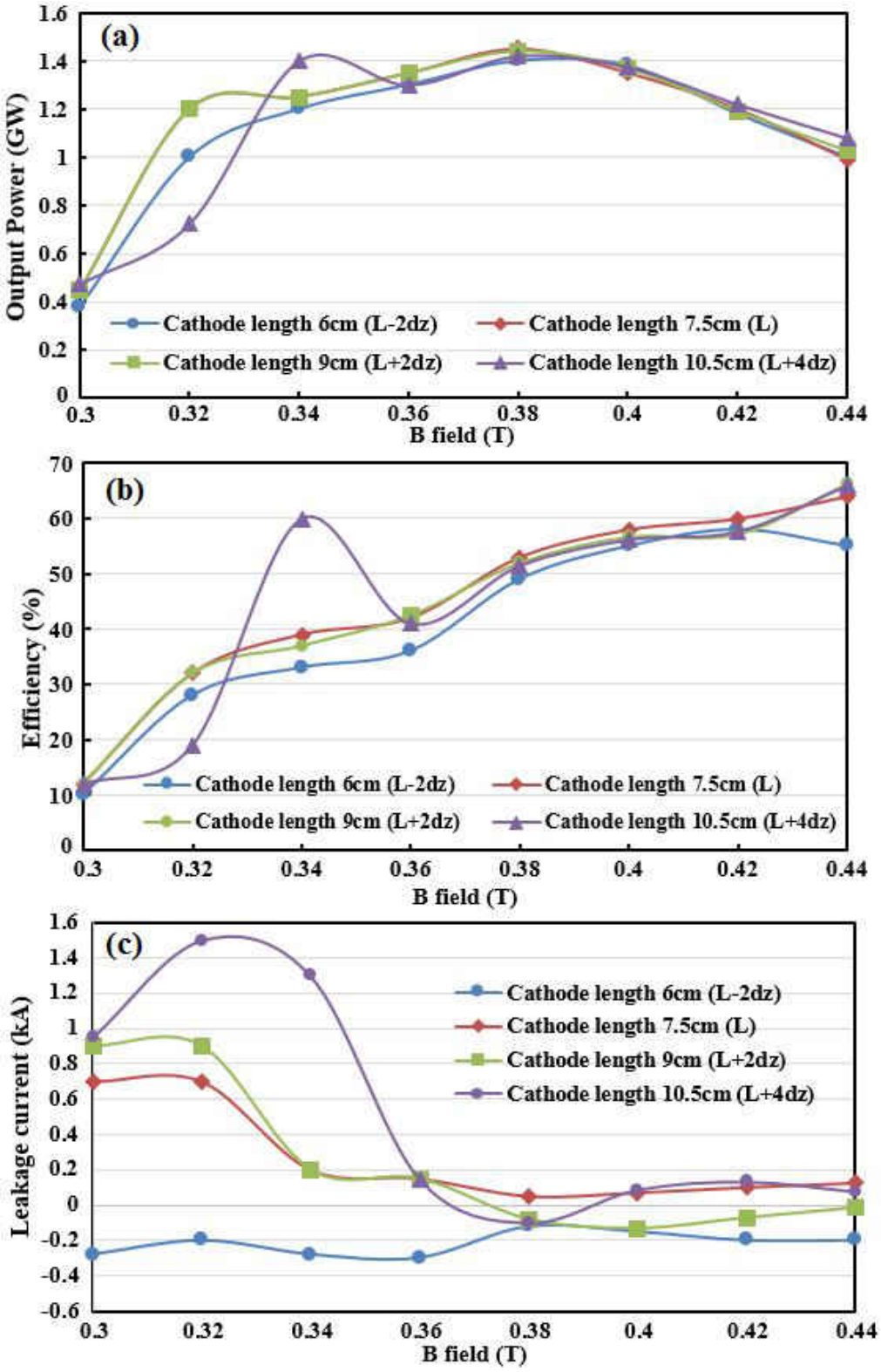


Figure 4-3. PIC simulation results for the A6 MDO with six individual endcaps for different length of cathodes. (a) The output power, as a function of the applied magnetic field. (b) Efficiency, as a function of the applied magnetic field, and (c) Leakage current, as a function of the applied magnetic field.

Based on these parameters for having the optimized geometry and magnetic field, further simulation work was carried out to probe the potential location and thus angular offset between the transparent cathodes relative to the six-anode structure. Figure 4-4 shows the angle between x-axis and the first cathode which has been changed from zero to 60 degree for analyzing the effect of location of cathodes with respect to anode block.

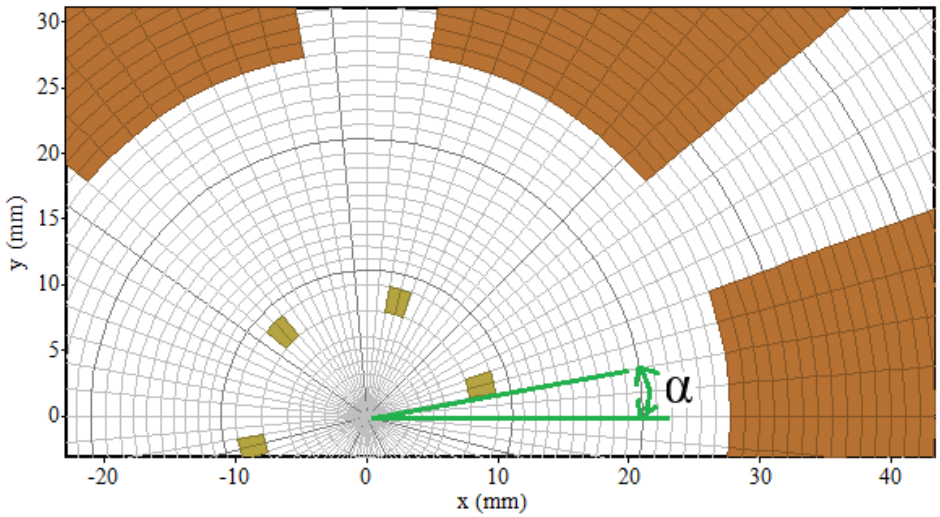


Figure 4-4. Angle between x-axis and first cathode (alpha).

Both the output power and leakage currents are shown as a function of "$\alpha$" in Figure 4-5. As this figure shows the magnetron has the lowest leakage current magnitude and highest output power at $\alpha$~55 degree. Thus, the optimized value of the output power is predicted to be about 1.47 GW for the 400 kV, 4 ns rise-time voltage. The leakage current is small at about 25 Amperes and the overall efficiency of this MDO with a cathode extension of 3 cm was obtained at about 66 %.

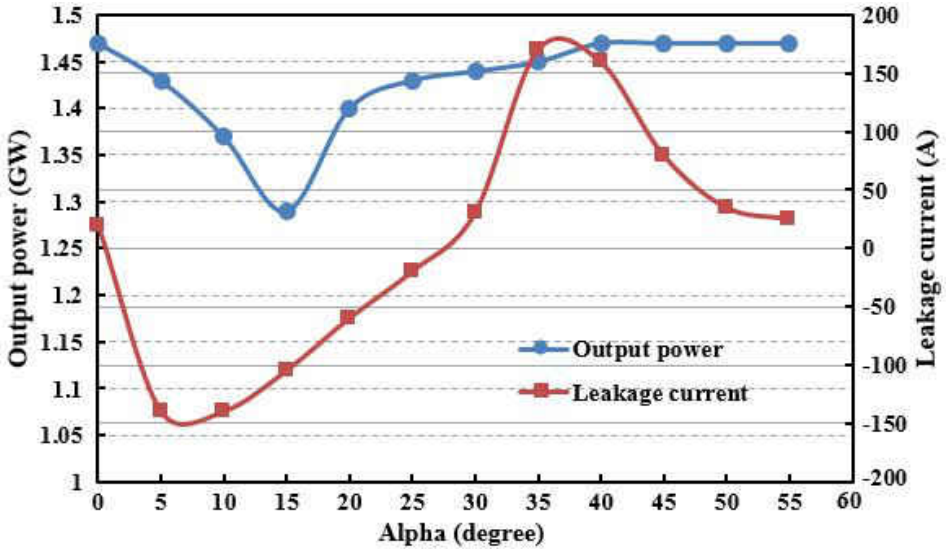


Figure 4-5. Simulation results for the output power and leakage current as a function of angular location of the cathode with respect to the anode block. One comprehensive endcap and an extended cathode of length *L+2dz* was used with a fixed B-field of 0.4 T.

### *4-1-2 Rising-Sun Magnetron*

Finding the optimized geometry for anode block of Rising-Sun magnetron was the first step in the overall process of conducting numerical simulations on Rising-Sun geometry. The cut-away views of the Rising-Sun geometry are shown in Figures 3-12 and 3-13. The anode is a Rising-Sun block comprised of six long and six short vanes. In the first geometric configuration for the anode block, the slope of the short vanes (angle $\beta$ in Figure 3-12(d)) was changed from 5 degree to 60 degree in 5 degree increments, while the angle of other six vanes (angle θ in Figure 3-12(c)) was kept fixed at 32 degrees. This fixed value represents an optimized angle as obtained in previous simulations [3, 42]. In the second anode block geometry shown in Figure 3-13, $R_s$ was changed from 55 mm to 100 mm in 5mm steps, while $Z_s$ was kept fixed at 204.6 mm for all six short vanes. It should be noted that the outer radius for the six long vanes was 105 mm at a constant angle of θ=32 degrees. Three dimensional views of these two geometries (Figures 3-12(b) and 3-13(b)) give a

better perception of the geometries. Particle-in-cell simulation results for the 12 cavities, 12 cathodes Rising-Sun MDO without any endcap for these two different geometries of the anode block are shown in Figures 4-6 and 4-7. The simulations were carried out at two different applied magnetic fields of 0.42 T and 0.48 T. The output power, device efficiency and leakage current were obtained for different values of $\beta$ as shown in Figures 4-6(a) and 4-6(b), and for various $R_s$ values as in Figures 4-7(a) and 4-7(b).

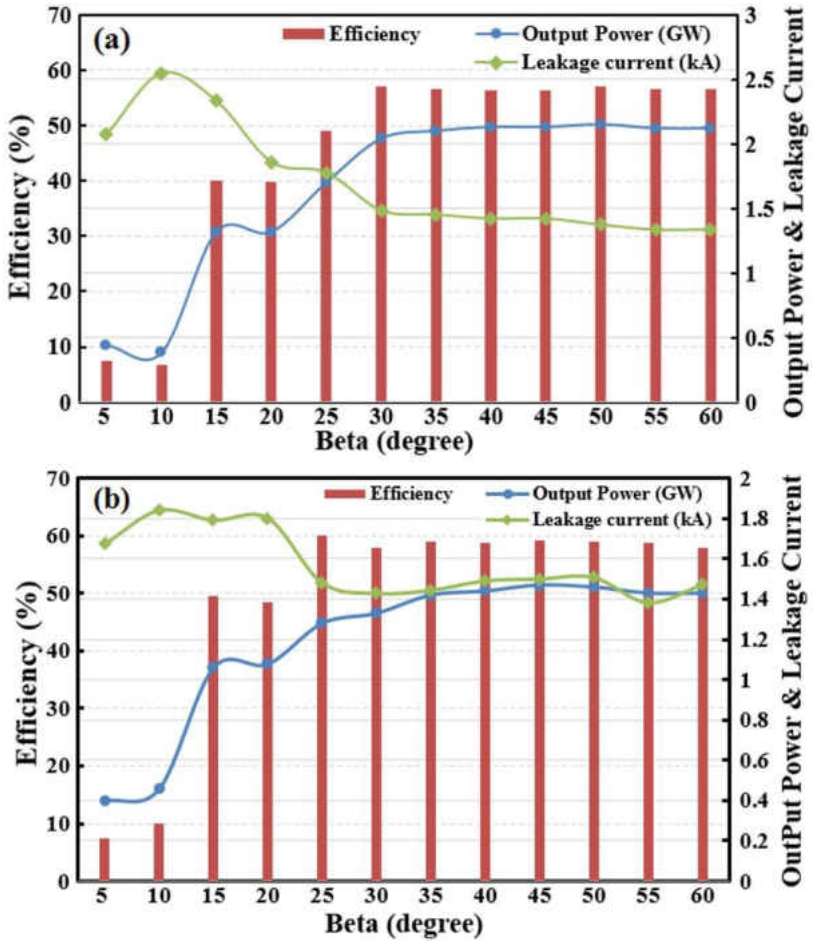


Figure 4-6. PIC simulation results for the 12-Cavity Rising-Sun Magnetron. The output power, device efficiency and leakage current are shown as a function of short vanes angle ($\beta$). Applied magnetic fields of: (a) B = 0.42 T, and (b) B = 0.48 T were used [47].

Figures 4-6(a) and 4-6(b) show the output power, device efficiency and leakage current for different angles of the short vanes for applied magnetic fields of 0.42 T and 0.48 T, respectively. Figures 4-7(a) and 4-7(b) show the output power, device efficiency and leakage current for different values of $R_s$ (corresponding to the anode geometry of Figure 3-13) for same two values of the applied magnetic fields. Comparing Figures 4-6 with Figures 4-7 shows that the first geometry (i.e., changing angle $\beta$) appears to have a better performance as compared to changing $R_s$ within the second geometry.

The magnetron with the geometry of Figure 3-12 is predicted to work at an efficiency of about 57% at 0.42 T, and an efficiency of about 59% at 0.48 T. On the other hand, the second geometry (Figure 3-13) at best is predicted to work at efficiencies of about 50% and 54% for magnetic fields of 0.42 T and 0.48 T, respectively.

In addition, the output power in the first geometry is higher than that of the second geometry. For example, the first structure has a maximum output power of about 2.1 GW at 0.42 T and 1.45 GW at 0.48 T, while the second geometry has maximum output powers of about 1.7 GW and 1.2 GW at 0.42 T and 0.48 T, respectively. Clearly then, the geometry of Figure 3-12 is preferable from the standpoint of better performance and was therefore chosen for further analysis.

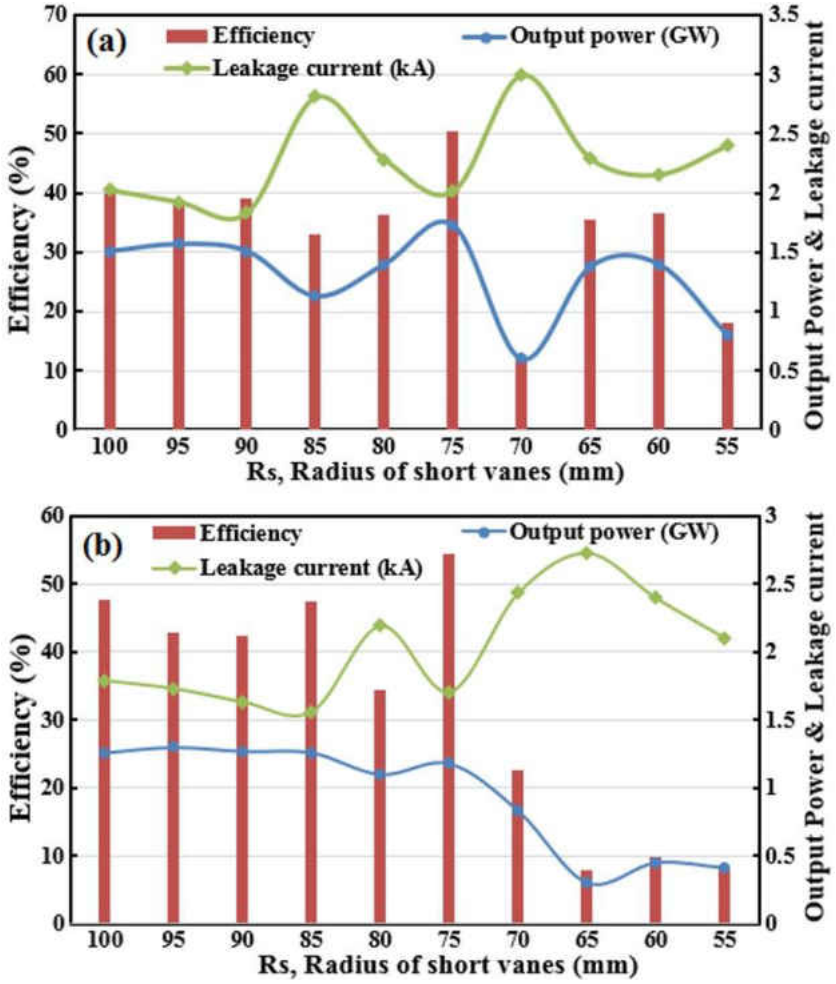


Figure 4-7. PIC simulation results for the 12-Cavity Rising-Sun magnetron. The output power, device efficiency and leakage current are shown as a function of the parameter $R_s$. As with figure 3-13, applied magnetic fields of: (a) B = 0.42 T, and (b) B = 0.48 T were used [47].

After choosing the geometry for the Rising-Sun MDO, a selection for the best slope (angle $\beta$) was made based on the simulation results already obtained. Simulation data of Figure 4-6 suggest an optimum operating range for $\beta$ between 40 and 50 degrees from the standpoint of efficiency and output power. In this range of angles, a 57% efficiency and a 2.1 GW output power, as well as a 59% efficiency and a 1.4GW output power were obtained at magnetic fields of 0.42 T and 0.48 T, respectively. Therefore, $\beta$ = 45 degrees

was chosen as the optimized angle for the short vanes of the Rising-Sun MDO, with a 56.4% efficiency and 2.13 GW output power at 0.42 T, and a 59.1% efficiency with a 1.47 GW output power for the 0.48 T field. It may be noted that at this chosen angle, the device has relatively low leakage current compared to the other angles at both simulated magnetic field values.

Next, PIC simulations for the Rising-Sun MDO with one comprehensive endcap encompassing all twelve cathodes were carried out for different values of the applied magnetic field. Two different shapes of the endcap were used in the simulations: a bulb shape and cylindrical shape. The geometry for these two comprehensive endcaps used is shown in Figure 3-14. It should be mentioned that these two types of endcaps were added to optimized geometry (including the $\beta = 45$ degrees angle) obtained in the previous steps.

The output power, device efficiency and leakage currents were obtained once again with the endcaps as a function of the applied magnetic field. Figure 4-8 shows the results. The increase in efficiency in Figure 4-8 is quite significant as compared to the previous results of Figure 4-6. For instance, comparing the results of Figure 4-6 for a $\beta$ value of 45-degree with Figure 4-8 at a 0.42 T magnetic field, shows the efficiency increasing from about 56% without an endcap, to about 65% and 66% with a bulb shaped and cylindrical endcap, respectively. The results at a different magnetic field of 0.48 T also verified this rising trend in efficiency. At 0.48 T, the efficiency is predicted to increase from 59% for an MDO without an endcap, to about 69% with either a bulb shaped or cylindrical endcaps.

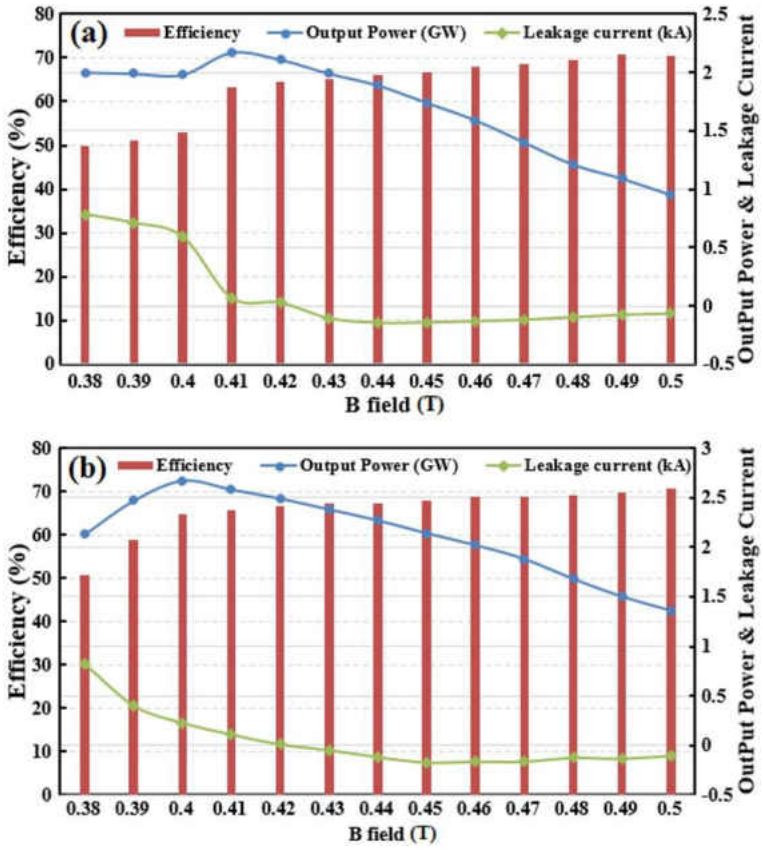


Figure 4-8. PIC simulation results for the 12-Cavity Rising-Sun magnetron with endcap. The output power, device efficiency and leakage current are shown as a function of the applied magnetic field for: (a) a bulb shape endcap, and (b) a cylindrical endcap [47].

In addition to efficiency increases, the sharp drop-off in leakage current with the presence of an endcap is another important benefit of adding endcaps. Figure 4-9 compares the leakage current for three different conditions: without any endcap, with a bulb-shaped cap, and with a cylindrical cap. This figure shows that the leakage current to have decreased significantly upon adding endcaps for the cathodes. Specifically, the leakage current values dropped from about 1.5 kA to less than 200 A for magnetic field higher than 0.4T. Besides, the values were quite close to zero at operating magnetic fields in the 0.41 T to 0.43 T range. Therefore, based on the simulation results of Figures 4-8 and 4-9, one might

select the cylindrical endcap at an operating magnetic field 0.43 T as the optimized geometry and operating condition for enhanced efficiency and output power, coupled with low leakage currents.

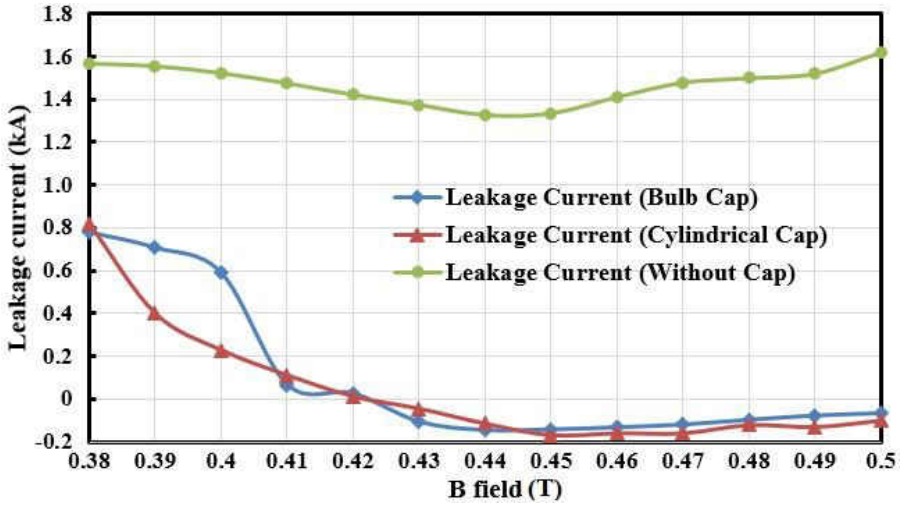


Figure 4-9. Leakage current of 12-Cavity Rising-Sun Magnetron for three different cathode structures. These structures were without any endcap, with a bulb-shaped cap, and with a cylindrical endcap [47].

The role of the cathode length and its extension beyond the anode dimensions was probed next. The length of the anode block $L$ was 7.2 centimeters, and different cases were simulated for cathode lengths ranging in the interval: 12 cm < $L$ < 19.5 cm. The simulations were carried out at incremental steps $dz$ of 7.5 mm. PIC simulation results for the 12-Cavity Rising-Sun MDO with a cylindrical endcap for different lengths of the cathode are shown in Figure 4-10. The magnetic field was taken to be 0.43 T. The output power, device efficiency and leakage current were obtained as a function of cathode length. From the standpoint of high efficiency and output power, coupled with low leakage currents, a

cathode length of *L+5dz* appears to be a good optimal choice based on the simulation results of Figure 4-10.

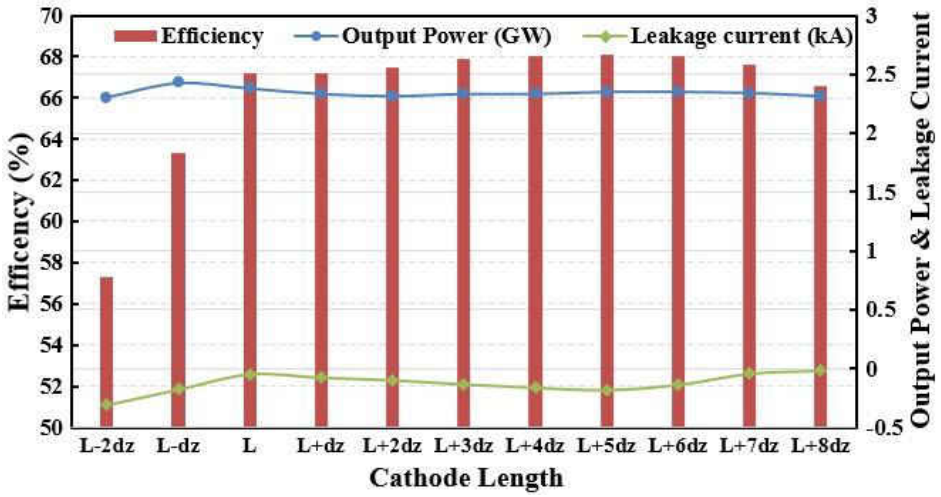


Figure 4-10. PIC simulation results for the 12-Cavity Rising-Sun MDO with a cylindrical endcap for different lengths of the cathode at an applied magnetic field 0.43 T. The output power, device efficiency and leakage current are shown as a function of cathode length [47].

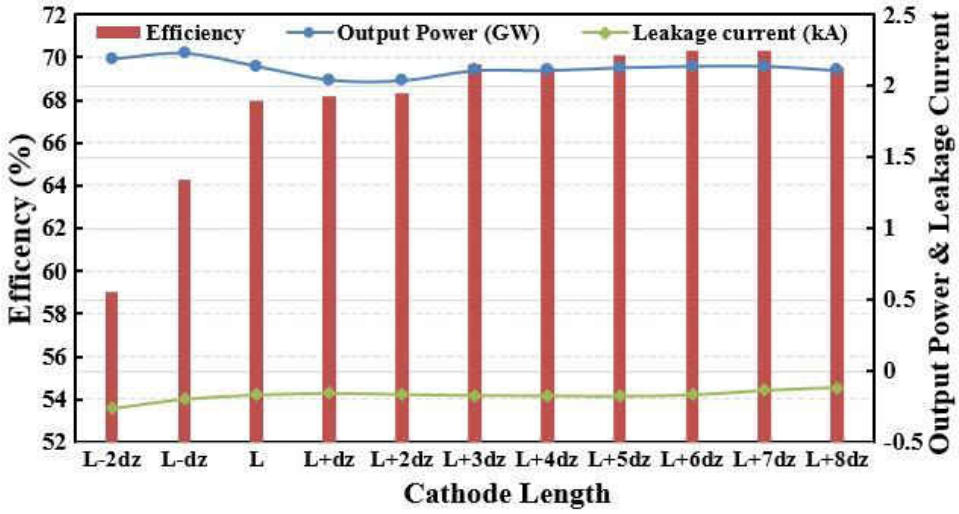


Figure 4-11. Simulation results for the 12-Cavity Rising-Sun Magnetron with cylindrical endcap for different lengths of the cathode at magnetic field 0.45T. The output power, device efficiency and leakage current are shown as a function of cathode length [47].

PIC simulations were also carried out for different cathode lengths at a slightly higher magnetic field of 0.45 T with the cylindrical endcap. This second set of simulations at a slightly higher magnetic field of 0.45 T were carried out based on the results already obtained in Figure 4-8. Though the device output power was slightly lower (2.15 GW at the 0.45 T magnetic field), but a slightly higher 68% efficiency was predicted at this magnetic field. The PIC simulation results as a function of cathode length at 0.45 T are given Figure 4-11. The results of Figure 4-11 are somewhat similar to the curves at 0.43T in Figure 4-10. The results show the efficiency to have been raised slightly with increasing cathode length. It is seen to slightly surpass 70% efficiency for the interval: 17.25cm < $L$ < 18.75cm at 0.45 T. Thus, taking into consideration both figures 4-10 and 4-11, the best choice in terms of the highest efficiency and output power, with the lowest leakage current would appear to be an extended cathode with a length of 18 cm (=$L$+6dz) and an operating magnetic-field of 0.43 T or 0.45 T. At 0.43 T, the device operates with a 68% efficiency and 2.35 GW output power, while the MDO works at a 70.5% efficiency and 2.14 GW output power at 0.45 T. It may additionally be mentioned that the leakage current in both these cases is at about 150 A which is significantly lower than without any endcaps. In the former case, leakage currents as high as 1.5 kA were calculated.

Furthermore, Figures 4-12 and 4-13 depict the MAGIC-based PIC simulation results for the temporal evolution of various quantities of interest within the 12-Cavity Rising-Sun magnetron. A cylindrical endcap and 18 cm cathodes (=$L$+$6dz$) at a 0.45 T applied magnetic field was used. The efficiency is seen to reach 70% within about 20 ns. The output power is predicted to be about 2.36 GW with a current of ~8.4 kA.

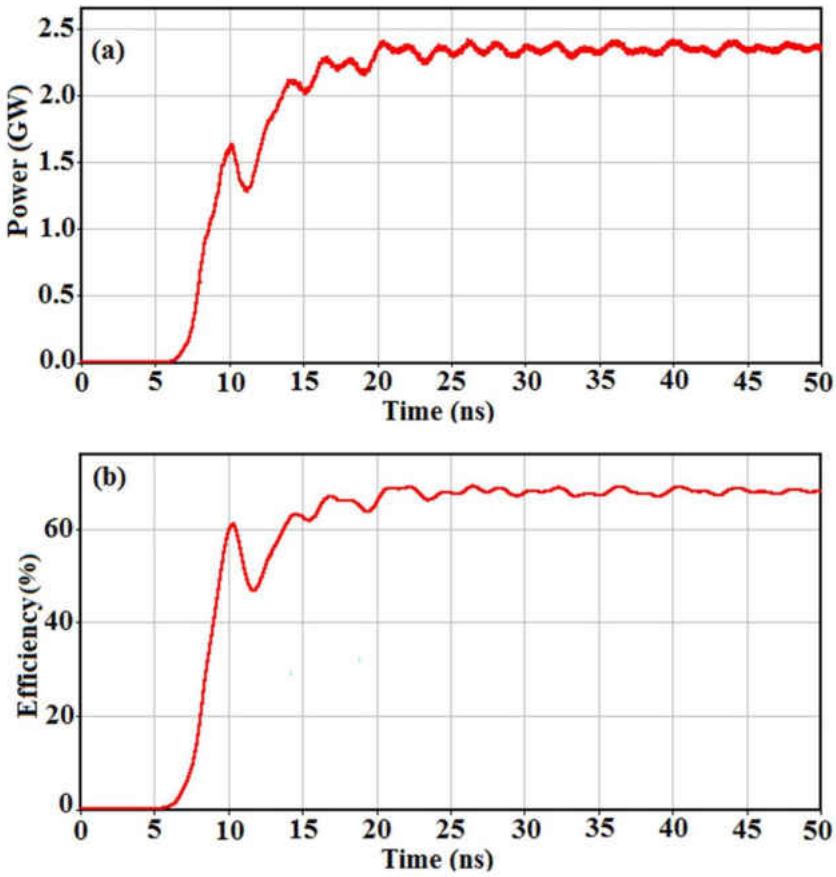


Figure 4-12. MAGIC-based simulation results for the 12-Cavity Rising-Sun Magnetron with a cylindrical endcap and 18cm cathodes (L+6dz) at a 0.45 T magnetic field. The figures show: (a) Output power, and (b) Efficiency [47].

Moreover, snapshots of the electron distributions within the cross sectional structure of the magnetron without and with a cylindrical endcap at three different time instants of 4.99 ns, 20.038 ns, and 39.442 ns for a 0.45T magnetic field are shown in Figures 4-14 and 4-15 respectively. Comparison of the figures, with and without an endcap, demonstrates the role of the endcap in suppressing electrons leakage current and contributing to higher efficiency. For instance, Figures 4-14(d) till 4-14(f) and Figures 4-15(g) till 4-15(i) represent snapshots at exactly the same position and time of MDO with and without endcap, respectively.

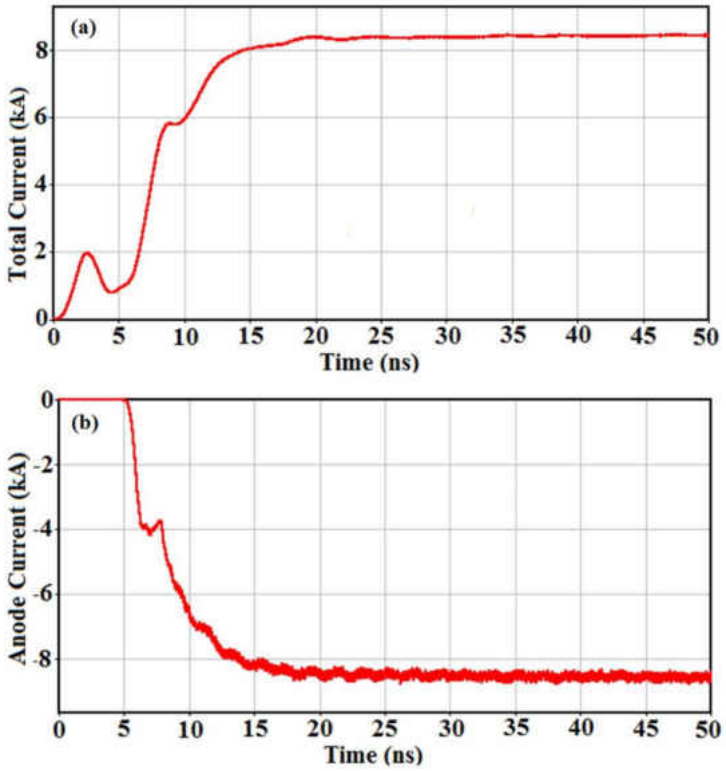


Figure 4-13. MAGIC-based simulation results for the 12-Cavity Rising-Sun Magnetron with a cylindrical endcap and 18cm cathodes (L+6dz) at a 0.45 T magnetic field. (a) Total current, and (b) Anode current [47].

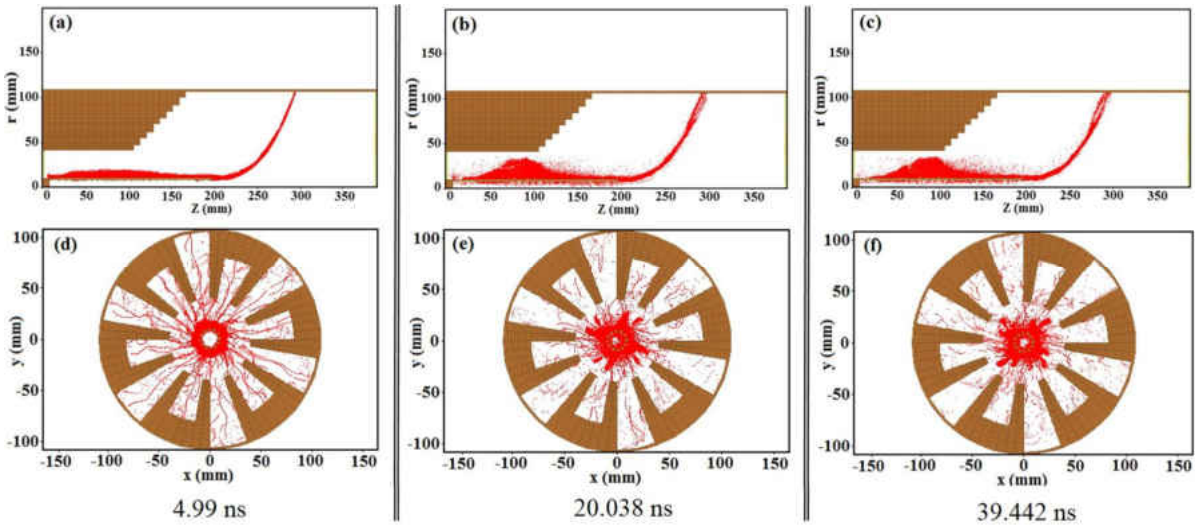


Figure 4-14. Snapshots at 4.99 ns, 20.038 ns, and 39.442 ns showing the evolution of the electron swarm and formation of spokes in the 12-Cavity 12-cathode Rising-Sun Magnetron without endcap at 0.45 T magnetic field and 400kV applied voltage. The various figure are the r-z plane cross sectional view of magnetron without any endcap at: (a) 4.99 ns, (b) 20.038 ns, and (c) 39.442 ns. The r-φ plane cross sectional view of the MDO at z=17.04cm, at: (d) 4.99 ns, (e) 20.038 ns, and (f) 39.442 ns [47].

Most of the electron flux is blocked by the endcap and is predicted not to reach the vanes and output window. It should be noted that Figures 4-15(g), 4-15(h), and 4-15(i) are cathodes with endcap, but this intersection (at $z$ = 17.04cm) is below the endcap, and hence the endcap cannot be seen in the figure.

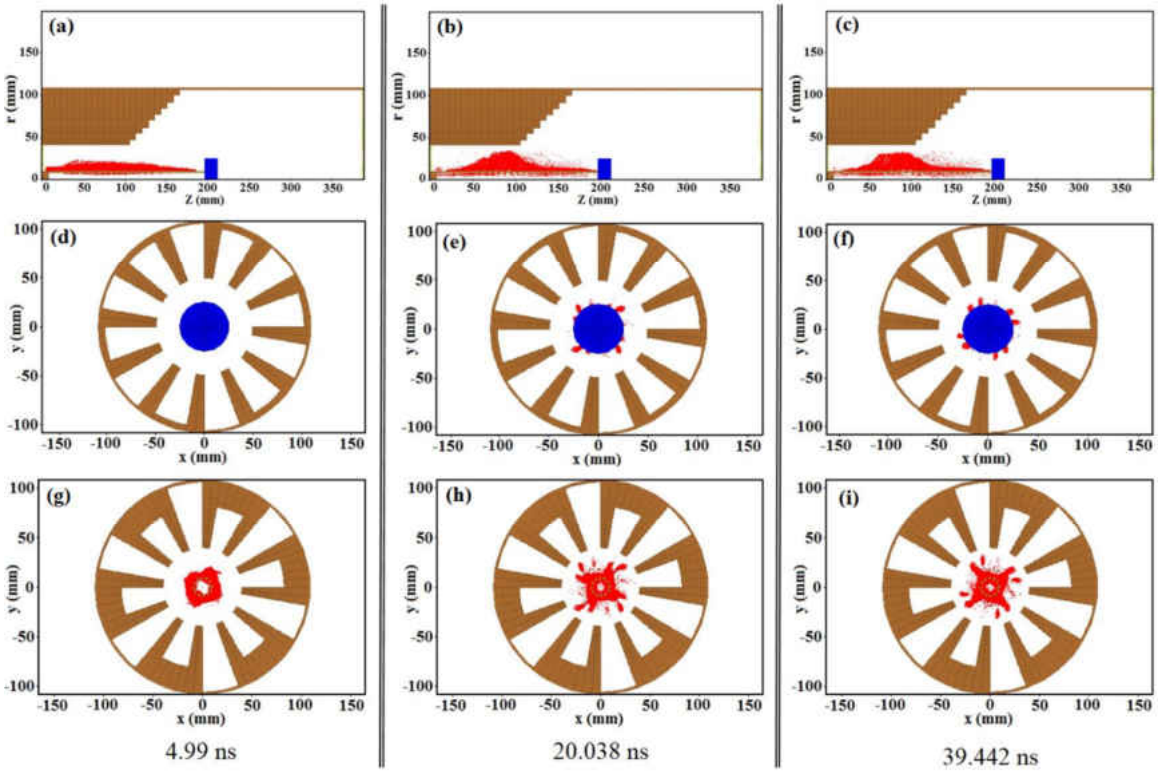


Figure 4-15. Snapshots at 4.99 ns, 20.038 ns, and 39.442 ns showing the evolution of the electron swarm and formation of spokes in the 12-Cavity 12-cathode Rising-Sun Magnetron with a cylindrical endcap at 0.45 T magnetic field and 400kV applied voltage. The various figures are the MDO cross sectional view in the $r$-$z$ plane at: (a) 4.99 ns, (b) 20.038 ns, and (c) 39.442 ns. Cross-sectional snapshots in the $r$-$\varphi$ plane of magnetron at $z$ = 20.08cm at: (d) 4.99 ns, (e) 20.038 ns, and (f) 39.442 ns. Finally, snapshots in the $r$-$\varphi$ plane of the magnetron at $z$ = 17.04cm, at: (g) 4.99 ns, (h) 20.038 ns, and (i) 39.442 ns, respectively [47].

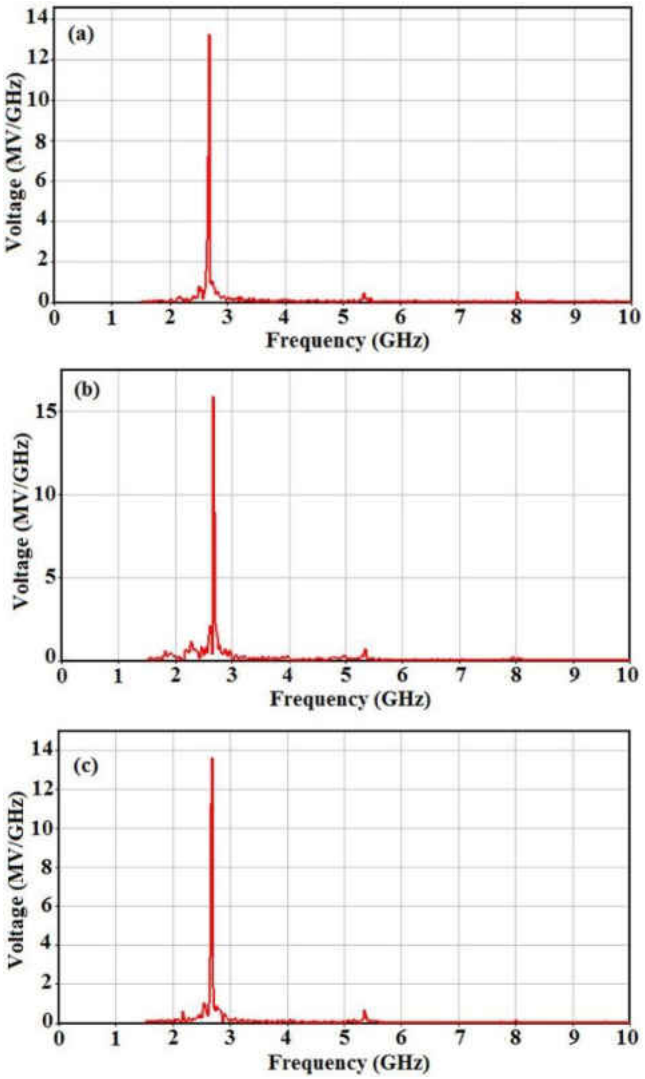


Figure 4-16. Output voltage spectra for the 12-Cavity Rising-Sun Magnetron at an applied magnetic field 0.45 T for various cases. (a)Without endcap and 13.5 cm cathodes, (b) with a cylindrical endcap and 13.5 cm cathodes, and (c) with a cylindrical endcap and 18 cm (= L+6dz) cathodes [47].

For completeness, results for the frequency of the magnetron operation are briefly discussed. Figure 4-16 shows the output voltage spectrum for the 12-Cavity Rising-Sun Magnetron at an applied magnetic field 0.45 T, with and without the use of endcaps. Different cathode lengths were simulated, and the results shown correspond to 13.5 cm long (Figures 4-16(a) and 4-16(b)), and 18 cm long (Figure 4-16(c)) cathodes. In all cases,

a frequency of about 2.66 GHz was obtained despite the variation in cathode length and structure. Thus, based on the results obtained the system appears quite stable.

Finally, for completeness, the effect of Secondary Electron Emission (SEE) on performance of 12-cavity Rising-Sun magnetron has been probed. The optimized geometry for 12-cavity Rising-Sun magnetron was used for consideration role of SEE. The best length of cathodes in terms of the highest efficiency and the output power, with the lowest leakage current found in previous sections was 18 cm. In addition, the cylindrical endcap encompassing all twelve cathodes was considered for 12 cavity Rising-Sun magnetron. It worth mentioning that the simulation results show that the Rising-Sun geometry with 15◦ degree cavities has a slightly better performance in terms of output power and efficiency over the 20◦ degree cavities. Thus, 15◦ degree cavities were chosen in the present simulation for evaluation the role of secondary emission. For the PIC simulations, 40-ns voltage pulses of magnitude 400 kV with a 4-ns rise-time were applied.

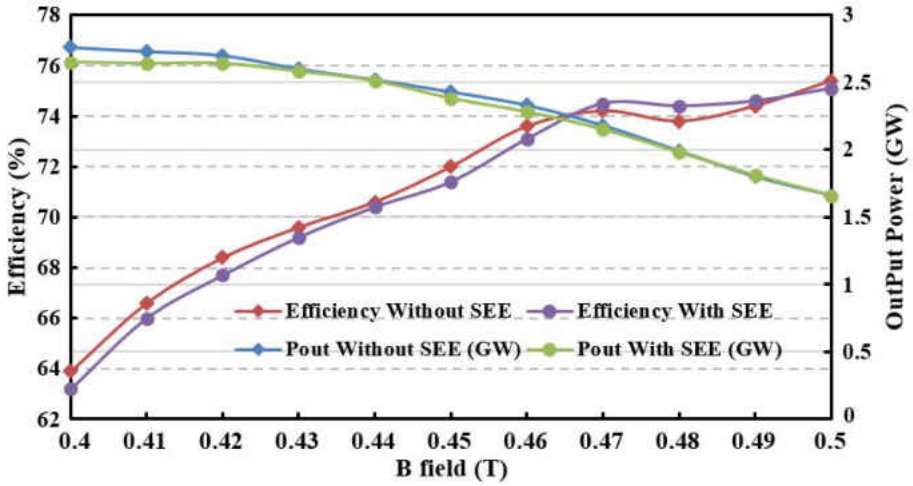


Fig 4-17. PIC simulation results for 12- cavity Rising-Sun magnetron with cylindrical end cap and cathode length 18 cm. The output power and device efficiency are shown as a function of the applied magnetic field with and without the inclusion of SEE.

The output power and efficiency for different applied axial magnetic field strengths with and without the inclusion of SEE from the anode and cathode, are shown in Figure 4- 17.

In addition, Figure 4-18 shows the leakage current of magnetron as a function of applied magnetic field with and without the inclusion of SEE. Both Figures 4-17 and 4-18 show the secondary electron emission does not have the considerable effect on output of magnetron.

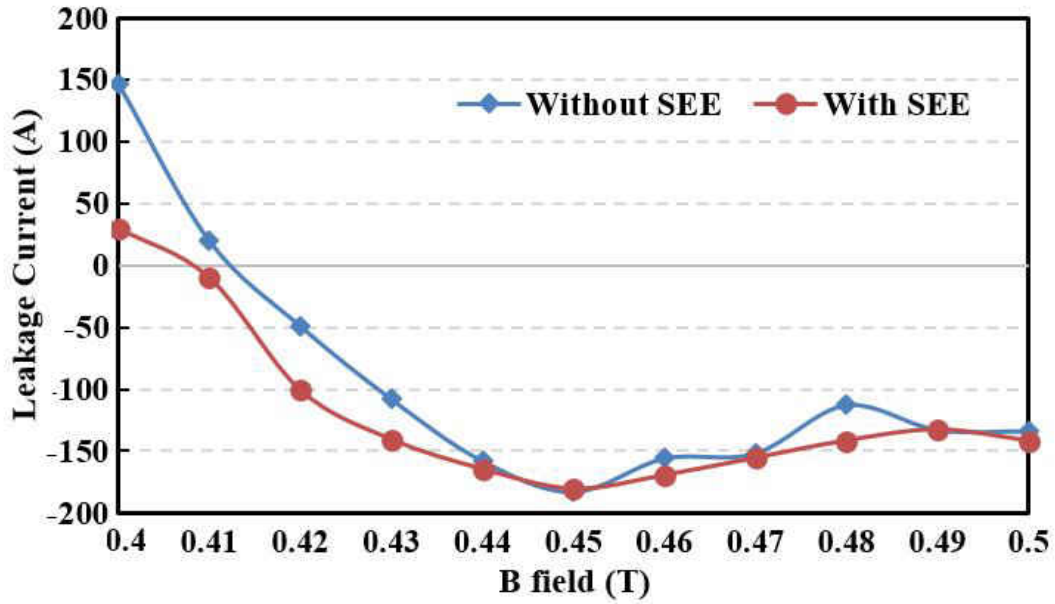


Fig 4-18. PIC simulation results for 12-cavity Rising-Sun magnetron with cylindrical end cap and cathode length 18 cm. The leakage current is shown as a function of the applied magnetic field with and without the inclusion of SEE.

Furthermore, Figure 4-19 depicts the output power as a function of time for applied magnetic fields of 0.45T and 0.47T with and without SEE from the anode and cathode. As Figures 4-19 shows, there is not considerable change in output power; although the decrease of output power with secondary electron emission at the 0.45 T magnetic field (Figure 4-19(a)) is more visible between the 10 ns to 25 ns interval.

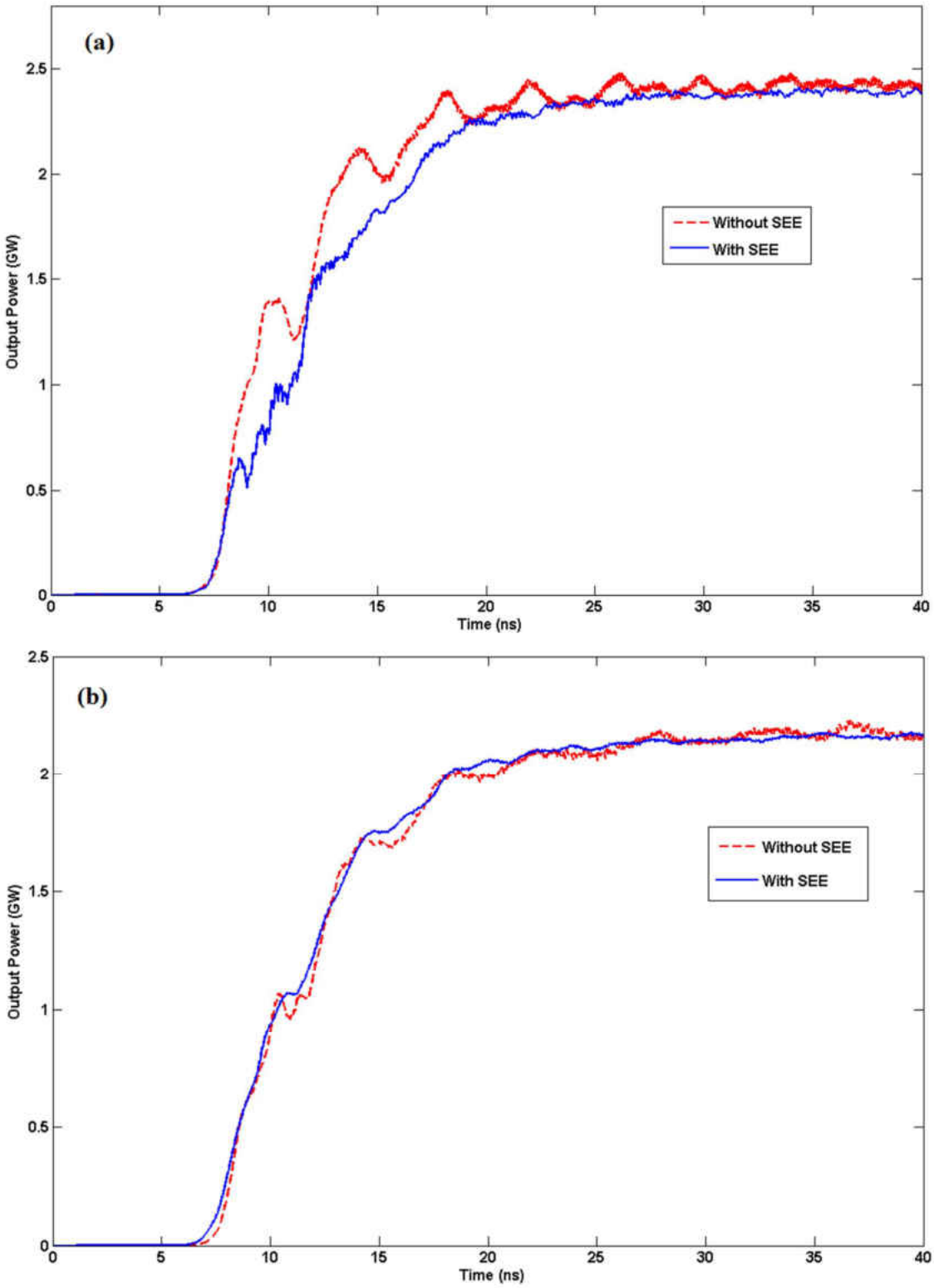


Fig 4-19. MAGIC-based simulation results for the time dependent output power obtained for the 12-Cavity Rising-Sun Magnetron with a cylindrical endcap and 18 cm cathodes for different applied magnetic fields with and without SEE: (a) 0.45 T magnetic field, and (b) 0.47 T magnetic field.

In addition, Figure 4-20 shows the efficiency as a function of time for applied magnetic fields of 0.45T and 0.47T with and without SEE. As with the plots for output power, there are no appreciable changes in efficiency in Figure 4-20. Again, as with the results for output power, the slightly decrease of efficiency in the case of including secondary emission at 0.45 T magnetic field (Figure 4-20(a)) is visible between the 8ns to 25 ns interval.

Overall, as is apparent from the recent figures, there is negligible difference between the curves including SEE and without SEE because of the weak effect of Secondary Electron Emission (SEE). Thus, the role of secondary emission was not found to be very strong for the 12-cavity Rising-Sun magnetron though it did lead to some (a few percent) lowering of the device efficiency.

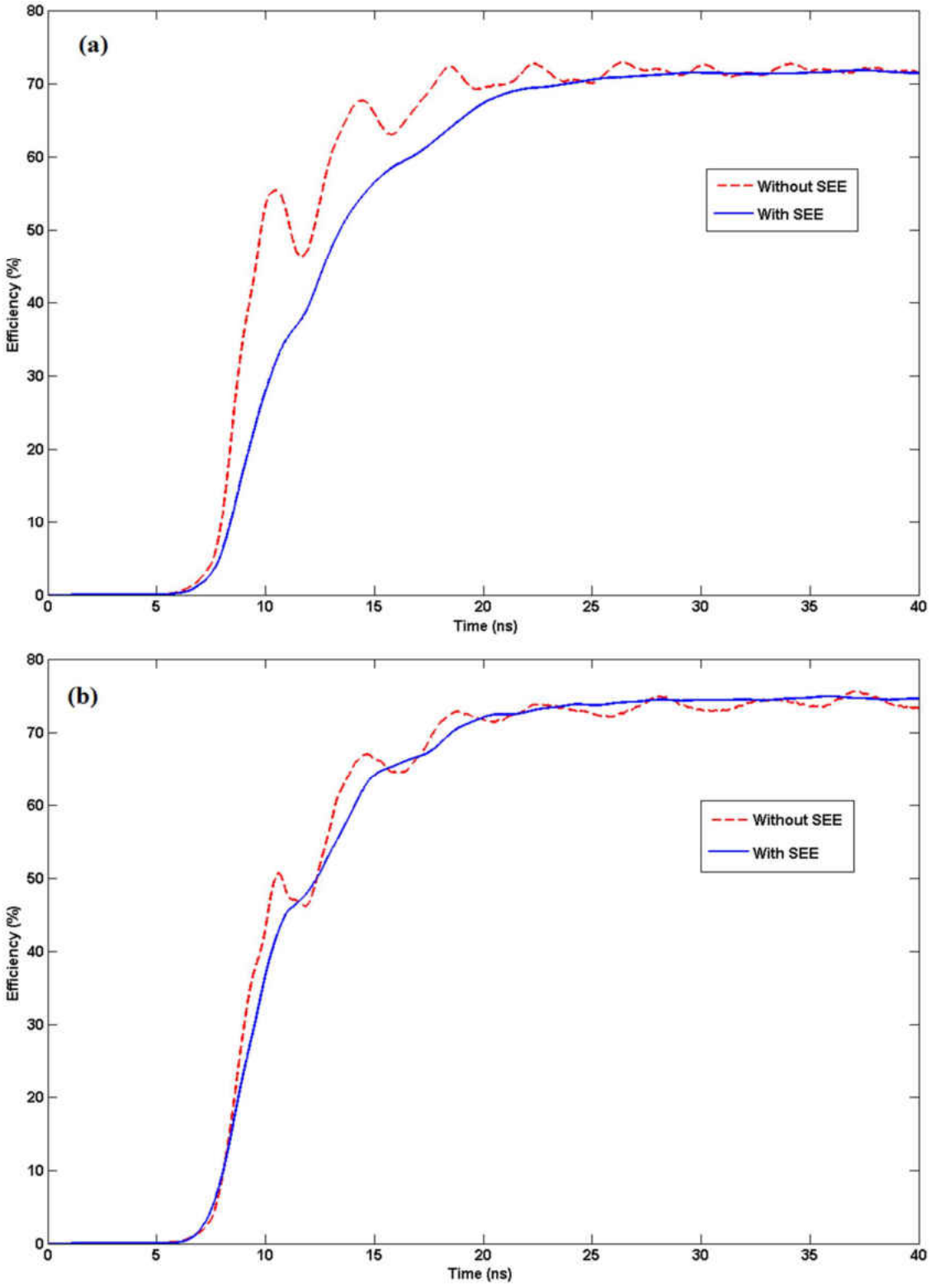


Fig 4-20. MAGIC-based simulation results for the time dependent efficiency obtained for the 12-Cavity Rising-Sun Magnetron with a cylindrical endcap and 18 cm cathodes for different applied magnetic fields with and without SEE: (a) 0.45 T magnetic field, and (b) 0.47 T magnetic field.

# CHAPTER 5

# CONCLUSIONS AND SCOPE FOR FUTURE WORK

## 5-1 Summarizing Conclusions

The A6 magnetron with radial output and uniform emission cylindrical cathode (i.e., ″solid cathode″), was the first relativistic magnetron invented at MIT in 1970s with the capability of producing power in the Megawatt range. The starting time and build-up of microwave oscillations in magnetrons with solid cathode is very slow. Thus, the ″transparent cathode″ was proposed as a mean of improving the overall performance of A6 relativistic magnetron and decreasing the start time of oscillations, which can lead to short pulses for ultrawideband applications. The transparent cathode is a hollow cathode with longitudinal strips of material removed in a symmetric angular fashion. As a result, the transparent cathode consists of a district number of individual emitters. The strong azimuthal RF electric field in transparent cathodes, as compared to zero amount in solid cathode, quickly captures pre-bunched electrons into the rotating spokes. This phenomenon provides the improved condition for the fast conversion of the electron potential energy into electromagnetic energy.

Magnetrons with diffraction output (MDO) is another important class of relativistic magnetrons that has been proposed in recent years. While most relativistic magnetrons extract the output power radially from a slot located in their cavities, in axial diffraction output magnetrons (MDOs), the radiation is extracted axially along the vanes of the anode block via a horn antenna or multiple waveguides. In a MDO, the vanes of the anode block are continued and tapered within inside of a conical horn antenna. In addition, Rising-Sun

geometry was created and designed to achieve mode stability. This device geometry consists of two alternating groups of short and long vanes in angular orientation, that help create greater frequency separation between the modes and prevent mode competition.

The use of cathode endcaps has been one of the performance enhancing aspect studied both through experiments and simulations. The physics associated with the improvement is based on two aspects. First, the metallic endcaps shape the electric fields and help define the effective electrical length of the cathode. In addition, electron leakage currents can be suppressed and the output window of the MDO would be protected from electron bombardment.

The Particle-in-cell (PIC) code simulates the motion of plasma particles and calculates all macro- quantities from the position and velocity of these particles. Particle-in-cell based MAGIC software tool has been used in this thesis for modeling and simulation of magnetron to obtain the optimized geometry based on the device performance.

In the first part, Particle-in-cell simulations were performed to provide a numerical analysis of the efficiency, output power and leakage currents in an A6 magnetron with diffraction output and transparent cathode. The central goal was to evaluate the role of cathode length, different types of endcap, and location of cathodes in respect with anode block, as a function of different applied magnetic fields, on the output power, efficiency and leakage current of magnetron. In reality, the parameter space is really large, and so for convenience the basic dimensions and geometry were confined to that used in recent reports of the A6 relativistic magnetron.

Simulation results, in keeping with previous reports, demonstrate the definite advantage of having endcaps. Though the use of individual endcaps was probed, the performance was not shown to significantly improve over a single, comprehensive endcap. Given the ease of manufacture, a single endcap would, therefore, provide a more practical implementation. The results demonstrated peak output power in excess of 1 GW, with efficiencies on the order of 66% for B-field in the 0.4 T - 0.42 T range. For optimization, the relative angular displacement of the cathode relative to the anode was obtained to be about 55° degrees.

Furthermore, Particle-in-cell simulations were performed to provide a numerical evaluation of the efficiency, output power and leakage currents in a 12-cavitiy, 12-cathode Rising-Sun magnetron with diffraction output. The central goal was to conduct a parameter study of a Rising-Sun magnetron that comprehensively incorporated performance enhancing features such as transparent cathodes, axial extraction, the use of endcaps, and cathode extensions. Once again, the basic dimensions and geometry were confined to that used in recent reports of the A6 relativistic magnetron and the different conditions analyzed for optimized shape and angle of the short vanes in the structure. The results for this part again show the definite advantage of having endcaps. A 45° degree angle was obtained as the optimized value for the short vanes of the Rising-Sun magnetron, with the slope of other vanes kept fixed at 32° degrees (an optimized angle reported in previous reports). The simulations here also demonstrated peak output power in excess of 2GW, with efficiencies on the order of 68% for B-fields in the 0.42 T - 0.46 T range. For further optimization, the role of the cathode length and its extension beyond the anode dimensions was probed. The

results show the efficiency in excess of 70% and peak output power on the order of 2.1GW for an 18 cm cathode length at 0.45 T magnetic field and 400 kV applied voltage.

Finally, the role of secondary electron emission (SEE) on performance of 12-cavity Rising-Sun magnetron was performed in this thesis research. The Particle-In-Cell simulations based on the MAGIC tool were performed to provide a numerical analysis into efficiency, output power, and leakage currents. The simulation results show the weak effect of Secondary Electron Emission (SEE) on output power, efficiency and leakage current of magnetron. Thus, the role of secondary emission was not found to be very strong for the 12-cavity Rising-Sun magnetron, though it did lead to some (a few percent) lowering of the device efficiency.

**5-2 Scope for Future Work**

Based on the research work described in this thesis, some of the other areas for further research and simulation aspects for future studies are briefly described as follows:

1) Experimental works on Rising-Sun magnetron with different geometries which could be the best way for confirmation of the MAGIC-based simulation results.
2) Carrying out 3D MAGIC simulation with different shapes of cathode such as the cathodes with sharp edges in order to increase the local electric field and enhancing electron emission for the cathode.
3) Studying and Particle-in-cell MAGIC-based simulation on the operation of a compact relativistic magnetron with a virtual cathode (VC) in the interaction space of the device, instead of a physical cathode.

4) Simulation and research on the effect of changing the cathode strip position on the operation mode of magnetron.
5) Consideration of the effect of cascading electron emission in Secondary Electron Emission (SEE) in Rising-Sun MDO magnetron.
6) A study of magnetron performance with the anode cavities partially or fully filled with dielectrics could be carried out. This model would provide variable frequency operation, especially if liquid oils could be used in piston-like containers of variable length.

# REFERENCES


[1] A. Palevsky and G. Bekefi, "Microwave emission from pulsed, relativistic e-beam diodes. II. The multiresonator magnetron," *Physics of Fluids,* vol. 22, pp. 986-996, 1979.

[2] M. Fuks, S. Prasad, and E. Schamiloglu, "Increased efficiency and faster turn-on in magnetrons using the transparent cathode," in *International Conference on the Origins and Evolution of the Cavity Magnetron (CAVMAG)*, 2010, pp. 76-81.

[3] M. I. Fuks and E. Schamiloglu, "70% efficient relativistic magnetron with axial extraction of radiation through a horn antenna," *IEEE Transactions on Plasma Science,* vol. 38, pp. 1302-1312, 2010.

[4] M. Daimon and W. Jiang, "Modified configuration of relativistic magnetron with diffraction output for efficiency improvement," *Applied Physics Letters,* vol. 91, pp. 191503, 2007.

[5] C. Leach, S. Prasad, M. I. Fuks, and E. Schamiloglu, "Suppression of leakage current in a relativistic magnetron using a novel design cathode endcap," *IEEE Transactions on Plasma Science,* vol. 40, pp. 2089-2093, 2012.

[6] J. P. Verboncoeur, "Particle simulation of plasmas: review and advances," *Plasma Physics and Controlled Fusion,* vol. 47, pp. A231-A260, 2005.

[7] A. M. Spirkin, "A three-dimensional Particle-in-Cell methodology on unstructured voronoi grids," Ph.D. dissertation, Dept. Mech. Eng., Worcester Polytechnic Institute, Worcester, MA, 2006.

[8] J. Benford, J. A. Swegle, and E. Schamiloglu, *High Power Microwaves*, 2nd edition, New York, Taylor and Francis, 2007.

[9] H. A. H. Boot and J. T. Randall, "Historical notes on the cavity magnetron," *IEEE Transactions on Electron Devices,* vol. 23, pp. 724-729, 1976.

[10] G. B. Collins, *Microwave Magnetrons*. New York: McGraw-Hill Book Co., 1948.

[11] C. J. Leach, "High efficiency axial diffraction output schemes for the A6 relativistic magnetron," Ph.D. dissertation, Dept. Elect. Eng., Univ. of New Mexico, Albuquerque, NM, 2014.

[12] A. V. Hollenberg, N. Kroll, and S. Millman, "Rising Sun magnetrons with large numbers of cavities," *Journal of Applied Physics,* vol. 19, pp. 624, 1948.

[13] S. Millman and A. T. Nordsieck, "The Rising Sun magnetron," *Journal of Applied Physics,* vol. 19, pp. 156, 1948.

[14] T. A. Treado, W. O. Doggett, G. E. Thomas, R. S. Smith, III, J. Jackson-Ford, and D. J. Jenkins, "Operating modes of relativistic Rising-Sun and A6 magnetrons," *IEEE Transactions on Plasma Science,* vol. 16, pp. 237-248, 1988.

[15] H. J. Kim, J. U. Shin, and J. J. Choi, "Particle-in-cell code simulations and experiments of a Rising-Sun magnetron oscillator," in *Vacuum Electronics Conference IVEC 2002, Third IEEE International*, 2002, pp. 209-210.

[16] D.-F. Shi, B.-L. Qian, H.-G. Wang, and W. Li, "Derivation and generalization of the dispersion relation of Rising-Sun magnetron with sectorial and rectangular cavities," *Physics of Plasmas,* vol. 20, pp. 123113, 2013.

[17] A. K. Ganguly, G. S. Park, and C. M. Armstrong, "Nonlinear theory of harmonic peniotron and gyrotron interactions in a Rising-Sun slotted waveguide," *IEEE Transactions on Plasma Science,* vol. 22, pp. 902-912, 1994.

[18] R. W. Lemke, T. C. Genoni, and T. A. Spencer, "Investigation of Rising-Sun magnetrons operated at relativistic voltages using three-dimensional particle-in-cell simulation," *Physics of Plasmas,* vol. 7, pp. 706-714, 2000.

[19] K. Hae Jin, S. Jung Uk, and C. Jin Joo, "Particle-in-cell code simulations on a Rising-Sun magnetron oscillator," *IEEE Transactions on Plasma Science,* vol. 30, pp. 956-961, 2002.

[20] S. Fernandez-Gutierrez, J. Browning, M. C. Lin, D. N. Smithe, and J. Watrous, "Simulation of a Rising-Sun magnetron employing a faceted cathode with a continuous current source," *Journal of Vacuum Science & Technology B,* vol. 32, pp. 6, Nov 2014.

[21] M. Liu, E. Schamiloglu, W. Jiang, F. Mikhail, and C. Liu, "Investigation of a 12-cavity Rising-Sun relativistic magnetron with diffraction output using particle-in-cell simulation," in *2014 IEEE International Power Modulator and High Voltage Conference (IPMHVC),* 2014, pp. 333-336.

[22] Y. M. Saveliev, S. N. Spark, B. A. Kerr, M. I. Harbour, S. C. Douglas, and W. Sibbett, "Effect of cathode end caps and a cathode emissive surface on relativistic magnetron operation," *IEEE Transactions on Plasma Science,* vol. 28, pp. 478-484, 2000.

[23] M. R. Lopez, R. M. Gilgenbach, D. W. Jordan, S. A. Anderson, M. D. Johnston, M. W. Keyser*, et al.*, "Cathode effects on a relativistic magnetron driven by a microsecond e-beam accelerator," *IEEE Transactions on Plasma Science,* vol. 30, pp. 947-955, 2002.

[24] H. L. Bosman, M. I. Fuks, S. Prasad, and E. Schamiloglu, "Improvement of the output characteristics of magnetrons using the transparent cathode," *IEEE Transactions on Plasma Science,* vol. 34, pp. 606-619, 2006.

[25] M. C. Jones, V. B. Neculaes, Y. Y. Lau, R. M. Gilgenbach, W. M. White, B. W. Hoff*, et al.*, "Magnetron priming by multiple cathodes," *Applied Physics Letters,* vol. 87, p. 081501, 2005.

[26] V. Bogdan Neculaes, M. C. Jones, R. M. Gilgenbach, Y. Y. Lau, J. W. Luginsland, B. W. Hoff*, et al.*, "Magnetic priming effects on noise, startup, and mode competition in magnetrons," *IEEE Transactions on Plasma Science,* vol. 33, pp. 94-102, 2005.

[27] V. Bogdan Neculaes, M. C. Jones, R. M. Gilgenbach, Y. Y. Lau, J. W. Luginsland, B. W. Hoff*, et al.*, "Magnetic perturbation effects on noise and startup in DC-operating oven magnetrons," *IEEE Transactions on Electron Devices,* vol. 52, pp. 864-871, 2005.

[28] M. C. Jones, V. B. Neculaes, Y. Y. Lau, R. M. Gilgenbach, and W. M. White, "Cathode priming of a relativistic magnetron," *Applied Physics Letters,* vol. 85, pp. 6332-6334, 2004.

[29] S. Prasad, M. Roybal, C. J. Buchenauer, K. Prestwich, M. Fuks, and E. Schamiloglu, "Experimental verification of the advantages of the transparent cathode in a short-pulse magnetron," in *2009 IEEE Pulsed Power Conference,* 2009, pp. 81-85.

[30] M. Fuks and E. Schamiloglu, "Rapid start of oscillations in a magnetron with a "transparent" cathode," *Physical Review Letters,* vol. 95, pp. 205101, 2005.

[31] G. Lapenta. *Particle In Cell Method A brief description of the PIC Method* [Online]. Available: https://perswww.kuleuven.be/~u0052182/weather/pic.pdf

[32] R. S. Holger Fehske, Alexander Weisse, *Computational Many-Particle Physics*. Berlin, Germany: Springer, 2008.

[33] G. A. E. Vandenbosch, "Computational Electromagnetics in Plasmonics," in Plasmonic-Principles and Applications, 2012, Ch.2, pp. 23-48.

[34] Y. Kane, "Numerical solution of initial boundary value problems involving maxwell's equations in isotropic media," *IEEE Transactions on Antennas and Propagation,* vol. 14, pp. 302-307, 1966.

[35] A. Farid, A. N. Alshawabkeh and C. M. Rappaport, "Electromagnetic Waves Propagation in Complex Matter," in *Electromagnetic Waves Propagation in Complex Matter.*, In Tech, July 2011, Ch. 5, pp. 117-154.

[36] B. Goplen, L. Ludeking, D. Smith, and G. Warren, "User-configurable MAGIC for electromagnetic PIC calculations," *Computer Physics Communications,* vol. 87, pp. 54-86, 1995.

[37] V. Jujjavarapu, "Numerical studies of the A6 relativistic magnetron using Particle-In-Cell simulations," M.S. Thesis, Dept. Elect. Eng., Old Dominion Univ., Norfolk, VA., 2014.

[38] S. Parasad, "Fast start of oscillations in a short-pulse relativistic magnetron driven by a transparent cathode," Ph.D. dissertation, Dept. Elect. Eng., Univ. of New Mexico, Albuquerque, NM, 2010.

[39] L. Ludeking, A. Woods, L. Cavey, "MAGIC 3.2.4 Help Manual Technical Report," Alliant Techsystems (ATK), Newington, VA., Feb. 2014.

[40] G. N. Fursey, M. A. Polyakov, L. A. Shirochin, and A. N. Saveliev, "Liquid carbon surface during explosive emission," *Applied Surface Science,* vol. 215, pp. 286-290, 2003.

[41] A. Majzoobi, R. P. Joshi, A. Neuber, and J. Dickens, "Analysis of cathode emission phenomena: Effects of barrier thinning, field enhancements and local heating," in *2015 IEEE Pulsed Power Conference (PPC),* 2015, pp. 1-4.

[42] L. Meiqin, L. Chunliang, M. I. Fuks, and E. Schamiloglu, "Operation characteristics of 12-cavity relativistic magnetron with single-stepped cavities," *IEEE Transactions on Plasma Science,* vol. 42, pp. 3283-3287, 2014.

[43] L. Meiqin, M. I. Fuks, E. Schamiloglu, and L. Chunliang, "Operation characteristics of A6 relativistic magnetron using single-stepped cavities with axial extraction," *IEEE Transactions on Plasma Science,* vol. 42, pp. 3344-3348, 2014.

[44] C. Leach, S. Prasad, M. I. Fuks, and E. Schamiloglu, "Compact relativistic magnetron with Gaussian radiation pattern," *IEEE Transactions on Plasma Science,* vol. 40, pp. 3116-3120, 2012.

[45] L. Meiqin, M. I. Fuks, E. Schamiloglu, and L. Chun-Liang, "Frequency switching in a 12-cavity relativistic magnetron with axial extraction of radiation," *IEEE Transactions on Plasma Science,* vol. 40, pp. 1569-1574, 2012.

[46] L. Meiqin, E. Schamiloglu, M. I. Fuks, L. Chunliang, and J. Weihua, "Operation characteristics of a 12-cavity relativistic magnetron when considering secondary and backscattered electrons' emission," *IEEE Transactions on Plasma Science,* vol. 43, pp. 1855-1861, 2015.

[47] A. Majzoobi, R. P. Joshi, A. A. Neuber, and J. C. Dickens, "Particle-in-cell based parameter study of 12-cavity, 12-cathode rising-sun relativistic magnetrons for improved performance," *AIP Advances,* vol. 5, pp. 107102, 2015.

[48] K. F. R. Courant, and H. Lewy, , "On the partial difference equations of mathematical physics," *IBM Journal of Research and Development,* vol. 11, pp. 215-234, 1967.

# APPENDIX

## Thesis / Dissertation Reuse

**The IEEE does not require individuals working on a thesis to obtain a formal reuse license, however, you may print out this statement to be used as a permission grant:**

*Requirements to be followed when using any portion (e.g., figure, graph, table, or textual material) of an IEEE copyrighted paper in a thesis:*

1) In the case of textual material (e.g., using short quotes or referring to the work within these papers) users must give full credit to the original source (author, paper, publication) followed by the IEEE copyright line © 2011 IEEE.
2) In the case of illustrations or tabular material, we require that the copyright line © [Year of original publication] IEEE appear prominently with each reprinted figure and/or table.
3) If a substantial portion of the original paper is to be used, and if you are not the senior author, also obtain the senior author's approval.

*Requirements to be followed when using an entire IEEE copyrighted paper in a thesis:*

1) The following IEEE copyright/ credit notice should be placed prominently in the references: © [year of original publication] IEEE. Reprinted, with permission, from [author names, paper title, IEEE publication title, and month/year of publication]
2) Only the accepted version of an IEEE copyrighted paper can be used when posting the paper or your thesis on-line.
3) In placing the thesis on the author's university website, please display the following message in a prominent place on the website: In reference to IEEE copyrighted material which is used with permission in this thesis, the IEEE does not endorse any of [university/educational entity's name goes here]'s products or services. Internal or personal use of this material is permitted. If interested in reprinting/republishing IEEE copyrighted material for advertising or promotional purposes or for creating new collective works for resale or redistribution, please go to http://www.ieee.org/publications_standards/publications/rights/rights_link.html to learn how to obtain a License from RightsLink.

If applicable, University Microfilms and/or ProQuest Library, or the Archives of Canada may supply single copies of the dissertation.

Copyright Clearance Center

**Note:** Copyright.com supplies permissions but not the copyrighted content itself.

1 PAYMENT 2 REVIEW 3 CONFIRMATION

## Step 3: Order Confirmation

**Thank you for your order!** A confirmation for your order will be sent to your account email address. If you have questions about your order, you can call us at +1.855.239.3415 Toll Free, M-F between 3:00 AM and 6:00 PM (Eastern), or write to us at info@copyright.com. This is not an invoice.

**Confirmation Number: 11503837**
**Order Date: 12/04/2015**

If you paid by credit card, your order will be finalized and your card will be charged within 24 hours. If you choose to be invoiced, you can change or cancel your order until the invoice is generated.

### Payment Information

Alireza Majzoobi
a.majzoobi@gmail.com
+1 (757)4052532
Payment Method: n/a

### Order Details

#### High power microwaves

| | |
|---|---|
| **Order detail ID:** | 69155645 |
| **Order License Id:** | 3761720231893 |
| **ISBN:** | 978-0-7503-0706-2 |
| **Publication Type:** | Book |
| **Publisher:** | TAYLOR & FRANCIS GROUP LLC - BOOKS |
| **Author/Editor:** | BENFORD J |

**Permission Status:** Granted
**Permission type:** Republish or display content
**Type of use:** Republish in a thesis/dissertation

| | |
|---|---|
| **Requestor type** | Academic institution |
| **Format** | Print, Electronic |
| **Portion** | image/photo |
| **Number of images/photos requested** | 1 |
| **Title or numeric reference of the portion(s)** | Chapter 7, Figure 7.11 |
| **Title of the article or chapter the portion is from** | N/A |
| **Editor of portion(s)** | N/A |

| | |
|---|---|
| **Author of portion(s)** | N/A |
| **Volume of serial or monograph** | N/A |
| **Issue, if republishing an article from a serial** | N/A |
| **Page range of portion** | 100 |
| **Publication date of portion** | N/A |
| **Rights for** | Main product |
| **Duration of use** | Life of current edition |
| **Creation of copies for the disabled** | no |
| **With minor editing privileges** | no |
| **For distribution to** | United States |
| **In the following language(s)** | Original language of publication |
| **With incidental promotional use** | no |
| **Lifetime unit quantity of new product** | Up to 499 |
| **Made available in the following markets** | N/A |
| **The requesting person/organization** | Alireza Majzoobi, M.Sc Thesis |
| **Order reference number** | |
| **Author/Editor** | Alireza Majzoobi |
| **The standard identifier** | N/A |
| **The proposed price** | N/A |
| **Title** | Numerical studies of MDO magnetron using Particle-In-Cell simulations |
| **Publisher** | Old Dominion University |

| | |
|---|---|
| **Expected publication date** | Dec 2015 |
| **Estimated size (pages)** | 100 |

**Note:** This item will be invoiced or charged separately through CCC's **RightsLink** service. More info **$ 0.00**

**This is not an invoice.**

**Total order items:** 1 **Order Total: 0.00 USD**

**Confirmation Number: 11503837**

**Special Rightsholder Terms & Conditions**

The following terms & conditions apply to the specific publication under which they are listed

**High power microwaves**
**Permission type:** Republish or display content
**Type of use:** Republish in a thesis/dissertation

**TERMS AND CONDITIONS**

**The following terms are individual to this publisher:**

Taylor and Francis Group and Informa healthcare are division of Informa plc. Permission will be void if material exceeds 10% of all the total pages in your publication and over 20% of the original publication. This includes permission granted by Informa plc and all of its subsidaries.

**Other Terms and Conditions:**

**STANDARD TERMS AND CONDITIONS**

1. Description of Service; Defined Terms. This Republication License enables the User to obtain licenses for republication of one or more copyrighted works as described in detail on the relevant Order Confirmation (the "Work(s)"). Copyright Clearance Center, Inc. ("CCC") grants licenses through the Service on behalf of the rightsholder identified on the Order Confirmation (the "Rightsholder"). "Republication", as used herein, generally means the inclusion of a Work, in whole or in part, in a new work or works, also as described on the Order Confirmation. "User", as used herein, means the person or entity making such republication.

2. The terms set forth in the relevant Order Confirmation, and any terms set by the Rightsholder with respect to a particular Work, govern the terms of use of Works in connection with the Service. By using the Service, the person transacting for a republication license on behalf of the User represents and warrants that he/she/it (a) has been duly authorized by the User to accept, and hereby does accept, all such terms and conditions on behalf of User, and (b) shall inform User of all such terms and conditions. In the event such person is a "freelancer" or other third party independent of User and CCC, such party shall be deemed jointly a "User" for purposes of these terms and conditions. In any event, User shall be deemed to have accepted and agreed to all such terms and conditions if User republishes the Work in any fashion.

**3. Scope of License; Limitations and Obligations.**

3.1 All Works and all rights therein, including copyright rights, remain the sole and exclusive property of the Rightsholder. The license created by the exchange of an Order Confirmation (and/or any invoice) and payment by User of the full amount set forth on that document includes only those rights expressly set forth in the Order Confirmation and in these terms and conditions, and conveys no other rights in the Work(s) to User. All rights not expressly granted are hereby reserved.

3.2 General Payment Terms: You may pay by credit card or through an account with us payable at the end of the month. If you and we agree that you may establish a standing account with CCC, then the following terms apply: Remit Payment to: Copyright Clearance Center, Dept 001, P.O. Box 843006, Boston, MA 02284-3006. Payments Due: Invoices are payable upon their delivery to you (or upon our notice to you that they are available to you for downloading). After 30 days, outstanding amounts will be subject to a service charge of 1-1/2% per month or, if less, the maximum rate allowed by applicable law. Unless otherwise specifically set forth in the Order Confirmation or in a separate written agreement signed by CCC, invoices are due and payable on "net 30" terms. While User may exercise the rights licensed immediately upon issuance of the Order Confirmation, the license is automatically revoked and is null and void, as if it had never been issued, if complete payment for the license is not received on a timely basis either from User directly or through a payment agent, such as a credit card company.

3.3 Unless otherwise provided in the Order Confirmation, any grant of rights to User (i) is "one-time" (including the editions and product family specified in the license), (ii) is non-exclusive and non-transferable and (iii) is subject to any and all limitations and restrictions (such as, but not limited to, limitations on duration of use or circulation) included in the Order Confirmation or invoice and/or in these terms and conditions. Upon completion of the licensed use, User shall either secure a new permission for further use of the Work(s) or immediately cease any new use of the Work(s) and shall render inaccessible (such as by deleting or by removing or severing links or other locators) any further copies of the Work (except for copies printed on paper in accordance with this license and still in User's stock at the end of such period).

3.4 In the event that the material for which a republication license is sought includes third party materials (such as photographs, illustrations, graphs, inserts and similar materials) which are identified in such material as having been used by permission, User is responsible for identifying, and seeking separate licenses (under this Service or otherwise) for, any of such third party materials; without a separate license, such third party materials may not be used.

3.5 Use of proper copyright notice for a Work is required as a condition of any license granted under the Service.

Unless otherwise provided in the Order Confirmation, a proper copyright notice will read substantially as follows: "Republished with permission of [Rightsholder's name], from [Work's title, author, volume, edition number and year of copyright]; permission conveyed through Copyright Clearance Center, Inc. " Such notice must be provided in a reasonably legible font size and must be placed either immediately adjacent to the Work as used (for example, as part of a by-line or footnote but not as a separate electronic link) or in the place where substantially all other credits or notices for the new work containing the republished Work are located. Failure to include the required notice results in loss to the Rightsholder and CCC, and the User shall be liable to pay liquidated damages for each such failure equal to twice the use fee specified in the Order Confirmation, in addition to the use fee itself and any other fees and charges specified.

3.6 User may only make alterations to the Work if and as expressly set forth in the Order Confirmation. No Work may be used in any way that is defamatory, violates the rights of third parties (including such third parties' rights of copyright, privacy, publicity, or other tangible or intangible property), or is otherwise illegal, sexually explicit or obscene. In addition, User may not conjoin a Work with any other material that may result in damage to the reputation of the Rightsholder. User agrees to inform CCC if it becomes aware of any infringement of any rights in a Work and to cooperate with any reasonable request of CCC or the Rightsholder in connection therewith.

4. Indemnity. User hereby indemnifies and agrees to defend the Rightsholder and CCC, and their respective employees and directors, against all claims, liability, damages, costs and expenses, including legal fees and expenses, arising out of any use of a Work beyond the scope of the rights granted herein, or any use of a Work which has been altered in any unauthorized way by User, including claims of defamation or infringement of rights of copyright, publicity, privacy or other tangible or intangible property.

5. Limitation of Liability. UNDER NO CIRCUMSTANCES WILL CCC OR THE RIGHTSHOLDER BE LIABLE FOR ANY DIRECT, INDIRECT, CONSEQUENTIAL OR INCIDENTAL DAMAGES (INCLUDING WITHOUT LIMITATION DAMAGES FOR LOSS OF BUSINESS PROFITS OR INFORMATION, OR FOR BUSINESS INTERRUPTION) ARISING OUT OF THE USE OR INABILITY TO USE A WORK, EVEN IF ONE OF THEM HAS BEEN ADVISED OF THE POSSIBILITY OF SUCH DAMAGES. In any event, the total liability of the Rightsholder and CCC (including their respective employees and directors) shall not exceed the total amount actually paid by User for this license. User assumes full liability for the actions and omissions of its principals, employees, agents, affiliates, successors and assigns.

6. Limited Warranties. THE WORK(S) AND RIGHT(S) ARE PROVIDED "AS IS". CCC HAS THE RIGHT TO GRANT TO USER THE RIGHTS GRANTED IN THE ORDER CONFIRMATION DOCUMENT. CCC AND THE RIGHTSHOLDER DISCLAIM ALL OTHER WARRANTIES RELATING TO THE WORK(S) AND RIGHT(S), EITHER EXPRESS OR IMPLIED, INCLUDING WITHOUT LIMITATION IMPLIED WARRANTIES OF MERCHANTABILITY OR FITNESS FOR A PARTICULAR PURPOSE. ADDITIONAL RIGHTS MAY BE REQUIRED TO USE ILLUSTRATIONS, GRAPHS, PHOTOGRAPHS, ABSTRACTS, INSERTS OR OTHER PORTIONS OF THE WORK (AS OPPOSED TO THE ENTIRE WORK) IN A MANNER CONTEMPLATED BY USER; USER UNDERSTANDS AND AGREES THAT NEITHER CCC NOR THE RIGHTSHOLDER MAY HAVE SUCH ADDITIONAL RIGHTS TO GRANT.

7. Effect of Breach. Any failure by User to pay any amount when due, or any use by User of a Work beyond the scope of the license set forth in the Order Confirmation and/or these terms and conditions, shall be a material breach of the license created by the Order Confirmation and these terms and conditions. Any breach not cured within 30 days of written notice thereof shall result in immediate termination of such license without further notice. Any unauthorized (but licensable) use of a Work that is terminated immediately upon notice thereof may be liquidated by payment of the Rightsholder's ordinary license price therefor; any unauthorized (and unlicensable) use that is not terminated immediately for any reason (including, for example, because materials containing the Work cannot reasonably be recalled) will be subject to all remedies available at law or in equity, but in no event to a payment of less than three times the Rightsholder's ordinary license price for the most closely analogous licensable use plus Rightsholder's and/or CCC's costs and expenses incurred in collecting such payment.

8. **Miscellaneous.**

8.1 User acknowledges that CCC may, from time to time, make changes or additions to the Service or to these terms and conditions, and CCC reserves the right to send notice to the User by electronic mail or otherwise for the purposes of notifying User of such changes or additions; provided that any such changes or additions shall not apply to permissions already secured and paid for.

8.2 Use of User-related information collected through the Service is governed by CCC's privacy policy, available online here: http://www.copyright.com/content/cc3/en/tools/footer/privacypolicy.html.

8.3 The licensing transaction described in the Order Confirmation is personal to User. Therefore, User may not assign or transfer to any other person (whether a natural person or an organization of any kind) the license created by the Order Confirmation and these terms and conditions or any rights granted hereunder; provided, however, that User may assign such license in its entirety on written notice to CCC in the event of a transfer of all or substantially all of User's rights in the new material which includes the Work(s) licensed under this Service.

8.4 No amendment or waiver of any terms is binding unless set forth in writing and signed by the parties. The Rightsholder and CCC hereby object to any terms contained in any writing prepared by the User or its principals, employees, agents or affiliates and purporting to govern or otherwise relate to the licensing transaction described in the Order Confirmation, which terms are in any way inconsistent with any terms set forth in the Order Confirmation and/or in these terms and conditions or CCC's standard operating procedures, whether such writing is prepared prior to, simultaneously with or subsequent to the Order Confirmation, and whether such writing appears on a copy of the Order Confirmation or in a separate instrument.

8.5 The licensing transaction described in the Order Confirmation document shall be governed by and construed under the law of the State of New York, USA, without regard to the principles thereof of conflicts of law. Any case, controversy, suit, action, or proceeding arising out of, in connection with, or related to such licensing transaction shall be brought, at CCC's sole discretion, in any federal or state court located in the County of New York, State of New

York, USA, or in any federal or state court whose geographical jurisdiction covers the location of the Rightsholder set forth in the Order Confirmation. The parties expressly submit to the personal jurisdiction and venue of each such federal or state court.If you have any comments or questions about the Service or Copyright Clearance Center, please contact us at 978-750-8400 or send an e-mail to info@copyright.com.

v 1.1

Close

**Confirmation Number: 11503837**

**Citation Information**

**Order Detail ID:** 69155645

**High power microwaves by BENFORD J Reproduced with permission of TAYLOR & FRANCIS GROUP LLC - BOOKS in the format Republish in a thesis/dissertation via Copyright Clearance Center.**

Close


| | |
|---|---|
| **Title:** | Microwave emission from pulsed, relativistic e-beam diodes. II. The multiresonator magnetron |
| **Author:** | A. Palevsky,G. Bekefi |
| **Publication:** | Physics of Fluids 1958-1988 |
| **Volume/Issue** | 22/5 |
| **Publisher:** | AIP Publishing LLC |
| **Date:** | Aug 6, 2008 |
| **Page Count:** | 11 |





## Order Completed

Thank you very much for your order.

Click here for Payment Terms and Conditions.

Get a printable version for your records.

| | |
|---|---|
| License Number | 3762801021095 |
| Order Date | Dec 05, 2015 |
| Publisher | AIP Publishing LLC |
| Publication | Physics of Fluids 1958-1988 |
| Article Title | Microwave emission from pulsed, relativistic e-beam diodes. II. The multiresonator magnetron |
| Author | A. Palevsky,G. Bekefi |
| Online Publication Date | Aug 6, 2008 |
| Volume number | 22 |
| Issue number | 5 |
| Type of Use | Thesis/Dissertation |
| Requestor type | Student |
| Format | Print and electronic |
| Portion | Figure/Table |
| Number of figures/tables | 1 |
| Title of your thesis / dissertation | NUMERICAL STUDIES AND OPTIMIZATION OF MAGNETRON WITH DIFFRACTION OUTPUT (MDO) USING PARTICLE-IN-CELL SIMULATIONS |
| Expected completion date | Dec 2015 |
| Estimated size (number of pages) | 100 |
| Total | 0.00 USD |

ORDER MORE... CLOSE WINDOW

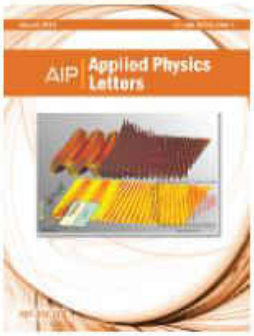


**Title:** Modified configuration of relativistic magnetron with diffraction output for efficiency improvement

**Author:** M. Daimon,W. Jiang

**Publication:** Applied Physics Letters

**Volume/Issue** 91/19

**Publisher:** AIP Publishing LLC

**Date:** Nov 9, 2007

**Page Count:** 3



## Order Completed

Thank you very much for your order.

Click here for Payment Terms and Conditions.

Get a printable version for your records.

| | |
|---|---|
| License Number | 3762801235356 |
| Order Date | Dec 05, 2015 |
| Publisher | AIP Publishing LLC |
| Publication | Applied Physics Letters |
| Article Title | Modified configuration of relativistic magnetron with diffraction output for efficiency improvement |
| Author | M. Daimon,W. Jiang |
| Online Publication Date | Nov 9, 2007 |
| Volume number | 91 |
| Issue number | 19 |
| Type of Use | Thesis/Dissertation |
| Requestor type | Student |
| Format | Print and electronic |
| Portion | Figure/Table |
| Number of figures/tables | 2 |
| Title of your thesis / dissertation | NUMERICAL STUDIES AND OPTIMIZATION OF MAGNETRON WITH DIFFRACTION OUTPUT (MDO) USING PARTICLE-IN-CELL SIMULATIONS |
| Expected completion date | Dec 2015 |
| Estimated size (number of pages) | 100 |
| Total | 0.00 USD |

ORDER MORE... CLOSE WINDOW

Copyright Clearance Center RightsLink®

Home | Account Info | Help | Live Chat

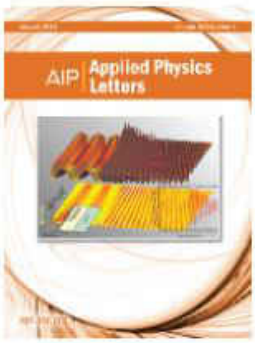


| | |
|---|---|
| **Title:** | Cathode priming of a relativistic magnetron |
| **Author:** | M. C. Jones,V. B. Neculaes,Y. Y. Lau, et al. |
| **Publication:** | Applied Physics Letters |
| **Volume/Issue** | 85/26 |
| **Publisher:** | AIP Publishing LLC |
| **Date:** | Dec 17, 2004 |
| **Page Count:** | 3 |

Rights managed by AIP Publishing LLC.

Logged in as:
Alireza Majzoobi
Account #:
3000979652

LOGOUT

## Order Completed

Thank you very much for your order.

Click here for Payment Terms and Conditions.

Get a printable version for your records.

| | |
|---|---|
| License Number | 3762801376498 |
| Order Date | Dec 05, 2015 |
| Publisher | AIP Publishing LLC |
| Publication | Applied Physics Letters |
| Article Title | Cathode priming of a relativistic magnetron |
| Author | M. C. Jones,V. B. Neculaes,Y. Y. Lau, et al. |
| Online Publication Date | Dec 17, 2004 |
| Volume number | 85 |
| Issue number | 26 |
| Type of Use | Thesis/Dissertation |
| Requestor type | Student |
| Format | Print and electronic |
| Portion | Figure/Table |
| Number of figures/tables | 1 |
| Title of your thesis / dissertation | NUMERICAL STUDIES AND OPTIMIZATION OF MAGNETRON WITH DIFFRACTION OUTPUT (MDO) USING PARTICLE-IN-CELL SIMULATIONS |
| Expected completion date | Dec 2015 |
| Estimated size (number of pages) | 100 |
| Total | 0.00 USD |

ORDER MORE... CLOSE WINDOW

OLD DOMINION UNIVERSITY
IDEA FUSION

Alireza Majzoobi <amajz001@odu.edu>

# Re: Permission for using the figures of paper in Thesis

**Permissions** <permissions@iop.org> Fri, Dec 4, 2015 at 10:48 AM
To: Alireza Majzoobi <amajz001@odu.edu>

Dear Alireza Majzoobi,

Thank you for your request to reproduce IOP Publishing material in your thesis.

Regarding:

Figures 1, 4, 7 and 9 (Plasma Phys. Control. Fusion 47 (2005) A231–A260)

We are happy to grant permission for the use you request on the terms set out below.

**Conditions**

Non-exclusive, non-transferrable, revocable, worldwide, permission to use the material in print and electronic form will be granted **subject to the following conditions:**

- Permission will be cancelled without notice if you fail to fulfil any of the conditions of this letter.
- You will make reasonable efforts to contact the author(s) to seek consent for your intended use. Contacting one author acting expressly as authorised agent for their co-authors is acceptable.
- You will reproduce the following prominently alongside the material:

o the source of the material, including author, article title, title of journal, volume number, issue number (if relevant), page range (or first page if this is the only information available) and date of first publication. This information can be contained in a footnote or reference note; or

o a link back to the article (via DOI); and

o if practical and IN ALL CASES for works published under any of the Creative Commons licences the words "© IOP Publishing. Reproduced with permission. All rights reserved""

- The material will not, without the express permission of the author(s), be used in any way which, in the opinion of IOP Publishing, could distort or alter the author(s)' original intention(s) and meaning, be prejudicial to the honour or reputation of the author(s) and/or imply endorsement by the author(s) and/or IOP Publishing.
- Payment of £0 is received in full by IOP Publishing prior to use.

**Special Conditions – For STM Signatories ONLY (as agreed as part of the STM Guidelines)**

Any permissions granted for a particular edition will apply also to subsequent editions and for editions in other languages, provided such editions are for the work as a whole in situ and does not involve the separate exploitation of the permitted illustrations or excerpts.

If you have any questions, please feel free to contact our Permissions team at permissions@iop.org.

I should be grateful if you would acknowledge receipt of this email.

Kind regards,

Kathryn Shaw

Publishing Assistant
IOP Publishing

**Please note**: We do not usually provide signed permission forms as a separate attachment. Please print this email and provide it to your publisher as proof of permission.

From: Alireza Majzoobi <amajz001@odu.edu>
To: Permissions <permissions@iop.org>.
Date: 04/12/2015 15:27
Subject: Re: Permission for using the figures of paper in Thesis

[Quoted text hidden]

OLD DOMINION UNIVERSITY
IDEA FUSION

Alireza Majzoobi <amajz001@odu.edu>

## Re: Permission for using the figures of paper in Thesis

**John Verboncoeur** <johnv@egr.msu.edu> Mon, Dec 7, 2015 at 2:27 PM
To: Alireza Majzoobi <amajz001@odu.edu>

Alireza,

I would be pleased if the figures would benefit your thesis. As long as they are referenced, then I approve.

Cheers,

John P. Verboncoeur
President, IEEE Nuclear and Plasma Sciences Society
Associate Dean for Research, College of Engineering
Professor, Electrical and Computer Engineering
Professor, Computational Mathematics, Science, and Engineering
Michigan State University
3410 Engineering Bldg
428 S. Shaw Lane
East Lansing, MI 48824-1226
517-355-5133
johnv@egr.msu.edu
[Quoted text hidden]
[Quoted text hidden]

# VITA

## Academic Background

- ✓ M.Sc. in Power Engineering/High Voltage, University of Tehran, Tehran, Iran, Oct. 2011
- ✓ B.Sc. in Electrical Engineering/Power, Sharif University of Technology, Tehran, Iran, Sept. 2007

## Publications

1. A.Majzoobi, R.P. Joshi, A. A. Neuber and J. C. Dickens, "Particle-in-Cell based parameter study of 12-cavity Rising-Sun relativistic magnetron for improved performance", *AIP Advances,* Vol. 5, pp.107102, Oct. 2015.
2. A.Majzoobi, R.P. Joshi, A. Neuber and J. Dickens, "Mechanistic model of explosive emission initiation at metal cathodes", *Journal manuscript submitted.*
3. I.A. Joneidi, A.Majzoobi, A.A.Shayegani, H.Mohseni and Jouya Jadidian, "Aging evaluation of silicone rubber insulators using leakage current and flashover voltage analysis", *IEEE Transactions on Dielectrics and Electrical Insulation*, Vol. 20, Issue 1, pp. 212 – 220, February 2013.

## Conferences (Selected)

1 A. Majzoobi, R.P. Joshi, A. Neuber and J. Dickens, "Analysis of cathode emission phenomena: Effects of barrier thinning, field enhancements and local heating", *IEEE Pulsed Power Conference 2015*, Austin, Texas.

2 A. Majzoobi, I.A. Joneidi, S. Mohajer, H.Mohseni and A.A.Shayegani, "Experimental investigation of effect of UV radiation on flashover voltage of polymeric insulators with and without contamination", *International Symposium on High Voltage* (ISH), Aug2011, Hanover, Germany.

3 A. Majzoobi, I.A. Joneidi, S. Mohajer, H.Mohseni and A.A. Shayegani,"3D modeling of electrical field and electrical potential in different contamination condition in polymeric insulator", *International Symposium on High Voltage*, Aug2011, Hanover, Germany.

4 I.A. Joneidi, A.Ghorbandaeipour, A. Majzoobi, A.A. Shayegani and H.Mohseni "Investigation of ultra violet influence on the surface of silicon rubber insulator", *International Symposium on High Voltage* (ISH), Aug2011, Hanover, Germany.

5 A. Majzoobi, I.A. Joneidi, A.A. Shayegani and H.Mohseni, "Investigation of effect of UV radiation on flashover voltage of polymeric insulators in different conditions", *26th International Power System Conference*, Nov. 2011, Tehran, Iran.

6 H. Abniki, A. Majzoobi, H. Monsef, H. Ahmadi, H. Dashti, "Identifying inrush currents from internal faults using symmetrical components in power transformers,"*IEEE Modern Electric Power Systems Conference (MEPS)*, Wroclaw, Poland, 20-22 Sep. 2010.

7 S. Mohajer, A.A. Shayegani Akmal, A.Mohseni, A. Majzoobi," Probabilistic Approach in Evaluation of Backflashover in Lushan-Deilaman 230KV Double Circuit Transmission Line", *IEEE Conference on Applied Electrical Engineering and Computing Technologies*, 2011, Amman, Jordan.

## Work Experience

- ✓ **Apr. 2008 – July 2013:** ***Electrical Engineer*****;** Energy Industries Engineering & Design Co. (EIED; Subsidiary of OIEC group.); Tehran - Iran.